UNIVERSITY OF CALIFORNIA,

IRVINE

Nanoconfinement Effects and Interfacial Reaction Pathways for Docking CO_2 in Natural and Synthetic Rocks

DISSERTATION

submitted in partial satisfaction of the requirements

for the degree of

DOCTOR OF PHILOSOPHY

in Civil and Environmental Engineering

by

Siavash Zare

Dissertation Committee:
Assistant Professor Mohammad Javad Abdolhosseini Qomi, Chair
Associate Professor Russell Detwiler
Distinguished Professor Douglas Tobias

2022

DEDICATION

To

Humanity

TABLE OF CONTENTS

LIST OF FIGURES

Page

LIST OF TABLES

Page

ACKNOWLEDGMENTS

I would like to thank the following individuals. First, I thank my advisor, Dr. Mohammad Javad Abdolhosseini Qomi, for funding my research and unwavering support throughout my doctoral study. I am grateful for many fruitful discussions with Dr. Andreas Funk and Dr. Quin Miller. I thank my committee members, Professors Douglas Tobias and Russel Detwiler for their time and contributions. Finally, I extend my gratitude to my family and friends for being there for me every step of the way.

VITA

Siavash Zare

EDUCATION

2022	Ph. D. in Civil and Environmental Engineering, University of California, Irvine
2016	M.Sc. in Structural Engineering, Sharif University of Technology, Tehran, Iran
2013	B.Sc. in Civil and Environmental Engineering, Amirkabir University of Technology, Tehran, Iran

RESEARCH EXPERIENCE

2017-22	Graduate Research Assistant, University of California, Irvine, CA
2020-2021	Henri Samueli Fellow, University of California, Irvine, CA
2014-2016	Graduate Research Assistant, Sharif University of Technology, Irvine, CA

PUBLICATIONS

Thrift, W. J., Nguyen, C. Q., Darvishzadeh-Varcheie, M., Zare, S., Sharac, N., Sanderson, R. N., ... & Ragan, R. (2017). Driving chemical reactions in plasmonic nanogaps with electrohydrodynamic flow. *ACS nano*, *11*(11), 11317-11329.

Masoumi, S., Zare, S., Valipour, H., & Abdolhosseini Qomi, M. J. (2019). Effective interactions between calcium-silicate-hydrate nanolayers. *The Journal of Physical Chemistry C*, *123*(8), 4755-4766.

Zare, S., & Qomi, M. J. A. (2021). Reactive force fields for aqueous and interfacial magnesium carbonate formation. *Physical Chemistry Chemical Physics*, *23*(40), 23106-23123.

Zare, S., Uddin, S., Funk, A., Miller, Q. R. S., Abdolhosseini Qomi, M. J. (2022). Nanoconfinement Matters in Humidified CO_2 Interaction with Metal Silicates. Submitted to *Environmental Science: Nano*

Zare, S., Funk, A., Abdolhosseini Qomi, M. J. (2022). Formation and Dissolution of Surface Metal Carbonate Complexes: Implications for Interfacial Carbon Mineralization in Metal Silicates. Submitted to *Environmental Science & Technology*

ABSTRACT OF THE DISSERTATION

Nanoconfinement Effects and Interfacial Reaction Pathways for Docking CO_2 in Natural and Synthetic Rocks

By

Siavash Zare

Doctor of Philosophy in Civil and Environmental Engineering

University of California, Irvine, 2022

Assistant Professor Mohammad Javad Abdolhosseini Qomi, Chair

Carbonation of natural earth-abundant and synthetic metal silicates promises scalable solutions to permanently store CO_2. With enigmatic observations of enhanced reactivity in wet CO_2-rich fluids, understanding the kinetics proves critical in designing secure and economical geological carbon sequestration and concrete technologies. Here, we use atomistic simulations, density functional theory, and free energy calculation techniques to probe the nature of physicochemical processes at the rock-water-CO_2 interface. We choose nanoporous calcium-silicate-hydrate (C-S-H) and forsterite (Mg_2SiO_4) as model metal silicate surfaces that are of significance in the cement chemistry and geochemistry communities, respectively. We show that while a nanometer-thick interfacial water film persists at undersaturated conditions consistent with *in situ* infrared spectroscopy, the phase behavior of water-CO_2 mixture changes from its bulk counterpart

depending on the surface chemistry and nanoconfinement. We also observe enhanced solubility at the interface of water and CO_2 phases, that could amplify CO_2 speciation rate. Through free energy calculations, we show that CO_2 could be found in a metastable state near the C-S-H surface, which can potentially react with surface water and hydroxyl groups to form carbonic acid and bicarbonate. These findings support the explicit consideration of nanoconfinement effects in reactive and non-reactive pore-scale processes. To investigate reactions at the solid-liquid interface, we develop Mg/C/O/H ReaxFF parameter sets for two environments: an aqueous force field for magnesium ions in solution and an interfacial force field for minerals and mineral–water interfaces. Then, we leverage reactive and non-reactive molecular simulations to probe the elementary reaction steps involved in the interaction of bicarbonate with metal silicate surfaces. We observe that a reverse proton transport between the bicarbonate and surface hydroxides drives carbonate production and surface metal carbonate complexation in agreement with *in situ* spectroscopy measurements. The resultant carbonate can also contribute to the ligand-enhanced dissolution that appears to be slightly favorable over carbonate-unassisted dissolution. We also discuss the potential implications of metal carbonate complex formation and dissolution on lowering the growth's configurational entropy penalty and the rise of interfacial carbon mineralization pathways.

Chapter 1

Introduction

1.1 CO_2 storage, a solution for climate change

Due to its calamitous climate change effects, the raise in the anthropogenic greenhouse gas emission in the post-industrial era has prompted international efforts to stabilize its effects. In the Paris Climate Accords, a goal is set to hold the increase in the global average temperature well below 2 °C above pre-industrial levels and to 'persue efforts' to limit it to 1.5 °C. Unfortunately, the continued greenhouse gas emission from existing and prospective fossil-fuel-burning energy infrastructure is expected to surpass the carbon budget needed to keep the mean global temperature well below 1.5 °C by mid-century[1]. Aside from the importance of "revolutionary changes" in mitigation technology, such as terrestrial solar and wind energy, nuclear fusion, biomass, etc.[2], it is possible to scale up currently operating and pilot projects.[3] One option is decarbonization of fuels and electricity that can be achieved through various routes, among them are Carbon Capture and Storage technologies; In these technologies, CO_2 is captured at fossil-fuel power plants or large industrial sources, compressed to supercritical form, and transferred to storage sites. It is then injected into geological formations, where it can be stored for hundreds or thousands of years. We can also store CO_2 in construction and demolition waste[4,5] or through CO_2-cured concrete technologies[6].

Using current technologies and the availability of enormous storage capacity in deep host rocks, the injection and trapping of CO_2 fluids in the subsurface is a viable solution. CO_2 could be stored in geological formations through four trapping mechanisms[3]: stratigraphic trapping (vertical migration of the CO_2 plume blocked by the seals), residual trapping (a portion of the CO_2 trapped as disconnected droplets), solubility trapping (gradual dissolution of the CO_2 in the formation water), and mineral trapping (formation of carbonate minerals). However, there are known risks associated with CO_2 trapping in deep sub surfaces[7] such as the long-term possibility of post-CO_2 trapping leakage from the caprock, opening of pre-existing fractures, fault activation, and earthquake triggering[8]; Because of the relatively high buoyancy of CO_2 with respect to brine, the risk exists for CO_2 removal and leakage from the storage, which is critical to evaluate for bulk CO_2 injection cases.

There have been two major field-scale pilot projects for CO_2 storage in basaltic formations, namely CarbFix in southwest Iceland[9–11] and Wallulah project in the Columbia river basalt group of southeastern Washington state, USA[12–14]. In the first phase of CarbFix project, about 200 tons of CO_2 was injected into basalt formations. CO_2 and water were separately injected underground with a proportion such that CO_2 is fully dissolved in water at the target depth, via a technique known as solution trapping[15]. CO_2 is then minerally trapped when it reacts with the host rocks. Because CO_2 is completely dissolved in water, there is no risk for leakage. In contrast to the CarbFix project, the CO_2 is injected in supercritical form in the Wallulah project, where the storage sites are covered with impermeable caprocks. Hydrologic tests before CO_2 injection and post-CO_2 injection monitoring shows no evidence for CO_2 removal from the storage[16]. Two years after CO_2 injection, 60%[16] and between 72-95%[10,17] of the CO_2 was mineralized in CarbFix and Wallulah projects,

respectively. Overall, both laboratory and field experiments show that storing CO_2 underground through mineral trapping, whether dissolved in water or in bulk CO_2 form, is an effective decarbonatization method.

Understanding the interaction of CO_2 with geological formations is of prime importance, because of the entailed sophisticated coupled processes[18]. When anhydrous $scCO_2$ is injected in geological formations, the formation water in the pore space is partially or completely displaced, and the $scCO_2$ phase adsorbs small amount of water to produce wet $scCO_2$ fluid. The reaction between the host rock and wet $scCO_2$ phase causes dissolution and volume and wettability changes, that overall alters porosity and permeability.[19–22] Therefore, it is critical to understand these reactions from both chemical and mechanical point of view, as new minerals are formed as the products of these reactions while long-term permeability and security of the sub surfaces are affected.

CO_2 is known to react with silicate minerals to form carbonate minerals[23]. In aqueous environment, carbonation of divalent metal-silicate ($M_2^{II}SiO_4$) minerals can be simplified as follows,

$$H_2O + CO_2(aq) \rightarrow H_2CO_3(aq) \rightarrow HCO_3^-(aq) + H^+(aq) \rightarrow CO_3^{2-}(aq) + 2H^+(aq) \quad (1\text{-}1)$$

$$M_2^{II}SiO_4(s) + 2CO_3^{2-}(aq) + 4H^+(aq) \rightarrow 2M^{II}CO_3(s) + H_4SiO_4\ (aq) \quad (1\text{-}2)$$

$$H_4SiO_4\ (aq) \rightarrow a\text{-}SiO_2(s) + 2H_2O \quad (1\text{-}3)$$

Equation (1) represents the formation of carbonic acid when CO_2 dissolves in water[24]. Then, carbonic acid can turn into bicarbonate and carbonate by successively transferring the proton to water. The resulting protons acidify water and causes the metals and silicates in water to dissolve. When the molar concentration of metals and carbonates reach the saturation levels, metal-carbonate $M^{II}CO_3$ precipitates along the formation of silicic acid as the by-product, as shown in

Equation (2). Finally, the silicic acid can polymerize to form a secondary amorphous passivation layer that inhibits reaction kinetics while producing water as shown in **Equation (3)**. As can be seen in these chemical equations, water plays a key role in the carbonation reaction from speciation of CO_2 to the formation of amorphous silica. However, when it comes to the interaction of wet $scCO_2$ and metal silicates in the pore space, some subtleties arise partly due to immiscibility of water and CO_2[25], the effect of confinement on the chemical reactions[26–28], and water properties at the interface[29–31].

Divalent metal silicate minerals (Me_2SiO_4) Carbonation reactions with humidified $scCO_2$ phases are known to occur at the thin water film adsorbed on the surface of the host rock. Although confined in nano-meter scale environment, the adsorbed thin water film is shown to perhaps facilitate carbonation reactions in Ca/Mg silicates in laboratory[32–39] and field experiments.[40] In addition to the different quasi-2D geometry of the adsorbed water film on the surface of metal silicates, its nano-structure is highly structured and it has a lower dielectric constant compared to bulk water. The molecular mechanisms responsible for carbon mineralization in the water film and the properties of the CO_2-water mixture in the confined space are critical elements for understanding carbonation and further accelerating the process. Due to the nano-scale nature of the solid-water-CO_2 interface and fast reactions in the water film, performing experiments is often difficult. However, molecular simulation techniques are able to offer some insight on these nano-scale interactions.

1.2 Research objectives and dissertation outline

In this dissertation, we aim to shed some light on the thermodynamics and early-age molecular interactions that occurs during carbonation at the solid-fluid interface through the means of molecular simulations, density functional theory, and free energy calculation techniques. In **Chapter 2**, we investigate the effects of nanoconfinement on the phase behavior of humidified CO_2-rich mixtures in contact with Calcium-Silicate-Hydrate (C-S-H), the binding phase of cement hydrate, and forsterite (Mg_2SiO_4), the magnesium end-member of olivine minerals. We also look at the adsorption of a CO_2 molecule on the surface of aforementioned minerals, as well as its reaction with surface water and hydroxyl groups. In **Chapter 3**, we develop a reactive forcefield for magnesium-containing systems in aqueous and interfacial environments. This forcefield enables us to investigate the interaction of carbonic acid and bicarbonate with the surface of the minerals at the solid-liquid interface, as discussed in **Chapter 4**. Also in **Chapter 4**, we calculate the free energy landscape for the dissolution of metal cations from the surface of minerals through the assistance of carbonate ions.

Chapter 2

Nanoconfinement Matters in Humidified CO_2 Interaction with Metal Silicates

2.1 Introduction

Carbonation of Mg- and Ca-rich silicates promises scalable solutions to mitigate the calamitous impacts of anthropogenic carbon emissions. These solutions can be realized in geological settings through *in situ* carbonation of mafic and ultramafic lithologies[16,22,41], or above ground through well-controlled *ex situ* carbon mineralization facilities to produce value-added concrete products[6]. The potential *in situ* CO_2 storage capacity of continental flood basalts[42], oceanic igneous plateaus[43,44], and basalt ridges[45,46] is greater by an order of magnitude than the estimated CO_2 emissions from burning all fossil fuel resources on Earth.[41] Ultramafic tailings[47,48], alkaline industrial residues[49], construction and demolition waste[4,50] and naturally occurring minerals such as olivine[51], can also collectively offset up to 30 Gt of emissions a year via *ex situ* proccesses.[52]

Whether realized *in* or *ex situ*, the permanent CO_2 conversion to carbonate minerals is advantageous over storage through residual trapping in nonreactive sedimentary formations.[53,54] However, the carbon mineralization extent and associated costs should be optimized to engender maximal CO_2 uptake through a rapid and close-to-complete carbonation process. Therefore, it is critical to predict the carbonation processes, including rates and mechanisms, as they directly affect storage security, efficiency, and cost. Despite this urgency, our understanding of carbon mineralization kinetics and underlying molecular pathways, especially with humidified CO_2-rich fluids, remain limited.

A major challenge in determining the carbonation rate is the complexity arising from confinement effects on fluid-rock and fluid-fluid interactions in the pore space. Compared to the bulk phase, confined fluids express substantially different physicochemical attributes and reaction rates.[26–28] For instance, recent experiments highlight the distinct thermodynamic properties of fluid in shales[55–57], model nanoporous glasses[58], and mesoporous silicon[59]. When confined in nanoporosity, fluid-solid interaction can also significantly impact the fluid phase behavior, sorption, capillary condensation, and imbibition.[60–62] Based upon experiments performed on mesoporous silicon[59], a follow-up theoretical study[60] showed that imbibition occurs when the relative humidity is above a critical value, well below the vapor saturation pressure. The fluid mixture phase behavior in the porous rock is particularly significant as it remains unclear to what extent the classical bulk aqueous-mediated dissolution-precipitation pathways can be applied to water-poor systems.

In this work, we study nanoconfined water-CO_2 mixtures on two model metal silicates with wide-ranging environmental and technological significance: 1) forsterite (Mg_2SiO_4), the magnesium endmember of olivine, relevant to carbonation studies of mafic (e.g. basalt) and ultramafic (e.g. peridotite) lithologies, and 2) Calcium-Silicate-Hydrate (C-S-H), the binding phase in the cement paste that is responsible for concrete's strength, fracture, and durability properties.[63–65] Carbonation of concrete infrastructure is estimated to be the sink for about 2.5% of the anthropogenic carbon emissions, despite an unsettlingly high carbon footprint linked to cement production.[66–68] Carbonation of C-S-H is also of prime importance for the well-bore integrity[69–71] and valorization of construction and demolition wastes that places tangible pathways for net zero or even negative carbon footprint concrete technologies within reach[72]. The motivation to conduct

a comparative study between C-S-H and forsterite is two-fold and goes far beyond their technological significance. First, while forsterite is a natural mineral dominated by macroscopic fracture networks, C-S-H provides a nanoporous model system[73] that readily lends itself to studies of confined fluids[30]. Second, the residence time of water in the first hydration shell of Mg^{2+} cations is at least three orders of magnitude longer than that around Ca^{2+} ions.[74] Such extended residence time can potentially hinder dehydration processes and regulate interfacial processes in rock-water-CO_2 systems.[23]

Herein, we employ molecular simulations to determine competitive sorption of CO_2 and H_2O in metal silicate nanopores and address two basic questions surrounding the interactions of humidified CO_2 with forsterite and C-S-H within the thermodynamic range of technological interest. First, we seek to quantify the impact of nanoporosity and chemical composition on the thickness of interfacial adsorbed water films. While molecular simulations delineate the structure and energetics of single- and multi-component fluids on metal silicate surfaces[31,75,76], quantitative measurements of the adsorbed water film thickness and its dependence on thermodynamic state variables of CO_2-H_2O mixture (pressure, temperature), surface chemistry and pore size remain to be understood. These gaps are difficult to address experimentally, and are key for parameterizing realistic MD simulations of these interfaces[75,77–79]. Although continual progress is being made at determining water film thicknesses at mineral-H_2O-CO_2 interfaces[32,33,35,36,79–85], including for forsterite surfaces, the initial hydration state of the mineral surface to measurements is often unknown, and the influence of pressure-temperature-composition on water film thicknesses has not been systematically explored. Second, we investigate whether carbonic acid and bicarbonate can potentially form at the water-solid interface. To this end, we determine the energetic penalty

for displacing CO_2 through interfacial water layers toward the surface and model its subsequent reaction with hydroxyl groups and adsorbed water molecules.

2.2 Methods

2.2.1 Grand Canonical Monte Carlo Simulations. Two-phase adsorption simulations in the present study, namely bulk mixture, and slit pore adsorption studies were carried out using the Grand Canonical Monte Carlo (GCMC) simulation approach. Towhee package [86] was utilized to perform all the Monte Carlo simulations in the grand canonical ensemble ($\mu_{H_2O}\mu_{CO_2}VT$) using the Configurational Biased Monte Carlo (CBMC) technique.[87] The configurational-biased insertion or deletion or reinsertion probabilities are 0.25 and 0.125 for water and CO_2 respectively. The biased molecular translation probabilities are 0.75 and 0.375 for water and CO_2 with maximum displacement 0.5Å. The biased molecular rotation probability is 0.5 for all molecules with the maximum rotation of 0.05 rad. The confined CO_2-H_2O adsorption simulations are carried out between two C-S-H and forsterite slabs with dimensions of 26 Å x 23 Å, and 26 Å x 26 Å, respectively. Due to high computational costs, layers are fixed in these simulations. Such an assumption has a negligible effect on the adsorption properties in non-swelling systems such as hardened concrete and igneous rocks. We used the conventional SPC water model[88], EPM2 CO_2 model[89], and Lorentz-Berthelot combination rule to model CO_2-H_2O mixtures. We note that such a combination might slightly underestimate the interfacial tension between water and carbon dioxide[53]. However, this would not significantly alter the thickness of interfacial water films that are governed by the water-mineral interfacial tension. ClayFF[90] and its modified version[75] are used respectively to model C-S-H and forsterite surfaces. We apply Lorentz-Berthelot mixing rules to

describe solid-fluid interactions. While the Lorentz-Berthelot mixing rule overestimates the single water adsorption energy on forsterite by ~10% (ΔE_{cal}=-31 kcal/mol vs. $\Delta E_{LBmixing}$ =-34 kcal/mol), it matches the adsorption energy measured via calorimetry at three mono-layers water coverage.[75] Therefore, the mixing rule satisfactorily predicts adsorption properties at thermodynamic conditions relevant to this work (RH~90%). However, a reparameterization of the modified ClayFF potential would warrant a better match with experiments and DFT calculations at lower relative humidity levels (water coverage below two monolayers). In contrast to ClayFF, variable charges for the C-S-H constituents were employed, similar to the previous simulation work on C-S-H [91], to ensure charge-neutrality. Before GCMC calculations, C-S-H layers are relaxed in the MD simulations with the CSH-FF potential, a version of ClayFF tuned specifically to model C-S-H structures and reproduce its mechanical properties. Similarly, MD relaxation is done for the hydroxylated {010} surface of forsterite using the modified Clay-FF potential. Forsterite surface was terminated at M2 sites recognized as the most stable termination through X-ray reflectivity[92], DFT[77], and molecular simulations[93,94]. MD simulations are done in the NVT ensemble using the Nosé-Hoover thermostat with a relaxation time of 100 steps and the timestep of 1 fs. The adsorption process in the slit pore was performed at four different thermodynamic conditions represented in **Table 2.1**. All confined GCMC simulations are equilibrated at least 25 million Monte Carlo (MC) steps. We continued slow converging simulations up to 60 million steps to ensure proper convergence.

2.2.2 Molecular dynamics simulations. MD simulations are performed in the canonical ensemble (NVT) with Nosé-Hoover thermostat and time step of 1 fs using LAMMPS software.[95] We use the same potentials as in GCMC calculations except for C-S-H, where flexible SPC water model[96] and

flexible EPM2 model for CO_2 molecules[97] were used. Also, SPC/E water model was used for Forsterite consistent with Kerisit et al[75]. We allow the first two layers of the surface to vibrate freely and kept the rest of the atoms in the substrate fixed to reduce the computational cost and for to enable the inner layers as a bulk-like structure. The cell is equilibrated for 100 ps, and the distribution analysis is derived from a production phase of 10 ns.

2.2.3 Potential-of-Mean-Force (PMF) Calculations. The energetics of the physisorption and dissociation of respectively carbon dioxide and metal on the solid surface is determined via the umbrella sampling (US) technique as implemented in the "PLUMED 2.5" add-on package to LAMMPS[98]. Here, we use a biased harmonic spring with a stiffness of 200 kcal/mol$Å^{-2}$ and 120 kcal/mol$Å^{-2}$ between the object (CO_2 molecule for the case of adsorption, Me^{2+} cation for the case of dissociation) and a reference Me^{2+} atom on the surface respectively. The normal distance to the solid surface is taken as the "collective variable" and sampling windows are separated by 0.1 Å. CSH-FF[99] and a modified version of Clay-FF[77] were used as forcefields for the adsorption of CO_2 on the surface of CSH and Forsterite respectively. An additional collective variable namely the surface Mg water coordination number is also considered, as discussed in the main text. The harmonic spring with stiffness of 2000 kcal/mol is chosen for the coordination number. Histograms of the distribution of the collective variables were produced after 500 ps of equilibration phase, and another 1 ns of the production phase of MD runs at 300 K in the NVT ensemble. The substrate (except the first two layers) were fixed. A weak harmonic potential was also considered in the 'xy' plane (parallel to the surface) to keep the CO_2 molecule in the desired adsorption/desorption site, enclosed in a cylinder with the fixed reference atoms on its base. The free energy difference is then obtained via the weighted histogram analysis method (WHAM)[100].

2.2.4 Density Functional Theory Calculations. A double layer of C-S-H with cell lengths a x b x c = 26.54 Å x 24.44 Å x 18.20 Å and cell angle γ = 82.5° and the other angles 90° has been created with Ca/Si ratio of 1.7 as described in ref [91]. For stabilization, two layers of water were added on the lower surface. A single CO_2 molecule was placed 10 Å above the unwetted surface to obtain a reference structure for unreacted CO_2. The entire structure was pre-optimized using ReaxFF[91] as implemented in LAMMPS. First, an MD was run with a 0.25 fs time step and a ramp brought up the temperature from 1 K to 298.15 K within 100 ps. Next, the MD was allowed to run for 500 ps before the ensemble was cooled down to 1 K within 500 ps. This yields a realistic initial guess structure for DFT calculations, with all chemically reasonable re-combinations and dissociations of water molecules completed. To obtain starting structures for adsorption and chemically reacted products, the CO_2 molecule had been shifted 3 Å and 1 Å above each reactive site, respectively. Reactive sites were 1) water on the surface 2) hydroxide on the surface, 3) an unhydrated dangling oxygen in a silicate dimer. This setup had been proven reasonable in a previous investigation[101]. The starting structures were then also pre-optimized as described above.

For all DFT calculations, the program CP2K[102] has been used with a combined Gaussian and plane waves ansatz. A double-ζ polarized basis set optimized for condensed phase[103] was applied together with a cutoff value of 500 Ry for the plane waves basis and GTH pseudopotentials [104–106]. The Kohn-Sham equations were solved to an accuracy of 10^{-8} E_h with the revised PBE[107,108] GGA functional and the D3 set of dispersion corrections[109]. The pre-optimized structures were fully optimized without any constraints and the resulting structures were interpolated for NEB calculations. First, the NEB was optimized within the D-NEB framework until a maximum error of 5 mE_h/a_0 in RMS gradients and 10^{-2} a_0 in RMS displacement had been achieved. Next, the band

optimization continued using IT-NEB[111] for 10 steps before it switched to CI-NEB[112] until the final convergence of 0.5 mE_h/a_0 in RMS gradients and 10^{-3} a_0 in RMS displacements had been achieved, which corresponds to an accuracy of at least 1 kJ/mol. Minima were converged to at least 0.45 mE_h/a_0 maximum gradient and 0.003 a_0 maximum displacements.

2.3 Results and Discussion

2.3.1 Formation of interfacial water films on metal silicate surfaces in contact with wet CO2-rich fluids**:** When the CO_2-H_2O mixture invades the pore structure of the host rock (Me^{2+} silicates), the CO_2-H_2O molar fraction changes according to the surface chemistry and the confinement geometry. Therefore, for water bearing CO_2 sequestration applications where carbonation reactions occur at the confined thin water film on the Me^{2+} silicates, it is critical to understand the molar fractions of water (adsorbed water film thickness) and CO_2 that exist in the pore.

To unravel the CO_2-H_2O mixture composition in the slit-pore, we perform Grand Canonical Monte Carlo (GCMC) simulations of competitive CO_2-H_2O adsorption. Unlike the classical molecular dynamic (MD) that keeps the number of atoms and molecules fixed during the simulation, GCMC allows the exchange of species between a pre-defined reservoir and the simulation box making it the proper computational platform to model adsorption phenomena. We perform GCMC calculations with four types of wet CO_2-rich fluids on the surface of defective Hamid tobermorite[113] ($Ca_{2.25}[Si_3O_{7.5}(OH)_{1.5}]\bullet 1H_2O$)) (001) at 1.7 Ca/Si ratio as an analog of C-S-H[63] and hydroxylated (010) surface of forsterite. In GCMC simulations, one fluid corresponds to the normal carbonation at ambient conditions, two are relevant to water-bearing supercritical CO_2 fluids at geological conditions[41], and one relates to an intermediate gaseous CO_2. For thermodynamic conditions corresponding to the above mentioned four fluid mixtures, see **Table**

Table 2.1: Thermodynamic properties of H_2O-CO_2 bulk mixtures in ambient condition, gaseous (g), and supercritical (sc) conditions.

	T(K)	P(bar)	$\mu_{H_2O}(\frac{kJ}{mol})$	$\mu_{CO_2}(\frac{kJ}{mol})$	ρ^{CO_2-rich} (g/cm^3)	$x_{CO_2}^{CO_2-rich}$ Mole Fraction
Ambient Condition	300	1	-46.00	-40.00	0.0002	0.9756
CO_2(g) at 20 bar	300	20	-46.00	-33.25	0.0409	0.9982
scCO_2 at 100 bar	348.15	100	-47.00	-35.75	0.2125	0.9942
scCO_2 at 200 bar	348.15	200	-47.00	-34.50	0.5965	0.9956

2.1, Appendix A. Note 1 and Appendix Figs. A1-A3. The relative humidity across these conditions is roughly 90%.

The slit pore in C-S-H is varied between 26 Å to 54 Å to explore its nanoporous structure. The forsterite simulations are focused on a 44 Å slit pore, which represents a cleaved surface and proves large enough to prevent imbibition. These olivine nanopores, including grain boundaries and fluid inclusions, are important dynamic environments that host dissolution-precipitation and mass transfer reactions that promote volume changes and reactive cracking.[114–117]More generally, these reactive nanopores are important in mafic rocks, including basalts, as Luhmann et al.[118] (ultra)small-angle neutron scattering measurements showed that CO2-rich brine increases the basalt's porosity, leading to pore sizes in the range of ~1 nm to 1 μm in response to secondary reactions and shrinkage-induced volume changes.

As presented in **Fig. 2.1.a-h**, interfacial water films persist on metal silicate surfaces even at supercritical CO_2 conditions and shield surfaces from direct contact with the segregated CO_2-rich phase. Similar observations are also reported for clays[76] and calcite[119,120], which suggest nanometer-thick water films should prevail on hydrophilic mineral surfaces when put in contact with a humidified CO_2-rich fluids. Interestingly, for the case of $scCO_2$ at 100 bar and 348 K, imbibition occurs in the slit-pore of C-S-H with a size as large as 44 Å, see **Fig. 2.1.b**. However, when we increase the CO_2 pressure to 200 bar, CO_2 manages to enter the same slit-pore size, as shown **Fig. 2.1.a**. On the other hand, water is only present as layers on the C-S-H surfaces at ambient (1 bar) and 20 bar CO_2(g) at 300 K (**Fig. 2.1.c and Fig. 2.1.d**).These two observations show the critical role of pressure and temperature in diffusion-to-imbibition transition at undersaturated water vapor pressure. Also, in contrast to C-S-H, we observe that CO_2 permeates

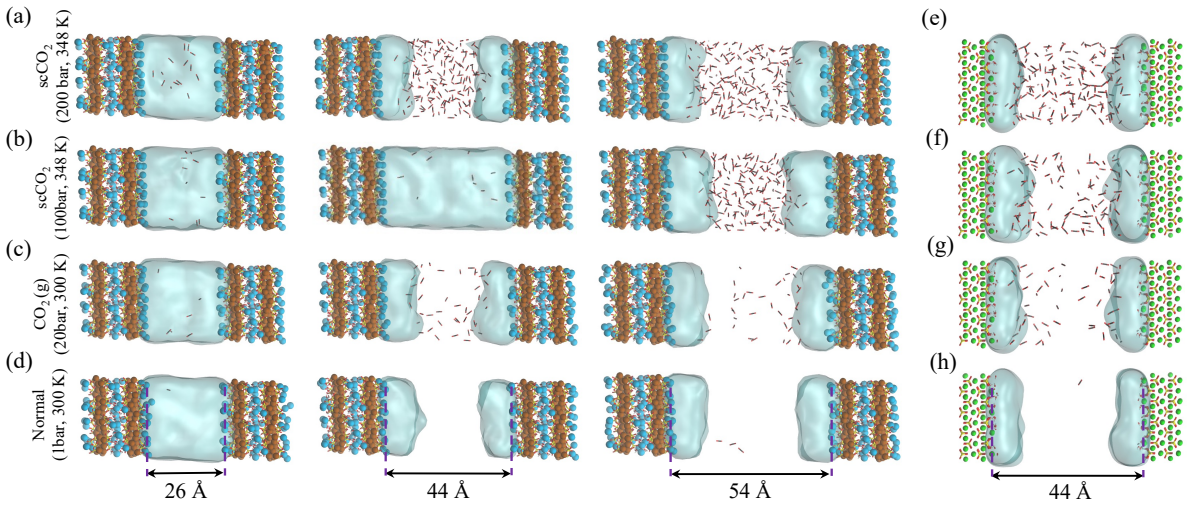

Figure 2.1: Competitive adsorption of H2O-CO2 mixtures in the slit C-S-H and forsterite porosity at normal, gaseous, and supercritical conditions. (a-d) Snapshots from the equilibrated two-phase GCMC adsorption simulations in C-S-H slit pores at different pore sizes and thermodynamic conditions. (e-h) Snapshots from equilibrated two-phase GCMC adsorption simulations in forsterite slit pores at different thermodynamic conditions. Blue and brown spheres represent intralayer and interlayer calcium in C-S-H, respectively. Green sphere represents magnesium. Silicate chains are depicted in yellow-red sticks. The continuous light blue cloud represents water and CO_2 is shown by black and red sticks.

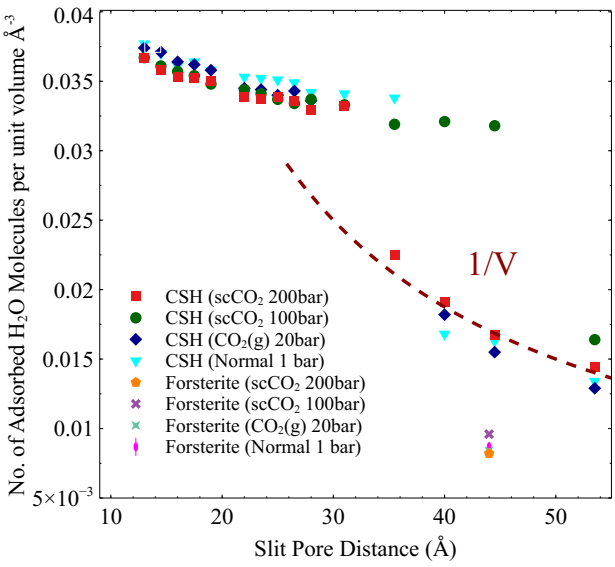

Figure 2.2: Number of adsorbed H2O molecules per unit volume based on the slit-pore distance. 1/V dashed line shows that the number of adsorbed water molecules is constant beyond a certain slit pore.

into the slit-pore of forsterite at the CO_2 pressure of 100 bar and temperature of 348 K, as shown in **Fig. 2.1.f**. This emphasizes the role of surface chemistry in the fluid phase behavior in confined spaces, and it is a signature of the more hydrophilic surface of C-S-H than the {010} surface of forsterite.

In the temperature and pressure ranges considered here, CO_2 could only penetrate the slit pore when the interlayer distance is more than 30 Å, while the interfacial water remains on the surface regardless of the distance, **Fig. 2.2**. Moreover, the total number of adsorbed water molecules converges to an asymptotic value at large pore sizes (> 40 Å), as shown by the dashed line in **Fig. 2.2**. The number of adsorbed water molecules per volume on the surface of forsterite is in general lower than that on the surface of C-S-H, again showing the more hydrophilic nature of C-S-H than forsterite. Regarding the effect of fluid pressure and temperature on the number of adsorbed water molecules, we do not see any significant difference among the thermodynamic conditions

considered in this work. Also, a recent wet $scCO_2$ forsterite carbonation study[83] shows negligible variability in the number of water layers in the temperature ranges between 298 K and 323 K. However, a more comprehensive study with a larger range of pressures and temperatures is required to better understand this issue, something we will discuss in a future work. It is also noteworthy that at interlayer distances of less 20 Å, the density of capillary water is found to be higher than its bulk value (1 g/cm^3) consistent with the simulations on the confined nature of water in CSH[121,122], see **Appendix A. Fig. A.4.**

To gain a more quantitative picture of the phase behavior, the resultant CO_2 mole fractions are overlaid on the experimental and theoretical bulk mixture phase diagram[25,123] in **Fig. 2.3**. Despite CO_2-rich conditions in all GCMC simulations, the equilibrium nanoconfined fluid in pores smaller than 30 Å turns H_2O-rich. This is related to the hydrophilic nature of forsterite[75] and C-S-H[30] surfaces and the effect of surface forces in nanoscale confinements on the fluid phase behavoir[59,60]. Beyond 30 Å, CO_2 permeates within the slit pores, and the mixture composition shifts toward the

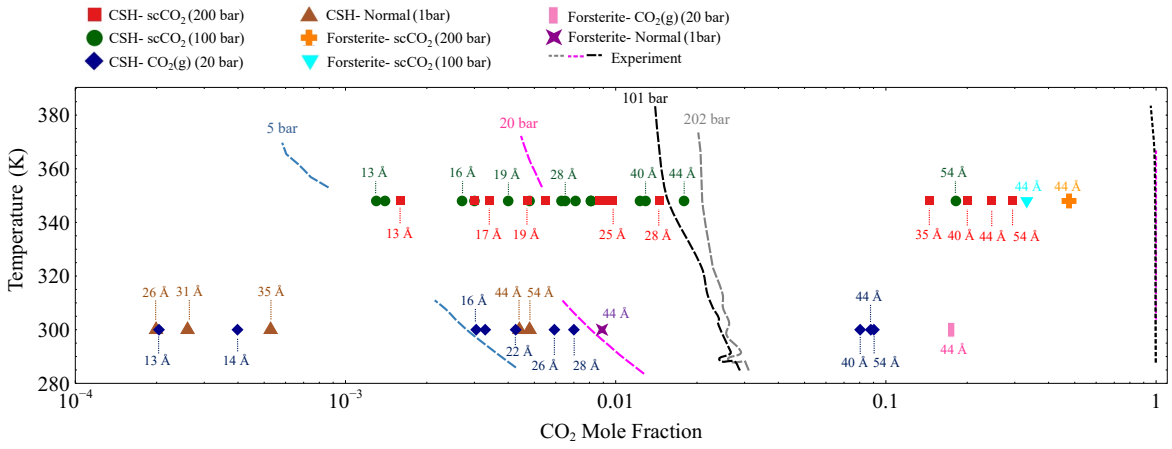

Figure 2.3: The H2O-CO2 phase coexistence diagram overlaid with the adsorbed mixture composition in the slit nano-porosities under various thermodynamic conditions computed via GCMC simulations. Dashed lines represent experimental and theoretical curves for the bulk mixture[70,71].

bulk CO_2-rich mixture (akin to the wet CO_2-rich reservoirs). However, even at pore sizes as large as about ~5 nm, the CO_2 mole fractions deviate from its bulk value counterparts, as shown in **Fig. 2.3**. This strong confinement effect has implications especially for multi-scale porous rocks such as C-S-H, which needs to be taken into account in continuum models or pore-scale models[124–126].

We also find that the average water film thickness on the forsterite surface is roughly 10 Å. The resulted thickness is in line with the recent *in situ* infrared spectroscopy measurements[33] on forsterite surfaces subjected to supercritical CO_2 at 323 K and 180 atm[33] and infrared titration experiments with supercritical CO_2 at 323 K and 90 atm[79], **Fig. 2.4**. Nevertheless, we observe slight variability for the average film thickness on the surface at different carbonation conditions. To address the variability of water film thickness based on CO_2 pressure, a better picture could be achieved by calculating the distribution of species at variable carbonation conditions.

The water film thickness on the surface of C-S-H is shown to be higher than that on the hydroxylated surface of forsterite. To clarify latter point, we calculate the water adsorption energies for different number of water monolayers on both surfaces. The water adsorption energies for 1, 2, 3 and 4 monolayers of water on the {010} hydroxylated surface of forsterite and C-S-H are shown in **Fig. 2.5**. The water adsorption energies on the surface of C-S-H are shown to be consistently lower than that of hydroxylated surface of forsterite. B3LYP calculations on gas phase clusters[127] show that hydration energies of Mg^{2+} cation are in general lower than that of Ca^{2+}. However, AIMD simulations[77] show that calcio-olivine (γ-Ca_2SiO_4), a crystalline calcium silicate structure, are more hydrophilic than forsterite when ½ monolayer to 2 monolayers water are

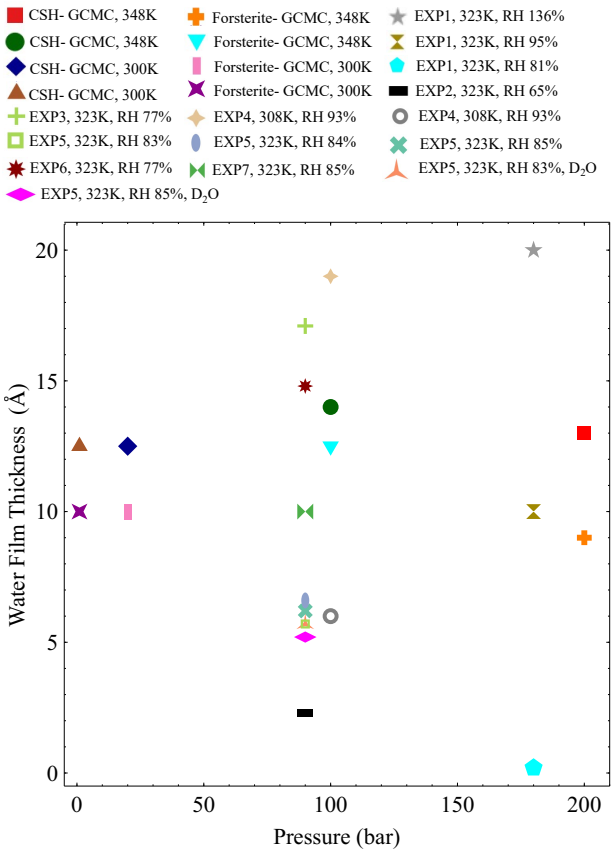

Figure 2.4: The comparison of adsorbed water film thickness on C-S-H and forsterite calculated via GCMC simulations and measured experimentally. EXP1: Molar concentration of water in FTIR setup using Beer's law, Loring et al. (2011)[52]. EXP2: IR titration apparatus, Kerisit et al. (2021)[57]. EXP3: IR titration apparatus, Loring et al. (2018)[54]. EXP4: Molar concentration of water in FTIR setup using Beer's law, Thompson et al. (2014)[50]. EXP5: IR titration apparatus, Miller et al. (2019)[56]. EXP6: IR titration apparatus, Loring et al. (2015)[53]. EXP7: IR titration apparatus, Placencia-Gómez et al. (2020)[49].

adsorbed on the surface. C-S-H is more disordered and has more defects than calcio-olivine, which could entail even higher affinity to water.

For comparison, the adsorption energies derived from calorimetry measurments[128] and previous MD simulations on the non-hydroxylated {010} surface of forsterite[75] are also included in **Fig. 2.5**. Our calculations overestimate the adsorption energies on the hydroxylated surface of forsterite by about 2-3 kcal/mol compared to the upper values of calorimetry experiments. This slight discrepancy could be potentially due to the forcefield artifacts, or an indication that not all silicate groups dissociate water molecules adjacent to the surface. We should also emphasize that, using

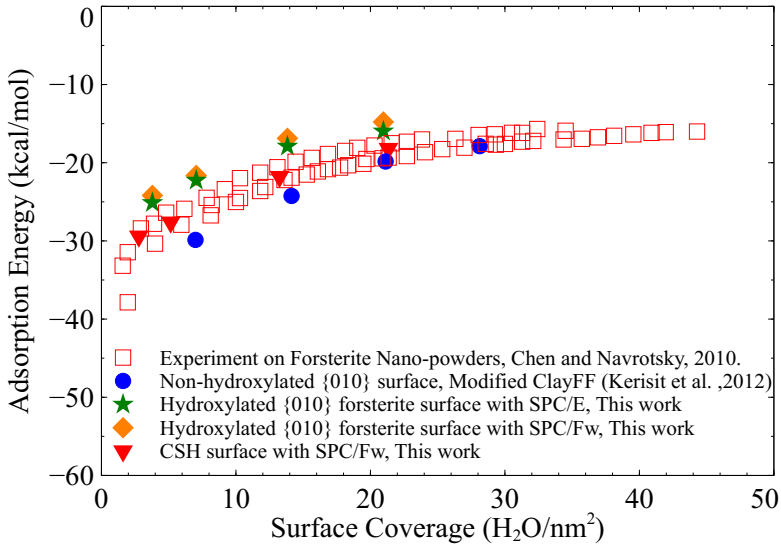

Figure 2.5: The calculated water adsorption energies on C-S-H and forsterite surfaces. Calorimetry measurements[76] and previous classical MD simulation results[44] on non-hydroxylated surface of forsterite are also presented for comparison.

the same forcefield, Kerisit et al.[75] derive a lower adsorption energy for associative adsorption of a single water monolayer on the non-hydroxylated surface of forsterite compared to experiments.

We also note that the water surface coverage for the first monolayer of hydroxylated forsterite and C-S-H are lower than that on the non-hydroxylated forsterite surface, **Fig. 2.5**. We can attribute this to the surface structure of these solids where dissociated water molecules are initially added to the surface resulting in the hydration of silicate groups and the presence of hydroxyl groups adjacent to metal cations. Therefore, the water surface coverage in hydroxylated structures with two monolayers is equivalent to one monolayer on the non-hydroxylated surface.

In addition, we calculate the adsorption energies of forsterite surface with SPC/Fw water model[129], which is a modification of SPC model with flexible bonds and angle, compared to SPC/E water model that was originally incorporated in the modified ClayFF[75] for the surface of forsterite. As pointed out in the methods section, our GCMC calculations are performed with SPC water model which has different oxygen and hydrogen charges than SPC/E, and therefore a different dipole

moment. We use SPC model in our GCMC calculations because it predicts the vapor pressure of water more accurately than SPC/E[130]. Nevertheless, upon our calculation of water adsorption energies on the surface forsterite, SPC/Fw water model only slightly overestimates the adsorption energies compared to SPC/E model, as shown in **Fig. 2.5**.

To resolve the spatial distribution of CO_2 and H_2O molecules as well as surface hydroxyl groups in the slit pore, we perform MD on fully equilibrated confined GCMC simulations. The details of these simulations are presented in the Methods section. The quantitative spatial distribution of water, CO_2, and hydroxyl groups are presented in **Fig. 2.6**. The formation of nanometer-thick interfacial water layers is evident from distributions, acting as a barrier for CO_2 molecules to directly contact the surface. Regardless of thermodynamic conditions, we observe four peaks in the water number density distributions on the surface of forsterite, see **Fig. 2.6. a-d**. However, the furthest peak from the surface does not represent a fully formed water layer. This is consistent with a recent $scCO_2$-forsterite experiments[35], which shows 3.5 water monolayers form on the forsterite surface at 85% relative humidity. On the other hand, we also observe water layers formed on the surface of C-S-H at all pore sizes, see **Fig. 2.6. e-h**. However, due to the appearance of multiple peaks close to each other, it is hard to distinguish water monolayers, although the overall water film thickness on C-S-H is higher than that on forsterites. This irregularities of the water density peaks on the surface of C-S-H could partly result from the observation that surface calcium atoms are more labile and less attached to the surface compared to surface magnesium on forsterite. This enables the water molecules to penetrate inside the C-S-H gel and attach to the second calcium layer and silicate groups, as shown in **Fig. 2.6. e-h**. Another reason for this irregularity on the C-S-H surface is a more disordered layering of calcium ions that attract water molecules, and the

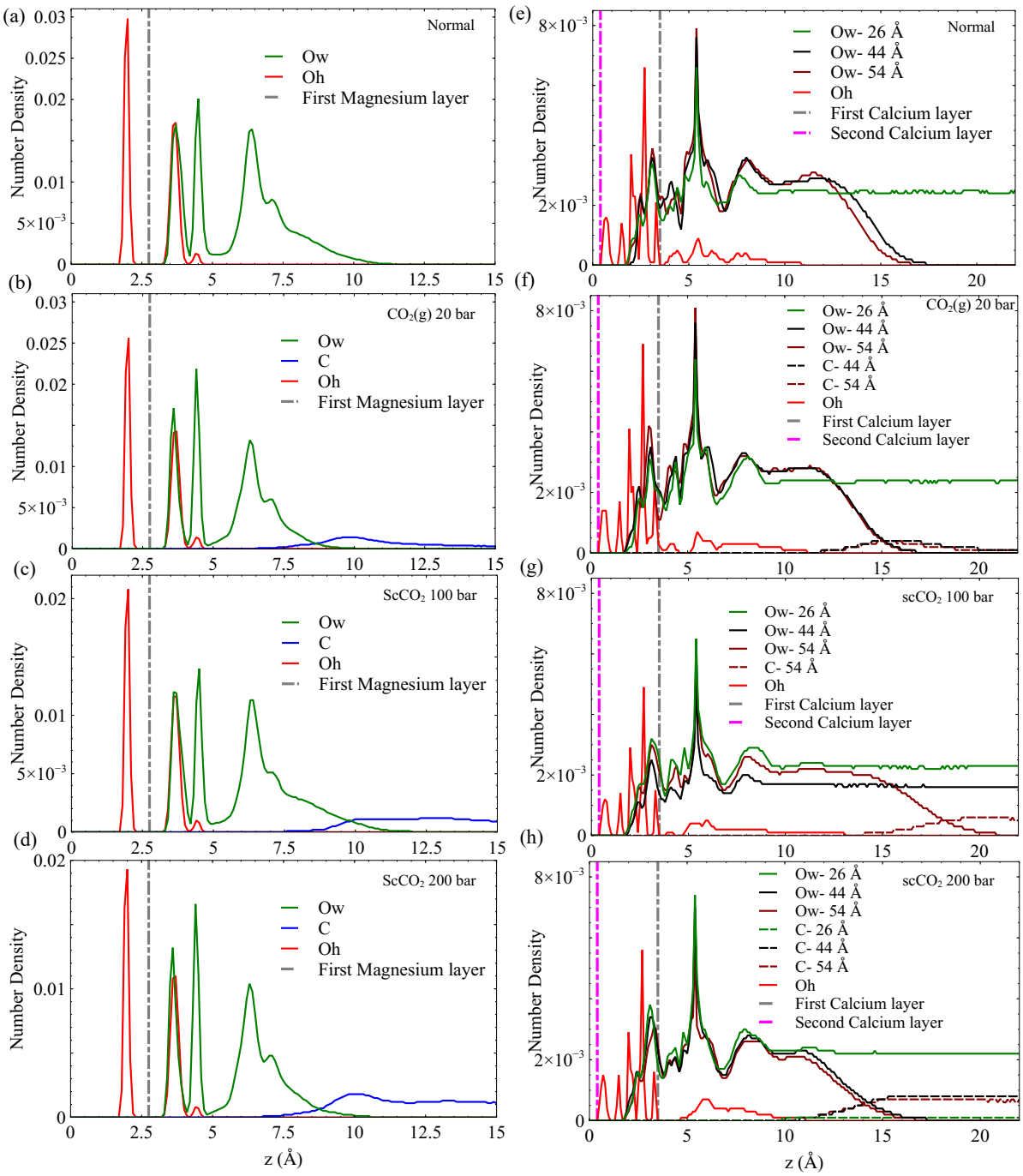

Figure 2.6 The average distribution of H2O, CO2, and OH- species in the slit-pore of forsterite and C-S-H. (a-d) Distribution of species in the slit-pore of forsterite at normal, CO_2 (g), $scCO_2$ (100 bar), $scCO_2$ (200 bar), respectively. (e-h) Distribution of species in the slit-pore of C-S-H at normal, $sbCO_2$, $scCO_2$ (100 bar), $scCO_2$ (200 bar), respectively. The average location of the first magnesium layer on the surface of forsterite, as well as the location of the first and second calcium layers on C-S-H surface are shown by vertical dashed lines. Ow, C, and Oh represent water oxygen, carbon in carbon dioxide, and surface hydroxide oxygen, respectively.

defects and nanoscale cavities resulted from defective silicate chains. Therefore, hydrogen bonds

form between water molecules, hydroxides, and hydrated silicates that are scattered at different elevations from the surface.

The formation of hydration layers has been previously reported for both forsterite[75] and C-S-H[31] in unsaturated and saturated conditions, respectively. Additionally, recent Fast Force Mapping (FFM) experiments on the surface of bohemite[131] illustrates the formation of first water layer on the surface cavities (here, the silicate groups), and the second layer forming on top of hydroxide groups. This is consistent with our results on the surface of forsterite as shown in **Fig. 2.6. a-d**. For the surface of C-S-H, which is much more disordered, the appearance of multiple water density peaks around the surface demonstrates the same phenomena, as shown in **Fig. 2.6. e-h.**

Another significant aspect of the distribution diagrams is that upon the entrance of the dense CO_2 inside the pore, the last water layer contracts and CO_2 distribution peaks at the interface, as could be seen by comparing the distribution at ambient (1 bar) gaseous to supercritical CO_2 (100, 200 bar) in **Fig. 2.6**. Although, the number of water layers do not change, this could be a sign that CO_2 pressure, if above a certain threshold, might alter the number of water layers. The appearance of interfacial peaks in CO_2 distribution at all four conditions is a characteristic of immiscible mixtures verified through both experiments and simulations.[132–135] However, after juxtaposing water distributions with those of carbon dioxide, we confirm that although CO_2 is not a good solvent for dipolar water, the appearance of overlapping shoulders between two species is indicative of enhanced mutual solubility at the interface. This is attributed to the interfacial capillary wave phenomenon and the Coulombic attraction between H_2O and CO_2 molecules.[20] This could potentially amplify the rate of CO_2 speciation at the interface. Another important feature of the resulted distributions is that the proximity of CO_2 and hydroxides within the nanolayered hydration

films, especially on the surface of C-S-H, may increase the rate of bicarbonate and carbonate production. Although it is well established from previous simulations that the thin water film on hydrophilic material displaces CO_2 away from the surface, this proximity of CO_2 molecules and surface hydroxides motivates us to next explore the energetics of CO_2 physisorption on the surface.

2.3.2 Energetics of CO2 speciation on metal silicate surfaces**:** Our adsorption simulations are non-reactive in essence. Thus, it is critical to resolve the mechanistic picture of CO_2 speciation in adsorbed water nanofilms. It is possible that CO_2 speciates to carbonic acid and bicarbonate within the nanofilm in the presence of dissolved cations.[35] Moreover, it is probable that CO_2 reacts with surface hydroxyl groups and surface cations. However, since CO_2 molecules are displaced from the surface due to the presence of the adsorbed water film, it is necessary to quantify the free energy required to bring CO_2 close to the surface. Since the residence time of water molecules around solvated Mg^{2+} ion is in the order of microseconds[74], the water coordination number around surface Mg^{2+} cations is important. Therefore, to sample the full phase space in our free energy calculation for the adsorption of CO_2 on forsterite surface, we consider the surface Mg water coordination number in addition to the perpendicular distance of CO_2 from the surface. The coordination number is defined as:

$$CN = \sum_{i \in \{Ow\}} \frac{1-\left(\frac{r_i - d_0}{r_0}\right)^n}{1-\left(\frac{r_i - d_0}{r_0}\right)^m} \tag{2.1}$$

where r_{ij} is the distance of water molecule *i* with the surface Mg, r_0 is set to 1 Å, d_0 is set to 2.2 Å, *n* is equal to 4, and *m* is equal to 8. The value of d_0 is taken from the peak distance of the surface Mg-water pair distribution function.

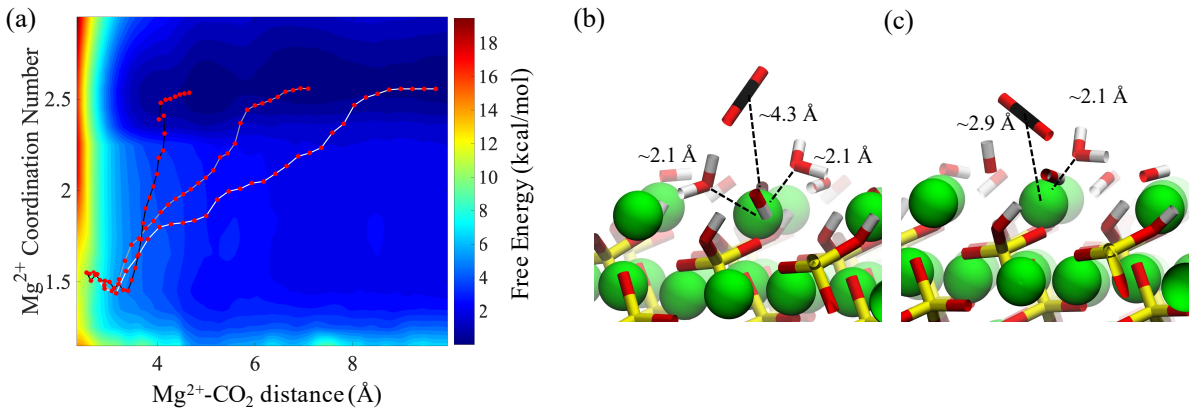

Figure 2.7: Potential-of-Mean-Force (PMF) for the adsorption of CO2 from the solution on the surface of Forsterite. (a) 2D PMF for the adsorption CO_2 on the surface. The three red-dotted paths represent minimum free energy paths corresponding to CO_2 adsorption from the edge of the 2nd, 3rd and 4th adsorbed water layer. While these three paths are distinct, they show that Mg^{2+} dehydration is necessary for the adsorption of CO_2 on the forsterite surfaces. Surface magnesium and the adsorbed CO_2 molecule with (b) two and (c) one neighboring water molecule. Free energy calculations show the departure of one water molecule is thermodynamically necessary for CO_2 adsorption.

The resulting two-dimensional free energy landscape is shown in **Fig. 2.7.a.** The minimum energy path (MEP) of the CO_2 molecule as it goes from the solution to the vicinity of the surface is calculated via the Nudged Elastic Band technique (NEB) method[136]. As shown in the figure, the coordination number of surface Mg changes from two to one as CO_2 is approaching the surface. Also, depending on the initial location of the CO_2 molecule, three distinct MEPs are derived for the cases where CO_2 is initially located at the 2nd, 3rd, and 4th layers of the adsorbed water, as shown in **Fig. 2.7.a.** However, the energy that is required for the CO_2 molecule to pass through the layers and reach the surface is not affected by the initial position of the CO_2. This perhaps shows that regardless of the number of adsorbed water layers, which depends on the relative humidity and CO_2 pressure, the energy of CO_2 physisorption on the forsterite surface is unique. Also, the calculated free energy of CO_2 adsorption is 2.5 kcal/mol higher than the adsorption free energy previously calculated by Kerisit et al.[75] for the non-hydroxylated {010} surface of forsterite. However, the magnesium coordination number was not considered in the PMF calculation in that

work. Therefore, this energy discrepancy could either be the consequence of incorporating magnesium coordination number or the existence of stronger hydrogen bond structure due to surface hydroxides.

It is noteworthy that although we calculate the free energy of CO_2 adsorption on the surface in contact with bulk water, it was previously shown that the structure of the water layers is not drastically different when the forsterite surface is in contact with various number of water monolayers and supercritical CO_2.[75] These findings are consistent with *in situ* XRD measurements of H_2O-CO_2 sorption in hydrophilic montmorillonite[137,138], where CO_2 intercalation was found limited when the hydration level goes beyond one water layer, regardless of isomorphous Me^{2+} exchange.

We also calculate the associative adsorption of CO_2 at random surface sites of C-S-H, as shown in **Fig. 2.8**. We find that, like the forsterite case, CO_2 is more stable in the solution than adsorbed in

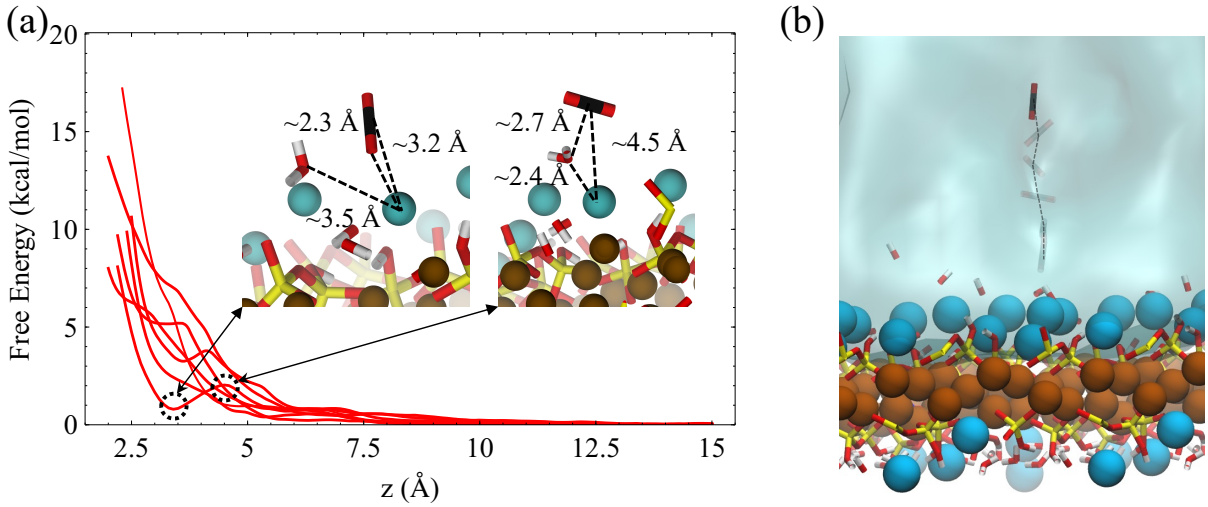

Figure 2.8: Non-reactive interaction of CO2 molecule with wet C-S-H. (a) Physisorption of a CO2 molecule on the surface of C-S-H. Multiple free energy curves are derived for random surface calcium atoms. The insets demonstrate a CO_2 molecule on the surface at the metastable state and the transition state. (b) The umbrella sampling stages for the adsorption of CO_2 on the surface.

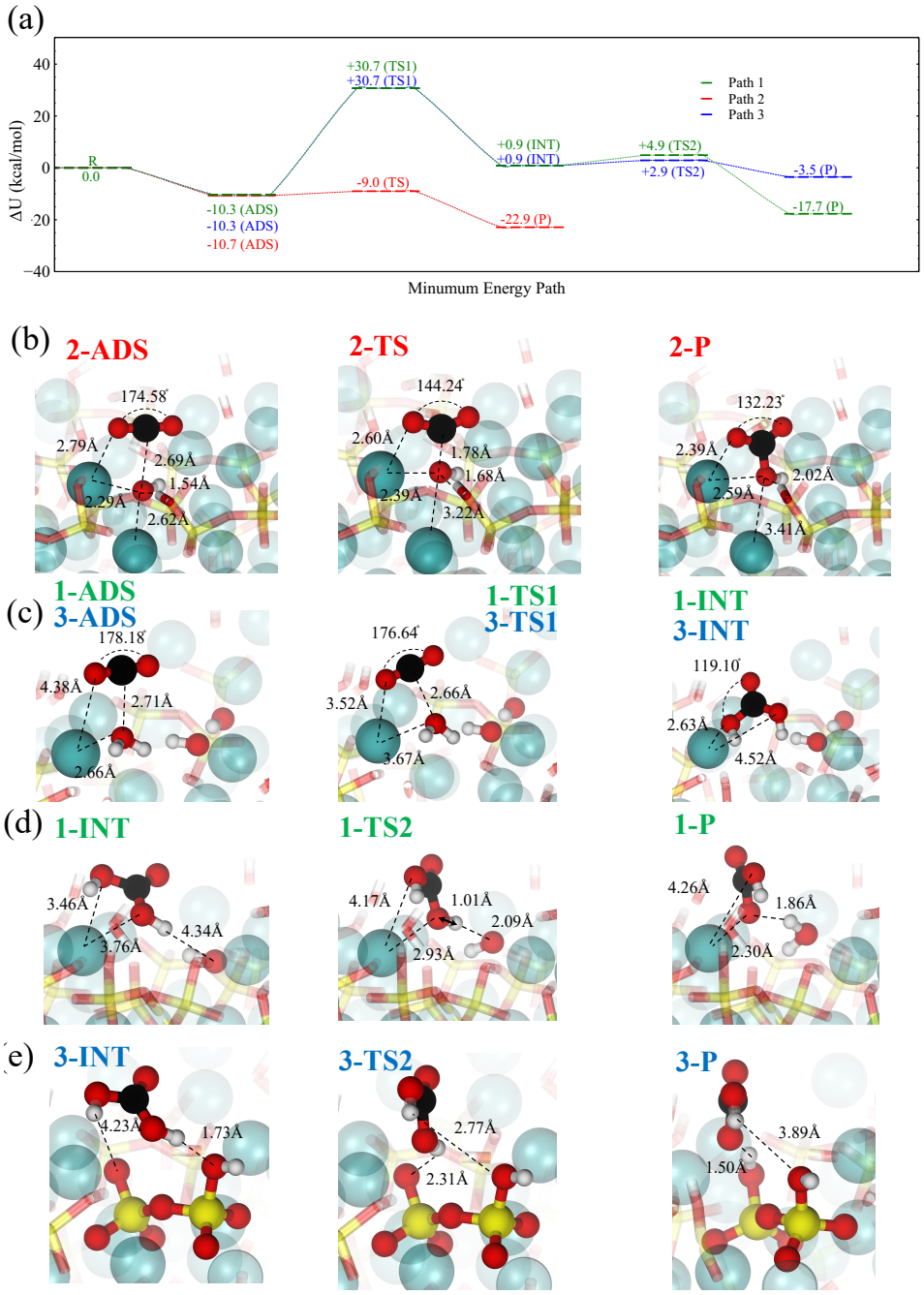

Figure 2.9: Reactive interaction of CO2 molecule with wet C-S-H. (a) DFT calculation of the reaction pathways between CO2 and C-S-H. (Path 1) The reaction between CO_2 and bound water at the hydroxide site. (Path 2) The reaction between CO_2 and surface-bound hydroxide. Strong physisorption is followed by a chemical reaction with a low barrier leading to the formation of bicarbonate. (Path 3) The reaction between CO_2 and bound water at the dangling oxygen site. (b) Snapshots of the adsorbed state (ADS), transition state (TS) and product (P) for reaction paths 2. (c) Snapshots of the ADS, TS and intermediate (INT) state for the reaction of surface water and CO_2 in path 1 and 3. d) Snapshots of the dissociation of carbonic acid to bicarbonate through reaction with surface hydroxide. e) Snapshots of the dissociation of carbonic acid to bicarbonate through reaction with dangling oxygen in silicates.

the on the surface. However, a metastable state is observed when the CO_2 molecule and surface

Ca^{2+} ions are separated by about 3.2 Å on the C-S-H surface. As shown in the inset, the oxygen of the CO_2 molecule in the metastable state is oriented toward the surface calcium cation, reminiscent of a weakly chemisorbed state[139]. Unlike the forsterite case where no minimum is observed, this unique characteristic of the C-S-H surface urges us to consider interfacial CO_2 reactions.

For the carbonation progression, the physisorbed CO_2 must speciate to carbonic acid and bicarbonate by reacting with interfacial water molecules or surface-bound hydroxide. Here, we use Density Functional Theory (DFT) along with the Nudged Elastic Band (NEB) method to calculate the corresponding reaction paths, see the Methods section. **Fig. 2.9.a** summarizes the three reaction paths. The adsorbed, transition, intermediate, and product states are schematically shown for each reaction path in **Fig. 2.9.b-e**.

The most significant reaction occurs at the hydroxide site (path 2), where strong physisorption is connected to a chemical reaction by a low barrier, leading to the formation of bicarbonate, see **Fig. 2.9.b**. In a fully hydrated environment, it takes about 3-10 kcal/mol to bring CO_2 to the hydroxide site on the surface of C-S-H, see **Fig. 2.9.a**. The overall energy barrier associated with this path is lower than or in the same range of the free energy barrier for bicarbonate formation in solutions as calculated via *ab initio* MD[140]. However, the abundance of hydroxide sites on the surface of C-S-H considerably impacts the overall rate of bicarbonate formation when compared to solution reactions. On the other hand, the reaction barrier of CO_2 with water, according to path 2 and 3, if seen from the adsorbate, is approximately 10 kcal/mol lower than the corresponding gas-phase reaction[141]. The snapshots of this reaction are shown in **Fig. 2.9.c**. This clearly indicates the catalytic role of C-S-H surface. Furthermore, it should be noted that the addition of liquid water would further lower the barrier down to 18.6 kcal/mol[142], without any catalytic effects of the

surface taken into account. Once carbonic acid forms, it can dissociate, either transferring a proton to a neighboring unhydrated dangling silicate dimer oxygen on the C-S-H surface (path 3), or a neighboring hydroxide (path 1), see **Fig. 2.9.d** and **Fig. 2.9.e**. With a wetted surface, the first option for proton transfer is unlikely, and the proton transfer to hydroxide is by far more exothermic. In both paths 1 and 3, the adsorbed CO_2 reacts with surface water and forms carbonic acid in a concerted reaction.

It is noteworthy that *ab initio* molecular dynamics (AIMD) simulations in the bulk aqueous water show that CO_2 could react with water to form bicarbonate and a hydronium ion, followed by the formation of carbonic acid in a stepwise reaction.[143] Similar route for this reaction could be imagined to happen in the adsorbed water nanofilm on C-S-H and forsterite leading to the formation of bicarbonate followed by the structural migration of excess proton to the surface hydroxide. Whether through reaction path 2 or in the adsorbed water nanofilm, the formation of bicarbonate is confirmed experimentally through *in situ* $^{1}H-^{13}C$ Cross-Polarized NMR spectroscopy on forsterite nanoparticles[35]. However, bicarbonates were not found on fused silica surfaces. As we demonstrated earlier in this work, it is energetically unlikely to bring CO_2 to the surface of forsterite in the presence surface water layers. Therefore, by ruling out the formation of carbonic acid through direct reaction of CO_2 with the surface hydroxide or surface water, there remains two possible reaction pathways: The reaction of CO_2 with water 1) in the solvation shell of dissolved magnesium in the thin water film[35], or 2) at the interface of dense CO_2 and water nanofilm. However, for the further progression of carbonation reaction to carbonate nucleation whether on the C-S-H or forsterite, the carbonic acid needs to turn into bicarbonate and carbonate.

The specific mechanisms for these deprotonation reactions are still not clear. We delve into the mechanistic picture of these reactions in the next chapters.

Chapter 3

Reactive Force Fields for Aqueous and Interfacial Magnesium Carbonate Formation

3.1 Introduction

Magnesium is an abundant alkaline-earth metal that plays a pivotal role in biological processes[144], automotive industry[145], battery technology[146], and mineral carbonation[147]. In particular, mineral carbonation in geological systems has gained considerable attention during the past two decades amid the record-high CO_2 concentration in the atmosphere. Carbonation is the reaction between CO_2 and Me^{2+}-containing minerals through natural weathering or geological sequestration that produces stable carbonate minerals. When dissolved in water, divalent metal cations like Mg^{2+} and Ca^{2+} bind to water molecules or negatively charged anions like carbonate anions. The pairing between magnesium/calcium and carbonate is a precursor for the precipitation of calcite ($CaCO_3$), dolomite ($CaMg(CO_3)_2$), and magnesite ($MgCO_3$), among other phases. However, the homogeneous nucleation and magnesite growth are slow at low temperatures (< 80 °C) relevant to geological conditions. The sluggish magnesite precipitation could be in part the consequence of the higher water-binding energies of magnesium[127,148] or the lattice limitation of carbonate on the geometrical configuration of CO_3 groups in magnesite[149].

Recently, magnesite precipitation was observed as the product of the reaction between synthetic and natural forsterite (Mg_2SiO_4), magnesium-rich end-member of olivine, and brucite ($Mg(OH)_2$) with water-saturated supercritical CO_2 and at low temperatures[37,150,151]. A common feature of all

Me^{2+}-bearing minerals is that once they contact wet supercritical CO_2, a sub-nanometer water film forms on their surface that facilitate the formation of carbonic acid[29] and surface-metal complexes[35,36], and if the thickness of water film is above a threshold magnesite precipitation occurs[78,79,152]. Time-resolved quantitative X-ray diffraction (XRD) experiments coupled with molecular dynamics simulations show that four water layers are required to allow Mg ion diffusivity across the water layers, enabling magnesite precipitation[78]. Also, *In operando* XRD experiments on the surface of forsterite in contact with wet supercritical CO_2 at various temperatures revealed an anomalously low activation energy barrier for the formation magnesite[153]. However, the underlying molecular mechanism of the carbonation reaction at the sub-nanometer olivine-water-CO_2 interface is puzzling due to experimental spatiotemporal limitations[35,154,155].

Indirect observations suggest that the lower dehydration energy of magnesium in the adsorbed water film is due to the presence of organic ligands[156,157] dissolved in CO_2 or the calcium-like water coordination shell of Mg^{2+} in the adsorbed water nanofilm[153]. However, the exact mechanism remains unknown. Molecular simulations promise to address this knowledge gap by providing an atomic-level insight into the physicochemical nature of the carbonation reaction at the olivine-water-CO_2 interface. First principle calculations offer promising avenues to explore chemical reactions at the nanoscale. For instance, quantum mechanical calculations indicate the H_2O exchange promotes the dissolution of Mg-/Ca-silicate clusters[158]. A*b initio* thermodynamics simulations also show the partial hydroxylation of the most active forsterite surface cleavages when in contact with two monolayers of water at geologically relevant temperatures[159].

However, such quantum mechanical calculations become exorbitantly expensive when the number of atoms exceeds a few hundred. Furthermore, the dynamics of interfacial and bulk water are still not captured without uncertainty in these calculations due to complications in capturing dispersion effects. Force field (FF) methods can potentially address these issues and delve into the atomistic-level details reaching microseconds. Classical molecular dynamics (MD) simulations show that water adsorption on the forsterite surface is exothermic even at undersaturated high CO_2 pressures. They also confirm that CO_2 is displaced from the (010) forsterite surface by the adsorbed water molecules except at low water coverages[75]. Raiteri et al.[160] have successfully developed a thermodynamically stable FF to model magnesium-(bi)carbonate ion pairing in the solution. Nevertheless, the current FFs for interfacial and bulk magnesium carbonate formation are nonreactive, i.e., they cannot simulate proton transfer processes and interfacial chemical reactions. Here, we attempt to develop a reactive FF to model carbonation reactions in bulk water and at the interface of magnesium-containing silicates and hydroxides.

This paper extends the current ReaxFF potential library to include magnesium interactions with oxygen, hydrogen, and carbon in an aqueous, bulk, and interfacial environment. The charge of magnesium is kept fixed, although the charge equilibration scheme in ReaxFF operates as usual for the rest of the elements. The geometrical and mechanical properties of a wide range of magnesium-containing crystals and magnesium-water binding energies are taken as observables in the fitting process. After completing the parameterization stage, we test the resulting parameters for reproducing a group of magnesium-containing solids, water adsorption on crystal surfaces, and Mg-(H)CO_3 ion pairing in the solution. Then, we explore our FF for some reactive environments, including the proton transfer between bicarbonate and brucite surface, the free energy calculation

of the adsorption of carbonate on the forsterite surface, and carbonic acid dissociation in water in the presence of magnesium ion.

3.2 Methods

To describe molecular interactions in magnesium carbonate systems, we derive and validate a set of potential parameters and merge the results with a previously-fitted ReaxFF forcefield[161] that was applicable to aqueous and interfacial calcium carbonate systems. ReaxFF is a bond-order-based FF that can simulate covalent bond formation and breakage. It also implements a charge equilibration scheme that calculates atomic charges based on geometry and electronegativity.[162] The total potential energy, E_{tot}, in ReaxFF is written as:

$$E_{tot} = E_{bond} + E_{vdW} + E_{qeq} + E_{pen} + E_{over} + E_{under} + E_{val} + E_{tors} + E_{conj} \quad (1)$$

where E_{bond}, E_{vdW}, E_{qeq}, E_{pen}, E_{over}, E_{under}, E_{val}, E_{tors}, and E_{conj} are respectively bonded, van der Waals, coulombic, penalty, over-coordination, under-coordination, valence angle, torsion, and conjugation energies. Like calcium, magnesium is present primarily as di-cation due to its ionic nature, except for the case of shortly-lived univalent Mg^{+} observed in the corrosion of magnesium alloys[163]. This allows us to incorporate a fixed magnesium charge and follow the recipe for the fitting of ReaxFF for calcium carbonate systems that treat calcium charge fixed without any bond-order consideration. To model electrostatics, we use the screened Coulomb potential between atom i and j, as implemented in REAXFF[7]:

$$E_{coulomb} = Tap.C.\frac{q_i q_j}{\left[r_{ij}^3 + \left(1/\gamma_{ij}\right)^3\right]^{1/3}} \quad (2)$$

where q_i and q_j are the charges of atoms i and j respectively, Tap is a 7th order polynomial taper function that depends on the distance between the two atoms. This taper function ensures that coulombic energy does not have discontinuity when charges enter or leave the cutoff radius of 10 Å. γ_{ij} is the pairwise screening parameter derived from the geometric mean of single atom screening parameters $\gamma_i \; and \; \gamma_j$.

For the short-range repulsive Mg-C and Mg-H interactions , we choose the repulsive portion of the Buckingham potential as follows:

$$E_{ij} = A_{ij} e^{-r_{ij}/\rho_{ij}} \tag{3}$$

where A_{ij} and ρ_{ij} are characteristic energy and length, respectively. We also choose 12-6 Lennard-Jones (LJ) potential for Mg-O interaction:

$$E_{ij} = \frac{A_{ij}}{r^{12}} - \frac{B_{ij}}{r^6} \tag{4}$$

Where A_{ij} and B_{ij} are LJ fitting parameters. We note that in the reactive FF developed for the calcium carbonate systems[161], only the repulsive part of the Lennard-Jones (12-6) potential was chosen to describe the short-range interaction for Ca-O pairs based on the realistic assumption that Ca^{2+} have negligibly small electronic polarizability. However, in our fitting process, the attractive part of the Lennard-Jones potential for Mg-O interactions helps achieve accurate magnesium hydration energies and magnesium-water distance.

Atomic point charges are usually fixed in most classical MD frameworks, and therefore the effect of the environment on the distribution of charges is neglected. However, in ReaxFF, a similar approach to electronegativity equalization method (EEM) is used to update atomic charges at every

step based on the geometry and fitted atomic properties[164–167]. In this method, total electrostatic energy comprised of intra-atomic and interatomic potentials is defined as:

$$E_{es}(q_1 \dots q_N, x_1 \dots x_N) = \sum_i (E_{i0} + \chi_i q_i + \frac{1}{2} J_i q_i^2) + \sum_i \sum_{j<i} q_i q_j J_{ij} \quad (5)$$

where x_i is the location of atom i, q_i is its charge, E_{i0} is a zeroth-order constant, χ_i is the electronegativity, J_i is the self-coulomb repulsion in atom i, and J_{ij} is the Coloumb potential between two unit charges located at x_i and x_j. The self-coulomb potential could be understood as the electrostatic repulsion between two electrons in a doubly-occupied orbital. The first sum represents the Taylor series expansion of the energy of an isolated atom up to the second order. The second sum represents the conventional inter-atomic Coulomb potential between atoms i and j that is inversely proportional to their distance, $\left|x_i - x_j\right|^{-1}$.

The equilibrium charge distribution is achieved when the first derivatives of the total potential with respect to each charge, $\frac{\partial E_{es}}{\partial q_i}$ or chemical potentials, are all equal. Applying the constraint that the total charge of the system is constant and using the Lagrange multiplier method leads to the following linear equation:

$$\sum_j M_{ij} q_j = \mu - \chi_i \quad (6)$$

where M_{ij} and μ are respectively the coulomb-interaction matrix and the Lagrange's multiplier. If some charges are fixed in the system, it is only required to construct the above matrix equation for variable charges q_i while subtracting the inter-atomic Coulomb potential between the fixed charges and unit charges at location x_i on the right-hand side.

To fit the FF parameters, namely Mg-C, Mg-H, Mg-O and γ_{Mg} potential parameters, we employ the iterative fitting scheme that was previously used to fit the parameters of fixed-charge-calcium REAXFF[161]. To this end, we minimize the error function defined as the sum of squares of the difference between experimental/DFT observable value and ReaxFF-calculated value:

$$F = \sum_{i=1}^{N} w_i (f_i^{obs} - f_i^{calc})^2 \quad (7)$$

where f_i^{obs} is the experminetal/DFT-derived quantity, f_i^{calc} is the ReaxFF-calculated quantity, w_i is the weighting factor for the given quantity, and N is the number of observables. The selected observables are the solid lattice constants, atomic configurations, bond/angle values, and bulk modulus for some of the crystals selected for fitting, as shown in **Table 3.1**.

In each iteration, first the Mg-H and Mg-C parameters are fitted to the lattice structure of αMgH_2[168], and MgC_2 [169] and the bulk modulus of αMgH_2. Then, the derived Mg-H and Mg-C parameters are used to fit Mg-O and γ_{Mg} using the lattice structure and the bulk modulus of $Mg(OH)_2$[170,171], MgO[172], and $MgCO_3$[173,174] crystals along with the total hydration energies (E_{hyd}) of water molecules on the first and second shell[175] of Mg^{2+}, namely $[Mg(H_2O)_6]^{2+}$ and $[Mg(H_2O)_6](H_2O)^{2+}$. Note that the Mg-H and Mg-C parameters are kept fixed at this step. Also, the Mg-Ow bond length of the first shell of water molecules and some of the Mg-Ow-Ow angles were taken as fitting observables, in which Ow being the oxygen in the water in the first and second shell. We repeat these two steps iteratively until we obtain a satisfactory parameter set.

Based on water adsorption calculation on crystal surfaces described later, assigning a formal charge of +2 to magnesium atoms causes an overestimation of water adsorption energies compared to density functional theory (DFT) calculations. Since electrostatics contributions play a

Table 3.1: The training dataset for parameterization of the forcefield. MgC_2, MgH_2, MgO, $MgCO_3$, and $Mg(OH)_2$ are crystal structures. $Mg^{2+}[H_2O]_6$ and $Mg^{2+}[H_2O]_6[H_2O]_2$ are magnesium-water clusters consisting first and second shell of waters, respectively. Magnesium-water clusters are only used to fit the aqueous forcefield, while crystal structures are used for both aqueous and interfacial forcefields. The Mg-O-O angles are the angles between water and magnesium in the first and second hydration shells.

structure	lattice constants	atomic configuration	bulk modulus	bond distance	angle value	hydration energy
MgC_2	x	x				
MgH_2	x	x	x			
MgO	x	x	x			
$MgCO_3$	x	x	x			
$Mg(OH)_2$	x	x	x			
$Mg^{2+}[H_2O]_6$				Mg-Ow	Mg-Ow-Ow	x
$Mg^{2+}[H_2O]_6[H_2O]_2$				Mg-Ow	Mg-Ow-Ow	x

significant role in water adsorption energies on crystal surfaces, we decided to parameterize two separate force fields: 1) The aqueous FF with magnesium charge fixed to +2, which is suitable for aqueous magnesium carbonate systems, and 2) The interfacial FF, for which we fit the magnesium charge to the geometrical and mechanical properties of magnesium-containing solids and can be used for crystalline solids and their interfaces with water. Note that we only used the Mg-water cluster to fit the aqueous FF and not the interfacial FF. Also, the charge of magnesium in the interfacial FF is fitted in the second step of each iteration.

Magnesium-water clusters are simulated using the Gaussian16 code[176]. B3LYP exchange-correlation functional[177,178] is used with the large 6-311++G(2d,2p) basis set. Berny optimization method[179] is used with the Tight option and Ultrafine integration grid[180] to ensure convergency is reached for clusters with soft degrees of freedom. Dispersion correction is applied using the DFT-D3 method of Grimme[181,182].

To calculate surface hydration energies, we implement Vienna Ab-initio Simulation Package (VASP)[183]. Projector augmented wave (PAW) potentials[184] are used with the kinetic cut-off energy of 520 eV. The Perdew-Burke-Ernzerhof (PBE) generalized gradient approximation (GGA) is used as the exchange-correlation functional[107]. Also, van-der-Waals dispersion forces are considered using the DFT-D3 method of Grimme. For the crystal surfaces, 2x2x1 mesh points are used to sample the K-space using Monkhorst-Pack scheme. Conjugate gradient method is used for geometry optimization. For simplicity, we refer to the DFT methods used for cluster and surface calculations as B3LYP-D3 and PBE-D3 respectively.

Table 3.2. Fitted interatomic potential parameters to be incorporated with REAXFF. The Mg-H and Mg-C interactions are modelled with Buckingham potential (eq 3) and the Mg-O interaction is modelled with Lennard-Jones (LJ) 12-6 potential (eq 4). Gamma is the screening parameter used in Coulombic interaction according to eq. 2.

Interaction	Aqueuos Forcefield						Interfacial Forcefield					
	q_{Mg}	γ ($Å^{-1}$)	A_{lj}(ev.$Å^{12}$)	B_{lj}(ev.$Å^{6}$)	A_{buck} (ev)	ρ_{buck} (Å)	q_{Mg}	γ ($Å^{-1}$)	A_{lj}(ev.$Å^{12}$)	B_{lj}(ev.$Å^{6}$)	A_{buck} (ev)	ρ_{buck} (Å)
Mg Coulomb	2.00	0.55	-	-	-	-	1.2846	0.5298	-	-	-	-
Mg-H	-	-	-	-	293.366	0.289894	-	-	-	-	246.154	0.2572
Mg-C	-	-	-	-	320.9	0.37	-	-	-	-	240.6954	0.3228
Mg-O	-	-	3704.1911	44.480255	-	-	-	-	3646.7034	53.5115	-	-

Table 3. Water binding energies (eV) calculated for $[Mg(H_2O)_n](H_2O)_m^{2+}$. n and m refer to the number of water molecules in the first and second shell respectively. Hydration energy (E_{hyd}), binding energy (E_{bind}), and successive (ΔE) binding energy are calculated based on Eqs. 8, 9, and 10, respectively.

Cluster	E_{hyd} ReaxFF (aq) (eV)	E_{bind} ReaxFF (aq) (eV)	ΔE ReaxFF (aq) (eV)	E_{hyd} ReaxFF (int) (eV)	E_{bind} ReaxFF (int) (eV)	ΔE ReaxFF (int) (eV)	E_{hyd} B3LYP-D3 (eV)	E_{bind} B3LYP-D3 (eV)	ΔE B3LYP-D3 (eV)	E_{bind} B3LYP [a](eV)	ΔE B3LYP[a] (eV)	E_{bind} Non-Reactive FF (eV)	ΔE Non-Reactive FF(eV)
n = 2, m = 0	-5.42	-5.67		-3.21	-3.47		-6.59	-6.83		-6.61		-4.76[d], -5.95 [e]	
n = 3, m = 0	-7.49	-8.08	-2.41	-4.33	-4.92	-1.45	-8.66	-9.43	-2.59	-9.00	-2.39	-6.93[d], -8.15[e]	-2.17 [d], -2.77 [e]
n = 4, m = 0	-9.47	-10.15	-2.07	-5.43	-6.13	-1.21	-10.47	-11.53	-2.11	-10.90	-1.90	-8.92[d], -9.97 [e]	-1.98 [d], -2.44 [e]
n = 5, m = 0	-10.15	-11.57	-1.41	-5.43	-6.84	-0.71	-11.29	-13.02	-1.49	-12.11	-1.21	-10.34[d], -11.2 [e]	-1.42 [d], -1.57 [e]
n=6, m = 0	-10.98	-12.84	-1.27	-5.60	-7.46	-0.62	-12.10	-14.39	-1.37	-13.18	-1.06	-11.77[d], -12.22[e]	-1.43 [d], -1.52 [e]
n=6, m = 1[b]	-11.68	-14.05	-1.21	-6.51	-8.03	-0.56	-12.55	-15.32	-0.92	-13.96	-0.78		
n=6, m = 1[c]	-11.64	-14.01	-1.17	-6.60	-8.12	-0.65	-12.62	-15.38	-0.98	-14.00	-0.82	-12.6[d], -12.64[e]	-0.83[d], -0.93 [e]
n=6, m =2	-12.09	-15.03	-1.02	-5.80	-8.74	-0.62	-13.21	-16.22	-0.84	-14.62	-0.66	-13.31 [d], -12.93[e]	-0.71[d], -1.06 [e]

[a] From [39]. [b] one hydrogen bond. [c] two hydrogen bonds. [d]core-shell potential[24] [e]Thermodynamically consistent potential[25]. (aq) refers to aqueous and (int) refers to interfacial forcefields.

3.3 Results and discussion

3.3.1 Solvation Structures and Energies**:** The final fitted parameters derived according to the procedure described in the Methods section are presented in **Table 3.2**. These parameters should accompany the ReaxFF library provided in **Appendix B**. The hydration energies of magnesium are calculated for clusters up to eight water molecules, as shown in **Table 3.3 and Fig. 3.1**. The total hydration energy, E_{hyd}, the binding energy, E_{bind}, and the difference in the energies if one water molecule was added to the cluster, ΔE, are calculated based on the following relationships:

$$E_{hyd} = E\{Mg(H_2O)_n^{2+}\} - E\{(H_2O)_n\} - E(Mg^{2+})\} \quad (8)$$

$$E_{bind} = E\{Mg(H_2O)_n^{2+}\} - nE\{(H_2O\} - E(Mg^{2+})\} \quad (9)$$

$$\Delta E = E\{Mg(H_2O)_n^{2+}\} - E(H_2O) - E\{Mg(H_2O)_{n-1}^{2+}\} \quad (10)$$

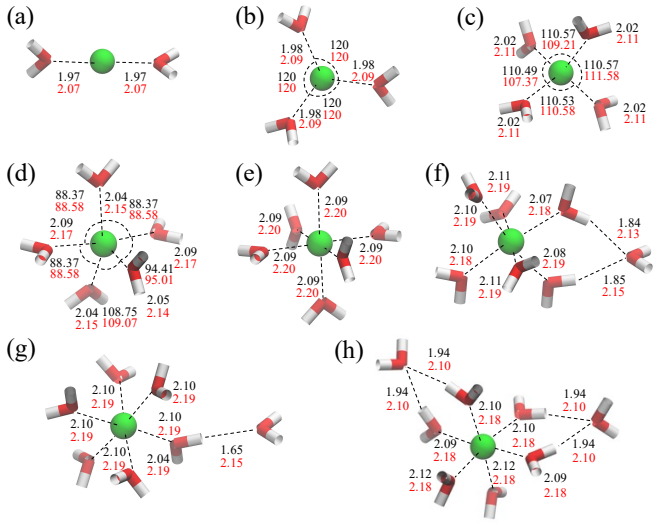

Figure 3.1. Mg2+-water clusters. a) $Mg^{2+}(H_2O)_2$ b) $Mg^{2+}(H_2O)_3$ c) $Mg^{2+}(H_2O)_4$ d) $Mg^{2+}(H_2O)_5$ e) $Mg^{2+}(H_2O)_6$ f) $Mg^{2+}(H_2O)_6(H_2O)$ The water molecule in the second shell has one hydrogen bond with a first-shell water molecule g) Mg^{2+}-$(H_2O)_6(H_2O)$. The water molecule in the second shell has two hydrogen bonds with two first-shell water molecules h) Mg^{2+}-$(H_2O)_6(H_2O)_2$. The black and red values respectively refer to B3LYP-D3 and ReaxFF calculations. Mg atoms are shown by green balls, and water oxygen and hydrogen atoms are colored as red and white sticks, respectively.

The difference between total hydration energy and binding energy is that the energy of a cluster of water molecules is used in the hydration energy while the energy of a single water molecule is used in the calculation of binding energies. The dispersion correction used in our B3LYP-D3 calculations can affect the water cluster energies. The magnitude of the binding energies (E_{bind}) calculated from our B3LYP-D3 calculations are larger than those previously calculated from B3LYP calculations[127] without dispersion corrections. The discrepancy in binding energies is expected when we use dispersion correction that was shown to more accurately capture van der Waals interactions and hydrogen bonding[185–187]. $|\Delta E|$ reduces as the number of water molecules increases in ReaxFF and DFT. Also, as the number of water molecules increases, the error in ReaxFF hydration energies compared to DFT results reduces. This is due in parts to the charge equalization scheme in ReaxFF that tends to uniformly distribute charges, therefore working better for larger clusters where charges are less localized.

We also provide in **Table 3.3** the binding energies resulted from two known non-reactive potentials. One is the core-shell potential developed by Kerisit and Parker[188], which is successfully used to study the free energy of metal cation (Sr, Mg, Ca) adsorption on the surface of calcium carbonate crystal. The other is the thermodynamically consistent forcefield developed by Raiteri et al.[160] to model alkaline-earth carbonates in water.

As reported in **Table 3.3**, our reactive forcefield gives more accurate results than both non-reactive forcefields for the binding energies of clusters with equal or more than 4 water molecules. This roots back in the charge equalization method implemented in our forcefield that does not perform accurately for localized charges, whereas for the systems with more distributed charges it is shown to be more reliable. The energy difference in binding energies (ΔE) are captured well through both

Table 3.4. Bond distances between Mg^{2+} and water oxygen derived from ReaxFF and DFT in $[Mg(H_2O)_n]^{2+}$ clusters.

Cluster	Mg-Ow (Å) ReaxFF	Mg-Ow (Å) B3LYP-D3	Mg-Ow (Å) B3LYP*
n = 2	2.07	1.95	1.95
n = 3	2.09	1.97	1.97
n = 4	2.11	2.02	1.99
n = 5	2.15, 2.17	2.04, 2.09	2.03,2.07
n=6	2.20	2.09	2.08

* From [39].

reactive and the non-reactive forcefields especially when we add water molecules to the first shell of magnesium. When we add water to the second shell, although binding energies calculated from our reactive forcefield are within a good range of binding energies calculated from DFT-D3, we observe larger discrepancy in ΔE. This can be the result of limited charge screening in our forcefield due to the fixed magnesium charge. Same is true for the Raiteri et al.'s forcefield with fixed charges, whereas the Kerisit and Parker's forcefield is more consistent in calculating ΔE, due to the polarizability of water molecules provided by the core-shell model. Also, we report the hydration and binding energies of magnesium-water cluster calculated from our interfacial forcefield in **Table 3.3**. As shown in the table, the interfacial reactive forcefield gives much less accurate results when compared to the aqueous ReaxFF due to the smaller Mg charge.

The distance between Mg^{2+} and water oxygens in $Mg(H_2O)_n^{2+}$ as obtained from ReaxFF, our DFT simulations, and a previous DFT work[127] are presented in **Table 3.4**. Our B3LYP-D3 calculations show slightly larger bond lengths between magnesium and the water oxygens compared to previous B3LYP calculations. Similar overestimations were observed for the Na^+-water bond lengths when dispersion correction was implemented[189]. On the other hand, ReaxFF gives

Table 3.5. Lattice properties and bulk modulus for magnesium containing crystals calculated from two fitted ReaxFF forcefields, compared to experiments.

Crystal Formula	Aqueous forcefield			Interfacial forcefield			a (Å)-exp.	c (Å)-exp.	K (GPa)-exp
	a (Å)	c (Å)	K (GPa)	a (Å)	c (Å)	K (GPa)			
Brucite	12.17	14.42	60	12.35	12.85	73	12.57	14.3	46
Magnesia	8.62			8.96			8.94		
Magnesite	5.94	17.83	163	6.11	18.36	105.18	5.67	17.02	110
Magnesium Hydride	18.69	15.25	58.8	18.69	15.77	21	17.94	15	51
Magnesium Carbide	16.78	15.71		17.22	14.92		15.74	15.06	
Nesquehonite	22.52	24.25		23.39	24.22		23.10	24.25	
Dolomite	24.57	6.14		25.00	6.25	96	24.05	6.013	94
Diopside	12.87	15.95		13.17	15.87		13.20	15.75	

acceptable bond distance values, although in general overestimates them. The Mg-Ow bond lengths increase as the number of water molecules increases, in agreement with DFT results.

3.3.2 Crystal structures**:** The resulting fitted parameters are used to calculate the lattice properties and bulk moduli of a list of magnesium-containing solid phases, as shown in **Table 3.5**. Along with the crystals used in the fitting procedure, few other crystal structures are selected to evaluate the transferability of the derived FF beyond the geometrical and mechanical observables used in the parameterization process. Here, we present the calculated crystal structures based on both aqueous and interfacial FF to show the impact of setting magnesium charge to a value less than+ 2 as expected for covalent-ionic systems.

As shown in **Table 3.5**, magnesite lattice parameters are reproduced with acceptable accuracy with both forcefields compared to experimental results. However, the bulk modulus is best captured with the interfacial FF with an underestimation of about 9%, while the aqueous FF produces poor results. The elastic constant, C_11, is calculated to be 168 GPa for magnesite according to our

interfacial FF, which is reasonable compared to DFT calculations with GGA functional. However, it deviates from the DFT-LDA results overall gives better results when compared to experiments[190]. Surprisingly, the elastic constants in the ab plane, C_{12}, and C_{13}, are very accurately calculated compared to DFT-LDA and experiments. However, $C_{11}+C_{12}$ differs a lot from the experimental value of 334 GPa[190]. Also, C_{33} is calculated to be 165 GPa compared to the experimental value of 156 GPa. We note that our reactive interfacial FF gives reasonable results for the mechanical properties of magnesite when compared to the non-reactive thermodynamically consistent FF[160] that cannot properly capture the bulk modulus. It can be attributed to the choice of the magnesium charge that is taken less than +2.

The structure and mechanical properties of dolomite which were not part of the training set are calculated, and the results are shown in **Table 3.5**. Calcium parameters are taken from a previously fitted reactive FF for aqueous calcium carbonate systems with a fixed calcium charge of 2.[161] Compared to experimental values, the lattice parameters are overestimated by about 4% and 2%, respectively, for the interfacial and aqueous forcefields[191]. Based on the interfacial forcefield, the calculated bulk modulus is 96 GPa based on Voigt definition, slightly overestimating the experimental value of 94 GPa[192]. The aqueous FF gives poor results when it comes to the mechanical properties of dolomite. Based on our interfacial FF, the C_{11} constant is 183 GPa compared to 204 GPa based on Brillouin zone spectroscopy measurements[193]. Also, the calculated C_{33} constant is 96 GPa agrees well with the experimental value of 97 GPa. However, the rest of the elastic constants that are calculated by our forcefields are less accurate.

The rest of the solid phases in **Table 3.5** are reasonably reproduced with both aqueous and interfacial forcefields in terms of lattice constants. Interestingly, brucite lattice constants are better

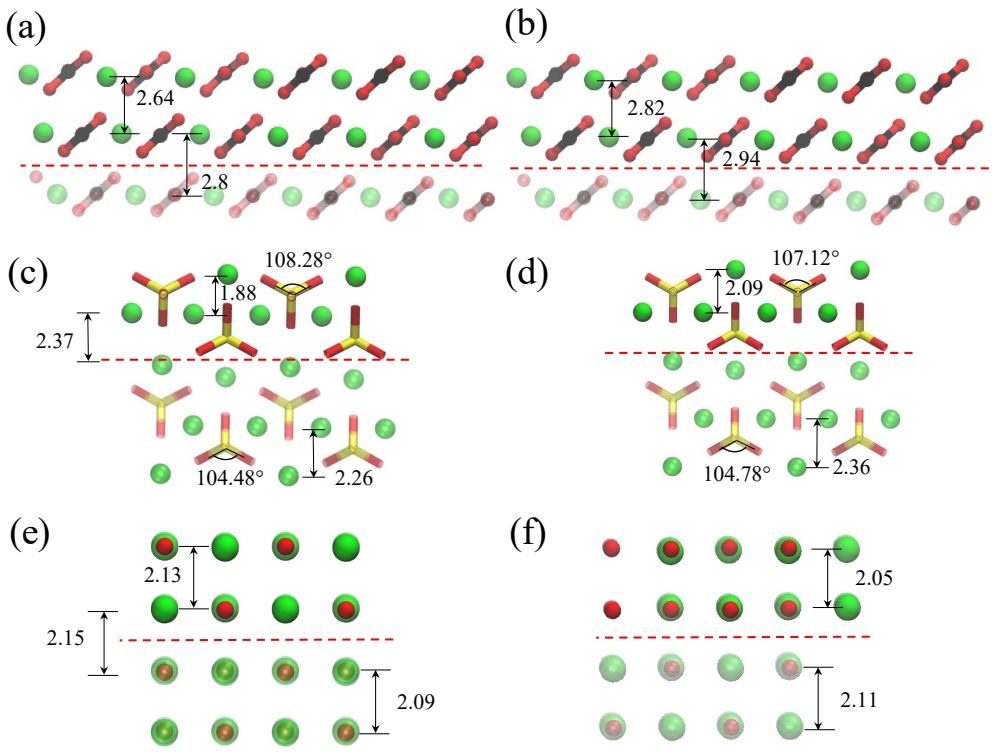

Figure 3.2. The dry surface of magnesite, forsterite, and magnesia. a) The dry $(10\bar{1}4)$ surface of magnesite calculated from PBE-D3. The distance between magnesium layers in the bulk phase is 2.77 Å. b) The dry $(10\bar{1}4)$ surface of magnesite as calculated with ReaxFF. The distance between magnesium layers in the bulk phase is 2.80 Å. c) The dry (010) surface of forsterite calculated from PBE-D3. d) The dry (010) surface of forsterite calculated from ReaxFF. e) The dry (100) surface of magnesia (MgO) calculated from PBE-D3. f) The dry (100) surface of magnesia (MgO) calculated from ReaxFF. The black and red values refer to PBE-D3 and ReaxFF calculations, respectively. The atoms below red dashed lines are fixed, while the top atoms are able to move. Magnesium, carbon, oxygen and silicon colored as green, black, red and yellow, respectively. Distances are in Angstroms.

captured with the aqueous FF. Especially in the *c* direction where the structure is layered, the lattice constant is only 1% deviating from the experiment , compared to the 10% underestimation of the interfacial FF. This discrepancy can be explained by the lower Mg-Ow bond lengths in the magnesium-water clusters used in the parameterization of the aqueous FF.

3.3.3 Surface hydration**:** The interaction of water with metal-containing rocks is crucial to understand CO_2 sequestration[194], electrochemical reactions[195], and accretion of the Earth from the water adsorption on dust grains[93,196], etc. However, our knowledge of the mineral-water interface

is limited due to experimental and theoretical difficulties. Here, we select three crystals, namely forsterite, magnesite, and magnesium oxide, to examine the fitted FF to predict the geometric structure of dry and hydrated surfaces. We use (010) cleaved surface of forsterite which was previously shown to have the lowest surface energy[94]. For magnesite, we choose the $(10\bar{1}4)$ surface cleavage that is shown by scanning electron microscopy analyses to be the dominant surface[197]. For MgO, we choose the (001) surface. Only the top two layers of magnesium in all crystals are allowed to move while fixing the bottom layers to represent the bulk-like crystals.

The dry surfaces are relaxed using DFT and the interfacial reactive forcefield, as shown in **Fig. 3.2. a-f**. On the forsterite surface, the top magnesium layer displaces toward the bulk phase for about 0.26 Å and 0.29 Å using DFT and ReaxFF, respectively. This results from the fact that the surface magnesium is undercoordinated and is attracted toward the negatively charged oxygens in the bottom layer. Also, the second top magnesium layer displaces slightly toward the surface for about 0.11 Å and 0.02 Å using DFT and ReaxFF, respectively. ClayFF, a classical FF with fixed charges, shows a displacement of 0.34 Å toward the bulk phase and 0.05 Å toward the surface for the first and second magnesium layers. The top silicon atoms move upward for about 0.19 Å, and the oxygen-silicon-oxygen angle changes from 104.48º to 108.28º. Using ReaxFF, the top silicon atoms move outward for about 0.07 Å, and the angle changes from 104.78º to 107.12º. This results from the lower equilibrium bond distance between undercoordinated magnesium and silicate oxygens. Also, the angle change can significantly reduce the stability of surface silicate groups and can potentially give rise to the production of carbonate groups when CO_2 is in the surface vicinity. DFT results are in close agreement with a previously reported DFT work[77] that used D2 dispersion correction.

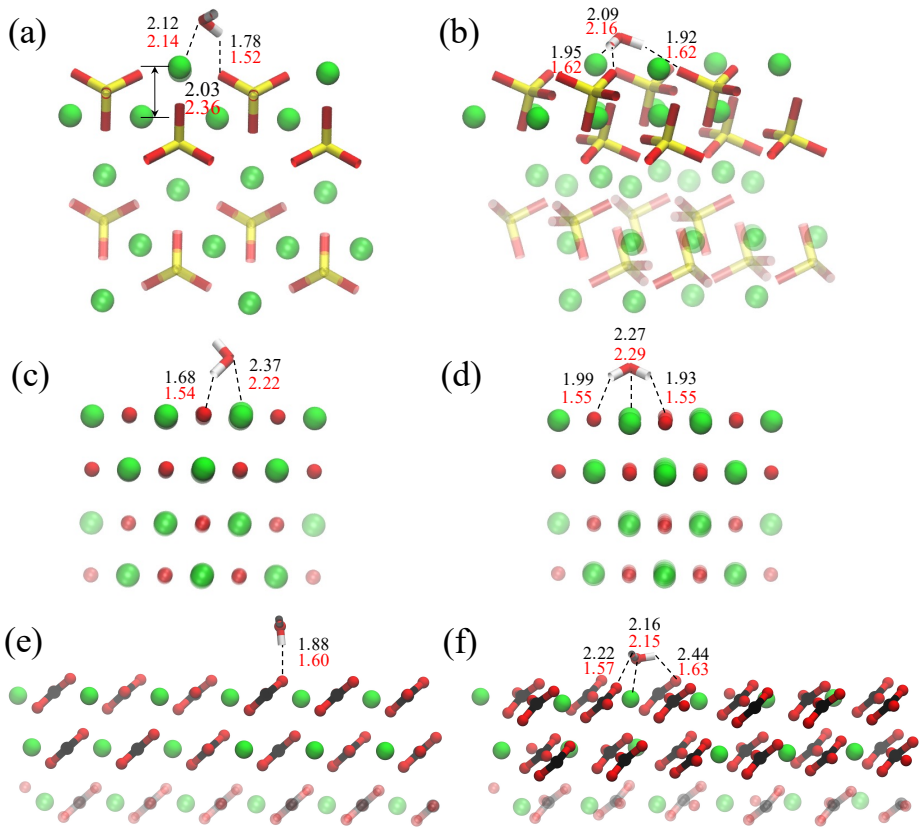

Figure 3.3. The hydrated surface of magnesite, forsterite, and magnesia. The adsorption of water on the (010) surface of forsterite with a) side and b) flat configurations. The adsorption of water on the (100) surface of magnesia with c)side and d) flat configurations. The adsorption of water on the $(10\bar{1}4)$ surface of magnesite with e) side and f) flat configurations. The transparent atoms are held fixed during the simulation, while the rest of the atoms are free to move. Magnesium, carbon, oxygen and silicon colored as green, black, red and yellow, respectively. The distance values in black and red are derived from PBE-D3 and ReaxFF. Distances are in Angstroms.

The surface features of carbonate minerals like calcite, magnesite, and dolomite are important for modeling the dissolution/precipitation processes in the geological carbon cycle. Magnesite and dolomite surface reactivity has been investigated experimentally using surface complexation models[197,198]. However, reactive molecular simulations are yet applied to study these problems. According to our calculations on the magnesite's dry surface, slight displacement is found on the $(10\bar{1}4)$ surface, compared to Calcite ($CaCO_3$) which has a lower bulk modulus of about 73.5 GPa[199]. Upon DFT calculations, the first magnesium layer moves toward the bulk phase by about 0.11 Å, and the second magnesium layer moves away from it by 0.03 Å. With ReaxFF, the first

magnesium layer moves toward the inner layers by about 0.1 Å, and the second magnesium layer moves away from the bulk phase by 0.02 Å, in full agreement with the DFT calculations. The CO_3 also distorts slightly like akin to the observations in the DFT simulations.

We also test our FF to reproduce the MgO (001) surface. MgO has critical industrial applications such as heterogeneous catalysis and concrete construction[200–202]. Based on our calculation, the anhydrous (001) surface of MgO changes only slightly. Based on our DFT calculations, we observe that the first magnesium layer displaces 0.16 Å out of the surface, while the second layer displaces only for 0.06 Å. Our ReaxFF simulations underestimate the displacement of the first and second magnesium layers by 0.09 Å and 0.05 Å, respectively.

After relaxing the dry surfaces, we add a water molecule on top of crystal surfaces and relax them using PBE-D3 and ReaxFF. Two configurations of water are found on each crystal surface, as shown in **Fig. 3.3.a-f** without dissociating. On the forsterite (010) surface, a water molecule can either donate a hydrogen bond to a onefold coordinated silicate oxygen or donate two bonds to two onefold coordinated silicate oxygen as shown, respectively in **Fig. 3.3.a** and **Fig. 3.3.b**. We call the former case "side water" and the latter case "flat water". In both cases, the water oxygen is found coordinated around a surface magnesium. The adsorption energy based on PBE-D3 calculations for the "side water" and the "flat water" are respectively -0.90 eV and -1.34 eV. The calculated adsorption energies are less exothermic than those calculated through DFT with D2 dispersion correction, which produced -1.48 eV and -1.42 eV for "flat water" and "side water" configurations, respectively[77].

The adsorption energies for the "flat water" and "side water" configurations based on ReaxFF are -2.38 eV and -1.6 eV, respectively. The aqueous FF gives even worse predictions about twice the

amount for the interfacial FF, although the former gives accurate hydration energies of solvated magnesium in water. Although assigning a charge less than +2 to the less ionic magnesium in the crystal partially resolves this problem, we believe that the observed difference in water adsorption energies between PBE-D3 and ReaxFF roots in the hydration of silicate groups. The lower ReaxFF hydroxylation energy of water on silicates compared to DFT calculations[203] support the evidence. This discrepancy can be alleviated by further improving ReaxFF's Si/O/H parameter set to include water geometry and adsorption energy on silicates.

For the case of "side water," surface magnesium is displaced away from the surface by 0.45 Å and 0.27 Å calculated from PBE-D3 and ReaxFF, respectively, most probably due to the charge transfer caused by the water molecule. Using interfacial ReaxFF, the length of the donated hydrogen bond for the "flat water" is underestimated by about 0.3 Å compared to our PBE-D3 results. Also, the bond between surface magnesium and the water oxygen is overestimated by about 0.02 Å and 0.07 Å for the "side water" and "flat water," respectively, using the interfacial reactive FF compared to the PBE-D3 simulations. This difference is due to the overestimated magnesium-water bond distance in our parameterization. The donated hydrogen bond in the "side water" configuration is 0.2 Å shorter in ReaxFF compared to PBE-D3. However, the magnesium water distance, in this case, is only 0.02 Å overestimated with ReaxFF compared to DFT.

Similar to the forsterite surface, the hydrogen bonds on the MgO surface are shorter when modeled with ReaxFF compared to PBE-D3, as shown in **Fig. 3.3.c-d**. The hydrogen bond formed between the water hydrogen and the undercoordinated oxygen on the surface is 1.54 Å resulted from ReaxFF, compared to the 1.68 Å calculated via PBE-D3. Contrary to forsterite cases, the magnesium-water distance on MgO surface is underestimated by ~0.15 Å. Also, the hydrogen

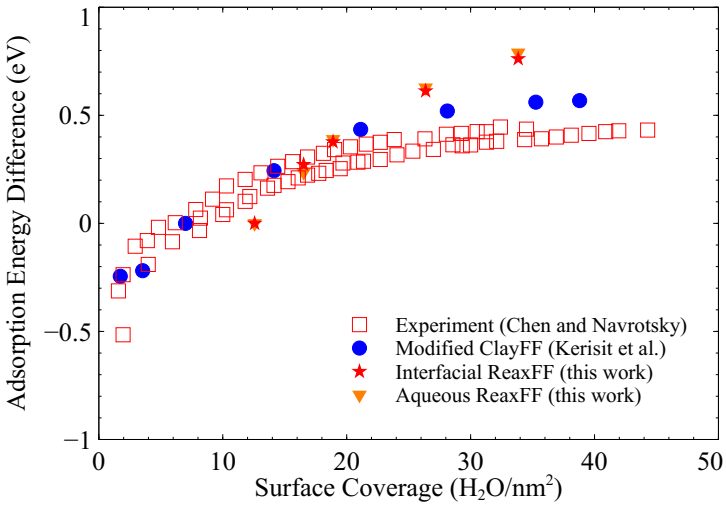

Figure 3.4. The monolayer water adsorption energy difference on the surface of forsterite from simulations and experiments. The energy difference refers to the adsorption energy of n monolayers of water subtracted by the adsorption energy of one monolayer water (n= 2,3,4,5).

bonds of the "flat water" case are shorter by almost ~0.45 Å in ReaxFF compared to PBE-D3 values, although the magnesium oxygen bond is properly calculated. This shows that the water dipole moment is more oriented toward the surface in ReaxFF. According to our energy calculations at 0 K, the structure of "side water" is more stable than "flat water" opposite to the forsterite adsorption cases. The adsorption energies derived using PBE-D3 are -0.42 eV and -0.48 eV for "flat water" and "side water", respectively. Similar to the forsterite surface, the adsorption energies from interfacial ReaxFF are more exothermic than adsorption energies resulted from PBE-D3 by -1.38 eV and -1.70 eV.

On the surface of Magnesite, the adsorption energies for the "flat water" and "side water" with PBE-D3 are -0.64 eV and -0.19 eV, respectively. However, ReaxFF-derived adsorption energies for "flat water" and "side water" are -1.55 eV and -0.48 eV overestimating their magnitude compared to their corresponding values from PBE-D3 calculations. The magnesium distance to

the water oxygen simulated from ReaxFF is close to its value from PBE-D3, although the hydrogen bond distances are smaller in ReaxFF than PBE-D3.

Moving away from the single water adsorption, we examine the cases where 1 to 5 monolayers of water exist on the (010) surface of forsterite. In the corresponding ReaxFF simulations, all the one-folded silicate oxygen atoms become hydrated. Moreover, previous DFT simulations of the (100) surface of MgO have shown that a complete monolayer of water hydroxylates the surface[204]. We calculate the adsorption energy for various monolayers on the surface of forsterite, as demonstrated in **Fig. 3.4.** Since the adsorption energy of the first monolayer was substantially high due to interactions with the silicates, we only present the difference in the adsorption energy of *n* water monolayers (*n*=2,3,4,5) and the adsorption energy of one monolayer. Comparison with experiment and modified ClayFF potential[75], a non-reactive forcefield, shows that two and three monolayers of water give the best adsorption energies when subtracted from the adsorption energy of a single monolayer, and it is in an acceptable experimental range when four and five monolayers are present on the surface.

3.3.4 Ion Pairing**:** The formation of $MgCO_3$ and $[MgHCO_3]^+$ ion pairs in the solution is a precursor for the nucleation of magnesium carbonate[84,205]. However, the molecular mechanism that leads to the nucleation and growth of crystalline or amorphous magnesium carbonate phases at different thermodynamic conditions and thin water films is not known[84,150,151,153,206]. Also, the attachment of carbonate to the surface magnesium on crystals like forsterite can lead to dissolution, known as ligand-promoted mineral dissolution[207]. Therefore, studying the energetics of the pairing reactions becomes crucial to understand homogeneous and heterogeneous nucleation and growth[36].

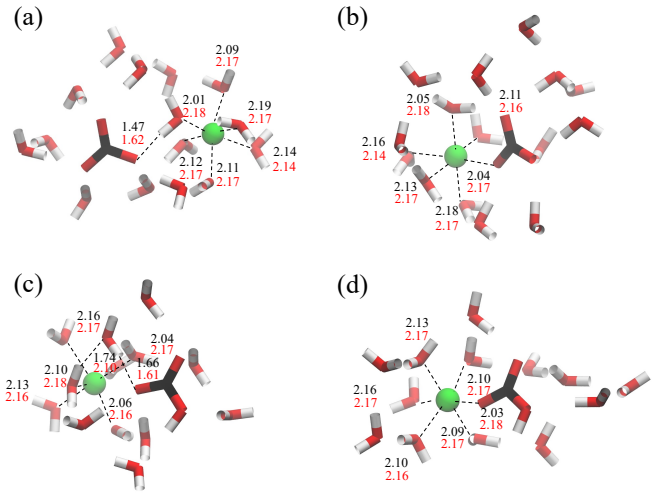

Figure 3.5. Magnesium-(bi)carbonate ion pairing clusters. a) Mg-CO_3 Solvent separated ion pair. b) Mg-CO_3 contact ion pair. c) $[Mg\text{-}HCO_3]^+$ Solvent separated ion pair d) $[Mg\text{-}HCO_3]^+$ contact ion pair. The distance values in black and red are derived from PBE-D3 and ReaxFF, respectively. Distances are in Angstroms.

Here, we examine the fitted aqueous FF to model the structure of the separated ions (SI), solvent separated ion pairs (SSIP), and contact ion pairs (CIP) and their relative potential energy. We use recent geometries[35] calculated by DFT for hydrated Mg^{2+} and HCO_3^-/CO_3^{2-} in SI, SSIP, and CIP form as initial structures and relax them using energy minimization with our aqueous reactive FF. The resulting structures are shown in **Fig. 3.5.a-d**. The relative energies between SSIP and CIP structures from our reactive simulations are compared to MP2/aD level and B3LYP/aD level calculations[35] in **Table 3.6**. As shown, the relative energies derived from our FF are within the acceptable range of the DFT results. However, SSIP structures are more stable than CIP contrary to the DFT results and infrared spectroscopic measurements in the solution[208]. Nevertheless, nucleation either takes place in the solution or at the mineral-water interface. Therefore, it is essential to test the FF in the solution and measure the relative stability of SSIP and CIP structures.

To this end, we construct a cubic box containing 560 water molecules and run MD at 298.15 K. First, we relax the cell in constant isobaric isothermal ensemble (NPT) using the Nose-Hoover

Table 3.6. Reaction energies for the conversion of Seperated Ions (SI) to Contact Ion Pair (CIP) and Solvent Separated Ion Pair (SSIP) calculated from ReaxFF compared to DFT results with B3LYP/aD and MP2/aD functionals.

	MP2/aD* (kcal/mol)	B3LYP/aD* (kcal/mol)	ReaxFF (kcal/mol)
SI to CIP (CO_3)	-348.6402	-339.2884	-235.9648
SI to CIP (HCO_3)	-216.0981	-212.1398	-141.6936
SI to SSIP (CO_3)	-331.5982	-325.8616	-236.1492
SI to SSIP (HCO_3)	-200.5453	-192.3124	-148.0037

* Results from [10]

thermostat and barostat with 0.5 fs timestep and relaxation time of 10 fs. Upon convergence in the box dimensions, we relax the system in canonical ensemble (NVT) at 298.15 K. Then, we place one magnesium ion and one carbonate ion at some distance in the solution and run MD for 6 ns. We observe that the relative distance between the two ions changes during the course of the simulation, and at random periods the two ions form an SSIP structure. In this simulation, we do not observe the formation of CIP structure as it is not expected to occur at room temperature due to the very rigid hydrated structure of magnesium and the limited MD timescales. Alternatively, we initialize the MD simulation with CIP structure and run for 6 ns. The CIP structure remained stable during the simulation. Also, the magnesium atom in the CIP structure has five water molecules, one water molecule less than the SSIP structure in agreement with experiments and FF calculations[160,209]. The CIP structure was on average 0.09 eV lower than the SSIP structure, and 0.13 eV lower than the case where ions were at least 3 water molecules apart from each other, confirming the relative stability of the CIP structure compared to SSIP and SI in the solution. Our

results are consistent with the experiment that shows magnesium carbonate ion pair dissociates with 0.09 eV enthalpy difference[210].

3.4 Applications of Aqueous and Interfacial FFs:

3.4.1 H_2CO_3 dissociation in water with $Mg(OH)_2$**:** Atmospheric carbon dioxide naturally dissolves in water and partially reacts with it to produce carbonic acid and bicarbonate. The excess amount of CO_2 from burning fossil fuels can negatively impact natural processes, one of which is the acidification of the surface ocean. Carbonic acid dissociates to bicarbonate and proton, which reacts with carbonates on the oceanic surfaces that can severely slow down the growth of coral reefs[211]. However, alkaline earth metals can neutralize carbonic acid by forming carbonate minerals[212].

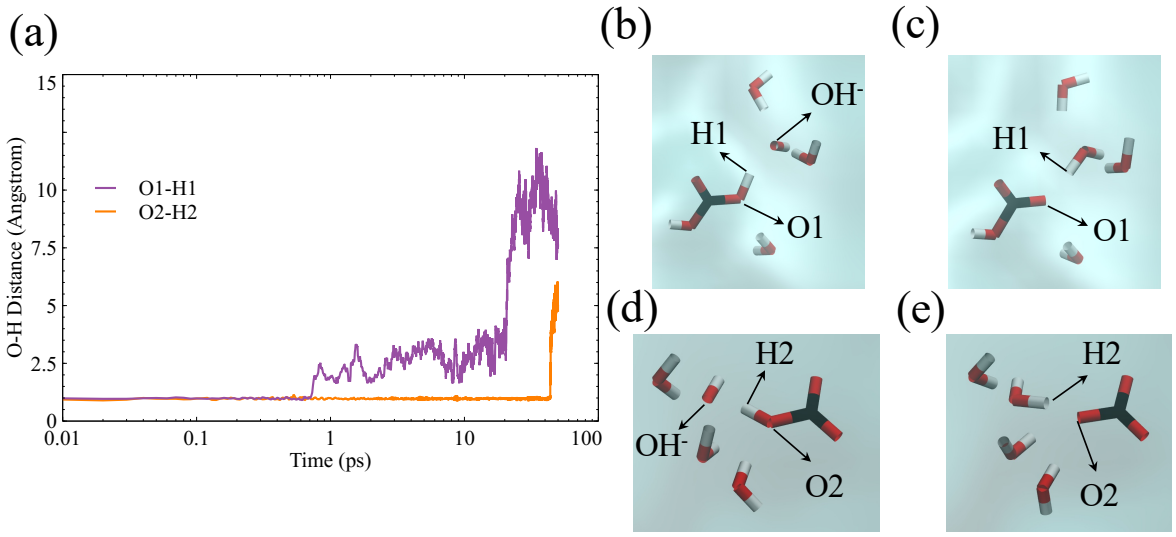

Figure 3.6. Carbonic acid dissociation in the presence of magnesium hydroxide. a) time-reaction for the deprotonation of carbonic acid. O1, H1, O2, and H2 are shown in the snapshots on the right. b) Carbonic acid in the solution before the reaction with the adjacent OH^- occurs c) Bicarbonate is formed as the product of the deprotonation of carbonic acid through reaction with solvated hydroxide ion. d) Bicarbonate in the solution before the reaction with the adjacent OH^- occurs e) carbonate is formed through the deprotonation of bicarbonate through reaction with a hydroxide. The cyan color in the background of snapshots represent the liquid water.

Here, we investigate the carbonic acid dissociation to bicarbonate and carbonate in the presence of dissolved magnesium hydroxide $Mg(OH)_2$ in the water using our reactive FF. To this end, we relax a neutral cell consisting of 250 water molecules, a carbonic acid molecule, and an $Mg(OH)_2$ ion pair in NPT ensemble at room temperature and zero pressure using Nose-Hoover thermostat and barostat with timestep of 0.25fs. After relaxation in NPT ensemble, we run the system in NVT ensemble. We first observe that the hydroxide initially coordinated around magnesium readily diffuses out into the solution through Grotthuss mechanism. Nevertheless, carbonic acid remained intact in about 2 ns. Adding another $Mg(OH)_2$ monomer, resulted in a fast reaction between carbonic acid with one of the hydroxide ions in less than 1ps to make bicarbonate as expected in such a basic solution, as shown in **Fig. 3.6.a-c**. After about 100 ps, the other hydroxide structurally diffuses toward the bicarbonate and grabs its proton and produces a carbonate ion, as shown **in Fig. 3.6.a** and **Fig. 3.6.d-e**. Obviously because the hydroxide concentration is ~ 13 order of magnitude greater than its concentration at pH of 14, we cannot expect the carbonic acid dissociation to occur this rapidly. However, our simulations show that the hydroxide, which diffuses structurally at a high rate in bulk water can reach to carbonic acid to make a spontaneous proton transfer reaction. With our reactive FF, we also observed the diffusion of surface hydroxide on metal divalent containing minerals toward the carbonic acid at the thin water film. The limited space in the nano-meter thin film in this system can substantially increase the rate of carbonic-acid-to-carbonate reaction, although the diffusion of hydroxide in the structured water is hindered. This is the subject of next section where we take brucite as a model surface to study this reaction.

We calculate the RDF for the three stages of the simulation described above. First, we fix the Ox-H bonds of the carbonic acid and proceed with the simulation and output the trajectories. Then, we unfix one of the Ox-H bonds and let the proton transfer happen to turn carbonic acid to bicarbonate, and run the simulation again to produce outputs of the trajectories. Finally, we unfix the remaining Ox-H bond of the bicarbonate until it turns into carbonate through another proton transfer reaction. Again, we run the simulation and output the trajectories. For all the stages, we run the simulations in NVT ensemble at room temperature using Nose-Hoover thermostat with timestep of 0.25 fs and relaxation time of 25fs. We output the trajectories every 25fs over the course of 500 ps to produce enough data for the radial distribution function (RDF) calculations. We also calculate the RDF for Mg-Ow for the two solvated magnesium cations. The resulting RDFs are shown in **Fig. 7. a-d**.

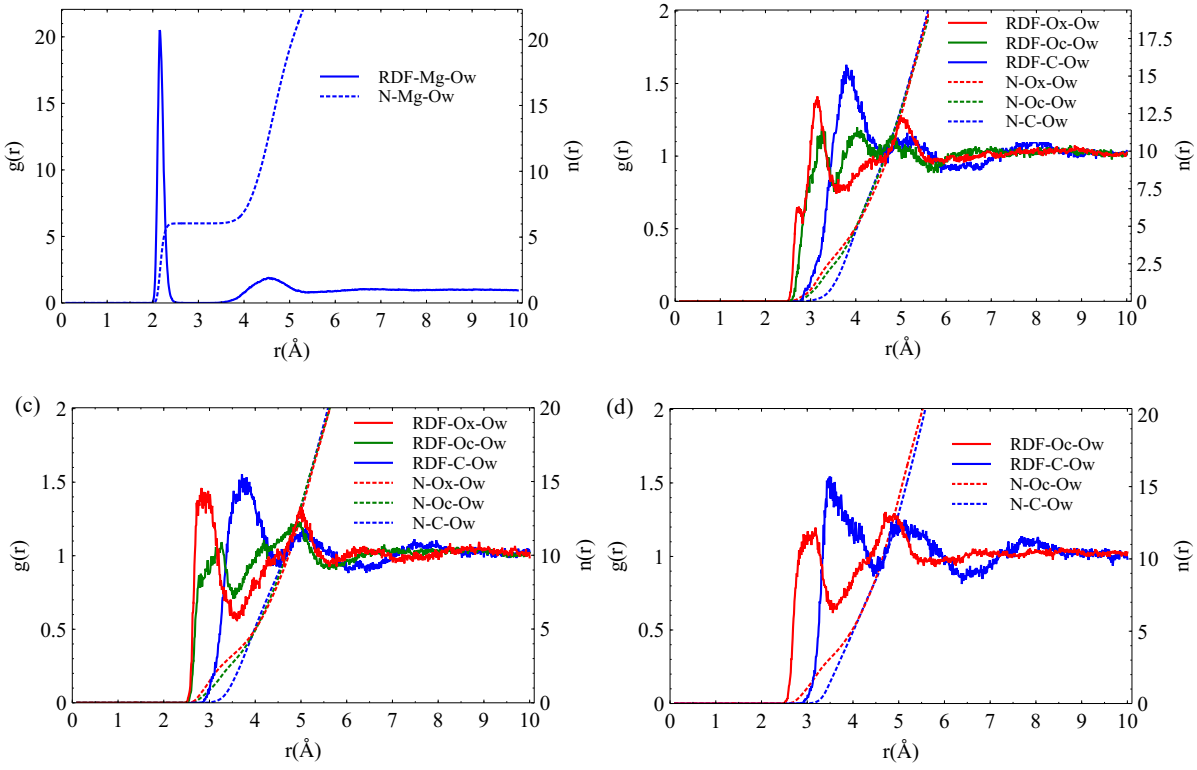

Figure 3.7. g(r) and coordination number, n(r), for (a) Magnesium (b) Carbonic Acid (c) Bicarbonate and (d) Carbonate in the solution. g(r) is shown with solid line and n(r) is shown with dashed lines in all figures. Ow, Ox and Oc refer to water oxygen, hydroxyl oxygen, and carbonyl oxygen, respectively.

The RDF for Mg-Ow has one sharp peak at around 2.15Å that corresponds to the first shell of water molecules that are tightly bound to the doubly charged magnesium cation as shown in **Fig. 3.7.a.** The water coordination number for magnesium is derived to be 6, which is in agreement with experiment[213] and previous simulations[160,214]. The carbonic acid contains two Ox and Oc which have different hydrogen bond networks as can be seen in the RDFs presented in **Fig. 3.7.b**. The first large peak for Ox-Ow is located at 3.13Å which corresponds to the hydrogen bond that are accepted by the carbonic acid hydroxyl groups. A smaller peak for Ox-Ow is observed at 2.75 Å that is related to the hydrogen bonds donated by the hydroxyl of the carbonic acid. The first peak for Oc-Ow is located at 3.25 Å. By integrating the RDFs up to 3.75 Å for the first shell of water molecules around Ox, a hydration number of 3.8 is derived, see n(r) in **Fig. 3.7.b**. The hydration number of Oc is 3.4, which is slightly smaller than that of Ox, due to the stronger hydrogen bonds around hydroxyl groups that both donate and accept hydrogen bonds. Probing the hydration structure of carbonic acid through experiment is difficult, because of its short lifetime. However, quantum mechanics/molecular dynamics (QM/MM) simulations of aqueous carbonic acid shows a hydration number of 3.17 for Oc, which is close to our calculated value of 3.4[215].

For the bicarbonate simulation, the RDF for carbonyl oxygen (Oc) and hydroxyl oxygen (Ox) are shown in **Fig. 3.7.c**. The first peak for Ox-Ow is almost at 2.9Å, while the first peak for Oc-Ow is slightly larger at around 3.1Å, due to the stronger hydrogen bond of the hydroxyl oxygen. By integrating the RDF for the first peak up to 3.75Å, the hydration number of Oc and Ox are derived to be 3.65 and 3.9, see the n(r) values in **Fig. 3.7.c.** These hydration numbers are both higher than their counterparts in carbonic acid. This is due to the charge of bicarbonate compared to the neutral carbonic acid as suggested by X-ray absorption spectroscopy measurements and Car-Parrinello

MD simulations[215,216]. However, our calculated hydration number for Oc is smaller than the derived value through QM/MM calculation which was 4.26[215]. This could in part results from the charge equalization method in ReaxFF that gives a lower charge magnitude of bicarbonate in our simulations, which is around -0.85 that its formal charge of -1.

We also calculate the RDF and hydration numbers for carbonate as shown in **Fig. 3.7.d.** The first peak for the Oc-Ow is located at around 3.0 Å. Forcefield calculations done by Bruneval et al.[217] shows the peaks to be in a lower range at 2.69. The hydration number for Oc of the carbonate is 4.08 if we integrate the RDF up to 3.75 Å. The forcefield calculation by Bruneval et al. shows a hydration number of 4.3, which like for the bicarbonate case could result from the lower charge magnitude of bicarbonate in our simulation (~ -0.9) that its formal charge of -2.

3.4.2 Bicarbonate-Brucite interaction**:** Ex-situ carbon mineralization can be achieved through the carbonation of mine wastes such as brucite [$Mg(OH)_2$] in mafic and ultramafic mines[147,218]. One study estimated that the accelerated carbonation of brucite in mine tailing could offset 22-57% of mine emissions[219]. Previously, we showed through reactive molecular dynamics simulations that the presence of surface hydroxide initiates a long-range proton transfer to deprotonate bicarbonate in the interfacial water film on forsterite surfaces. Here, we examine the interaction of bicarbonate at the water-brucite interface.

We construct a simulation cell containing a brucite slab and a slit pore filled with liquid water. We fix the inner layers of the brucite so that they represent the bulk structure, and we let the first two layers move and interact with the water molecules on top. The size of the box is 18.5Å*32.15Å*57.10Å in x, y and z direction, respectively. Then, we place a bicarbonate ion at the water-brucite interface and perform MD simulations in the NVT ensemble while fixing O-H

bonds in water and bicarbonate to relax the system. Then, we remove the constraint on the bonds and let the system evolve naturally. Similar to the hydroxylated (010) forsterite surface simulated through reactive molecular dynamics[220], we observe spontaneous diffusion of surface OH- groups in the water layers adsorbed to the surface.

Such proton transfer reactions were also observed on other oxide surfaces in both simulations and experiments. Through *ab initio* MD simulations[221], it was shown that the rate of proton transfer reactions at the water-ZnO $(10\bar{1}0)$ surface substantially increases when the number of water layers increases from one layer to a liquid multi-layer. Also, *ab initio*-based deep neural network analysis was able to show long-range proton transfer through water molecules at the water-TiO_2 interface[222]. Moreover, scanning tunneling microscopy experiments on FeO[223] and TiO_2[224] monolayers and single-molecule localization microscopy on defective boron nitride layers[225] unveil the proton transport at the solid-water interface. Recently, spectral single-molecule scanning tunneling microscopy and *ab initio* simulations[226] demonstrated higher proton diffusivity along the surface of boron nitride when it is in contact with a binary water-methanol solution rather than water- only solution.

After few picoseconds in our simulation on the brucite surface, we observe that a hydrogen-bond network forms between the bicarbonate and a surface hydroxide leading to a chain of proton transfer reactions that deprotonates the bicarbonate at the end, as shown in **Fig. 3.8.a-d**. The hydroxide ion structurally diffuses from the surface toward the bicarbonate in the interfacial water film. Structural diffusion, often called "Grotthuss diffusion," is the hopping of a proton from a hydronium ion to a neighboring water molecule or from a water molecule to a neighboring hydroxide. It involves breakage and formation of O-H bonds as the proton migrates between water

molecules. It is much faster than vehicular diffusion. The centers of charge and mass move together.[227] Similarly, hydroxide groups can structurally diffuse through water molecules as observed in biological systems and enzymatic reactions[228,229].

We also calculate the RDF for surface magnesium, carbonic acid, bicarbonate, and carbonate for the simulation on the surface of brucite. Initially, we fix the carbonic acid in the water layers 5Å away from the surface of brucite. To avoid spontaneous proton transfer that transforms the carbonic acid to bicarbonate and then to carbonate, we fix the O-H bonds of the hydroxyl group in carbonic acid. We run the simulation in NVT ensemble for 250ps, and output the trajectories every 25fs to produce data for RDF calculation. Other simulation settings are similar to those we used for carbonic acid deprotonation described in section 4-1.

The RDF for surface magnesium (Ms) and oxygen of water and surface hydroxide (O*) is shown in **Figure 3.8.e**. The first peak is located at 2.13Å, and a coordination number of 2.7 is derived for the first shell of O*, where two surface hydroxides are always present. The RDFs calculated for carbonic acid on the surface are shown in **Figure 3.8.f**. Like carbonic acid in the solution, the RDF for Ox-O* has two peaks close to each other, one at 2.6Å that corresponds to the accepted hydrogen bond and another at 3.12 that corresponds to the donated hydrogen bond. Interestingly, the hydration number for Ox is about 5.3 which is significantly larger than its counterpart in the solution which is 3.8. This can be the result of denser water layers with stronger hydrogen bonds compared to liquid water. This could also be the reason for the RDF for Oc-O* to have its first two peaks closer to each other than what we observe in the solution.

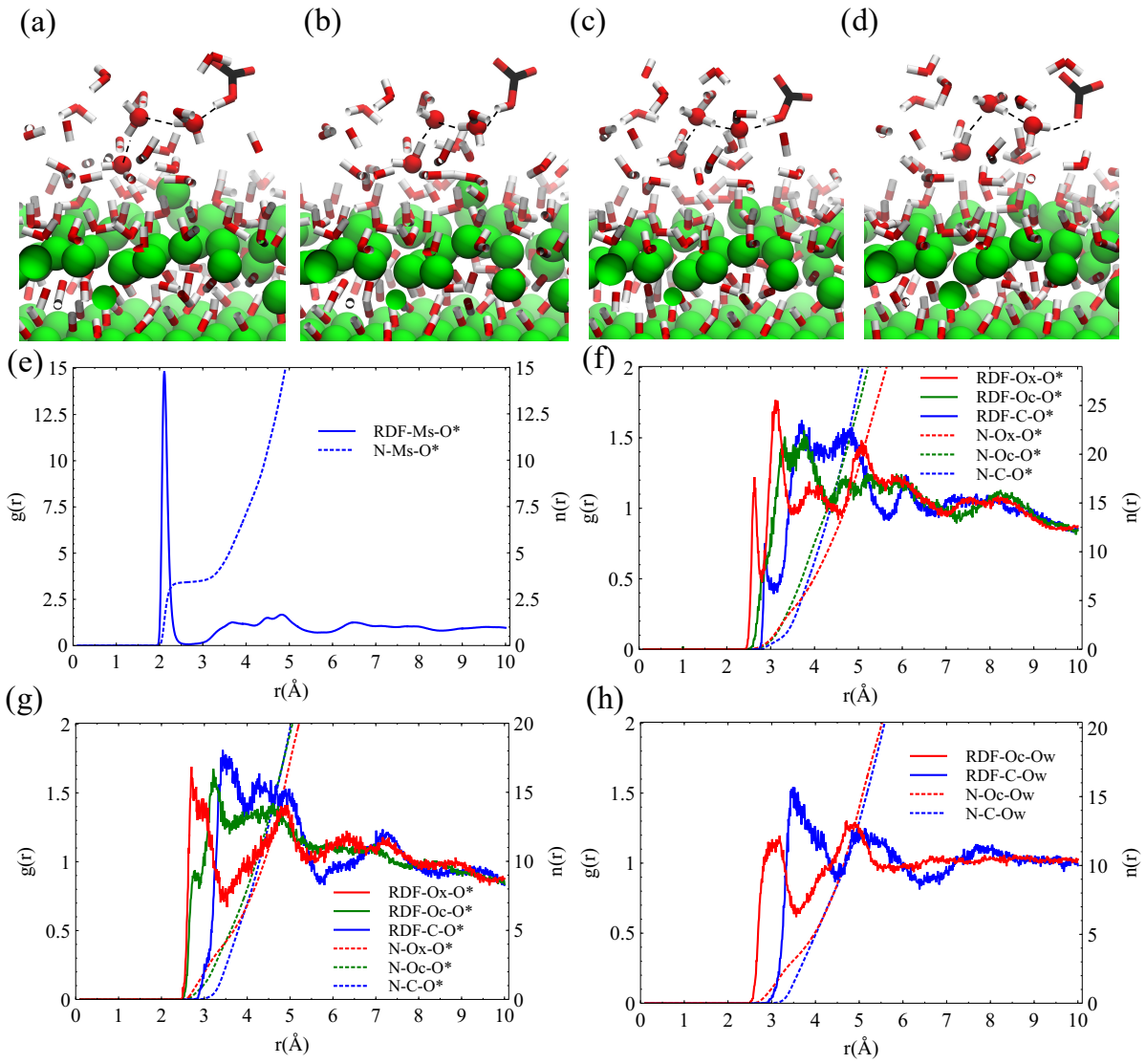

Figure 3.8. The deprotonation of bicarbonate at the brucite-water interface. From (a) to (c) the hydroxide in the first water layer diffuses toward the bicarbonate. (d) The bicarbonate deprotonates to carbonate hydrating a neighboring hydroxyl group. (e) g(r) and coordination number, n(r), for magnesium-water on the surface of brucite. (f) g(r) and n(r) for carbonic acid on the surface of brucite. (g) g(r) and n(r) for bicarbonate on the surface of brucite. (h) g(r) and n(r) for carbonate on the surface of brucite. g(r) is shown with solid line and n(r) is shown with dashed lines in all figures. O*, Ox and Oc refer to water/surface hydroxide oxygen, hydroxyl oxygen, and carbonyl oxygen respectively. Ms represents surface magnesium.

For the case of bicarbonate in the water layers on top of brucite, we see that the first peaks for both RDFs of Ox-O* and Oc-O* shift toward smaller distances as shown in **Figure 3.8.g**. We attribute this systematic shift is the result of different water permittivity in the water layers than that of liquid water. Therefore, compared to liquid water, the negative charge of bicarbonate results in

stronger electrostatics field that strengthens hydrogen bonds with dipolar water molecules. As shown in in **Figure 3.8.h**, we could not observe any further shift for the doubly-charged carbonate, that is related to the smaller charge magnitude of carbonate (~1.05) than its formal charge of 2.

The ReaxFF simulations also provide a detailed picture of the dynamics of structural hydroxide diffusion on the brucite surface. Since the adsorbed water layers on the brucite surface are more structured than liquid water, and also because the positively-charged magnesium cations attract hydroxide ions, we expect a hindered interfacial diffusion for hydroxide ions. To show this quantitatively, we run further simulations to calculate the diffusion constant of hydroxide ions adsorbed on the surface of brucite. To this end, we calculate the diffusion constant of OH^- in XY direction, parallel to the brucite surface, and in the Z direction s perpendicular to the surface using the Einstein relation:

$$D_{xy} = \frac{1}{4t}\langle \left| r_{xy}(t) - r_{xy} \right|^2 \rangle \tag{11}$$

$$D_z = \frac{1}{t}\langle |r_z(t) - r_z|^2 \rangle \tag{12}$$

In which r represents the position of the particle, and t is the time. $\langle \left| r_{xy}(t) - r_{xy} \right|^2 \rangle$ and $\langle |r_z(t) - r_z|^2 \rangle$ are the mean-square displacement (MSD) in the XY plane and in the Z direction, respectively.

To calculate the MSD for hydroxide ions on the surface, we randomly pick seven hydroxides and track the trajectory of the O^* of the OH^-.[230] The index O^* can change during the course of the simulation as proton transfer can happen between water molecules and the OH^-. We construct a similar system as in section 4-2, containing brucite slab in contact with water while letting the first two layers of brucite move and fix the inner layers. We initially relax the system in the NVT

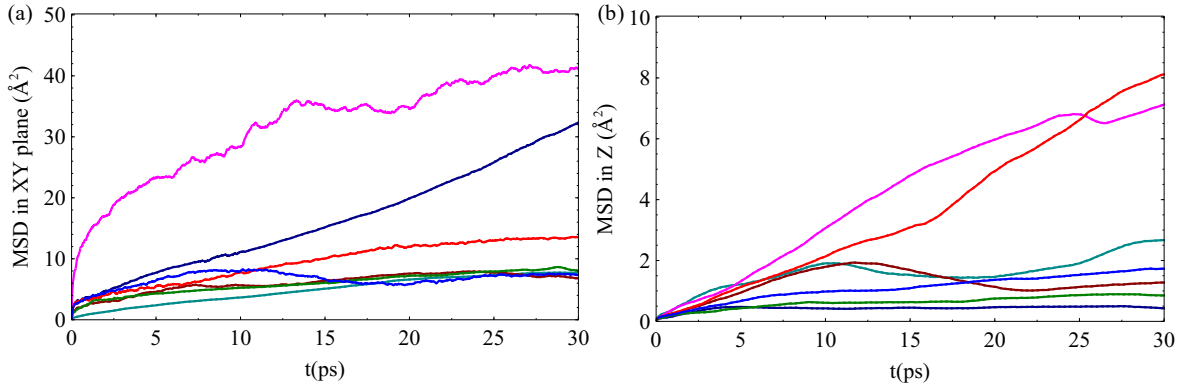

Figure 3.9. Mean-square displacement (MSD) for hydroxide ions on the surface of brucite. (a) MSD in the XY plane parallel to the surface. (b) MSD in the Z direction perpendicular to the surface. Different colors represent the displacement of seven randomly picked hydroxide ions on the surface of brucite.

ensemble at room temperature for 200 ps using timesteps of 0.25 fs and a Nose-Hoover thermostat with relaxation time of 25 fs. After the system is relaxed, we change the ensemble to NVE to avoid thermostat effects that can interfere with the trajectory of atoms. We run the system for 125 ps, and output trajectories every 2.5 fs to be used for the calculation of MSD. The resulting MSD up to 30 ps for the seven randomly picked hydroxide ions are shown in **Fig. 3.9.a-b**.

We note that the slope of the MSDs are not quite linear compared to the MSDs of hydroxide ions in liquid water resulted from the same forcefield[230]. This is due to the presence of magnesium cations on the surface of brucite that can trap the hydroxide ions. Here, we use the linear part of the MSDs with maximum slope for the calculation of diffusion constants. We calculate the diffusion constant for each O^* from the linear parts of the resulted MSDs. For the diffusion in XY plane, D_{xy} ranges between 0.04 and 0.18 Å^2/ps, while D_z ranges between 0.16 and 0.76 Å^2/ps. Based on the similar ReaxFF forcefield for water, the reported diffusion constant for the hydroxide ion in water is 1.03 Å^2/ps which is higher than our calculated diffusion constants. This difference can arise from the more structured water layers on the hydrophilic surface of brucite. The difference between D_{xy} and D_z and the variable diffusion constant derived for each of the randomly selected hydroxide ions show anisotropy and heterogeneity in the interfacial diffusion process of

these species in the adsorbed water layers. It is noteworthy that a second-generation ReaxFF water model can better predict the diffusion of hydroxide and hydronium ions compared to the one we used in our paper[230]. However, because the first generation ReaxFF water model is fitted and tested for the proton transfer between water and carbonic acid, which is essential for modelling magnesium carbonate systems, we use the first generation ReaxFF water model. Nevertheless, we carefully analyzed the proton transfer between bicarbonate and forsterite surface using both first- and second-generation ReaxFF water model. We find that the free energy barrier for the long-range proton transfer that transforms bicarbonate to carbonate is not significantly affected by the water model.

3.4.3 Free energy calculation of Mg-CO_3 surface complex formation on the surface of forsterite**:** The knowledge of the thermodynamics of ion-pairing at the solid-liquid interface is critical for understanding heterogeneous nucleation and growth. However, ion-pairing in the solution and at the solid-liquid interface is experimentally challenging to probe due to the small size of the ions and their short lifetime. On the other hand, quantum mechanical calculations are also problematic due to their high computational cost and the uncertainty about van der Waals interactions in the liquid phase. Nonetheless, molecular simulations can provide insight into the kinetics of ion interactions if accurate FFs are available. A thermodynamically stable FF was successfully able to calculate the free energy barrier for the pairing of (Ca^{2+}, Mg^{2+}, Sr^{2+}) cations and bicarbonate and carbonate species in the solution. However, metal cations on the surface of metal-silicates and metal-oxides are sometimes coordinated with hydroxide ions. Therefore, surface complex formation with ions like carbonate and bicarbonate may require a proton transfer reaction from the first shell of metal cations to their second shell, especially for magnesium cations tightly bound to

their water/hydroxide shell. This calls for a reactive FF like ReaxFF, which can model the structural diffusion of proton/hydroxide.

Here, we do the free energy calculation for the carbonate adsorption on the (010) hydroxylated surface of forsterite. First, we construct a slab of forsterite with 9 layers and an interlayer space with a size of 27 Å. We fill the interlayer space with water such that the density at the middle 10 Å is 0.91 g/cm^3 consistent with the density of liquid water when relaxed with ReaxFF. We fix the forsterite slab except for the first two surface layers at the top and the bottom. The energetics of the adsorption of carbonate on the forsterite surface is determined via the umbrella sampling (US) technique as implemented in the "PLUMED 2.5" add-on package to LAMMPS[98]. Here, we use a biased harmonic spring with a stiffness of 140 kcal/molÅ^{-2} between the center of mass of the carbonate and a fixed reference Me^{2+} atom in the inner layer of forsterite respectively. The normal distance to the solid surface is taken as the "collective variable" and sampling windows are separated by 0.1 Å. Histograms of the distribution of the collective variables were produced after 100 ps of equilibration phase, and another 250ps of the production phase of MD runs at 300 K in the NVT ensemble. The substrate (except the first two layers) were fixed. A weak harmonic potential was also considered in the 'xy' plane (parallel to the surface) to keep the carbonate in the desired adsorption site, enclosed in a cylinder. The free energy difference is then obtained via the weighted histogram analysis method (WHAM)[100].

Our PMF calculations show that the formation of $Mg \equiv CO_3$ surface complex on a random Mg site is relatively stable. This surface complex formation is made possible through a proton transfer step in which the OH^- attached to the surface grabs a proton from the second water shell. Another water molecule leaves the first shell to make room for the carbonate (see **Fig. 3.10. a-c**).The energy

barrier for this Mg-CO_3 surface complex formation is 0.21 eV, about 0.04 eV lower than the free energy required for their pairing in bulk water[160]. This has major implications on the nucleation stage. It reduces the magnesium dissolution energy barrier and can enhance the growth of magnesite crystal since ion pairs could readily attach to the crystal. This can also explain the anomalous low activation energy barrier for the nucleation and growth of magnesite at low temperature[153] when reactions occur at the thin water film formed on forsterite.

We calculate the RDF for surface magnesium and carbonate at two windows that we used for the free energy calculation: 1) When the carbonate is 5Å away from the surface. 3) When the carbonate is adsorbed on the surface and is paired with two surface magnesium atoms. The first peak of RDF for the surface magnesium (Ms) and water is located at 2.15Å similar to the location of the water in the first hydration shell of magnesium solvated in water as shown in **Fig. 3.10. d**. The water coordination number for Ms is 2.85. We label the surface magnesium that is coordinated with carbonate as Mx as shown in **Fig. 3.10. d.** Although, the location of the first peak for Mx-O* is the same as Ms-O*, the water coordination number for Mx is dropped to 2. As stated in the previous paragraph, we observe that for the magnesium-carbonate surface complex formation, the coordinated hydroxide grabs a proton from a nearby water molecule, and one water molecule is removed from the first coordination shell of Mx. When the carbonate is adsorbed on the surface, we need to differentiate two carbonate oxygens that are paired to surface magnesiums (Ox) with the one that is oriented toward the solution (Oc). As shown in **Fig. 3.10. e**, the hydration number for Oc is ~4.3, which is higher than the hydration number for oxygens of the carbonate in the solution, due to the higher density of layered water on top of forsterite. When the carbonate is distanced 5Å from the surface, we observe two peaks in the RDF for Oc-O* as shown in **Fig. 3.10.**

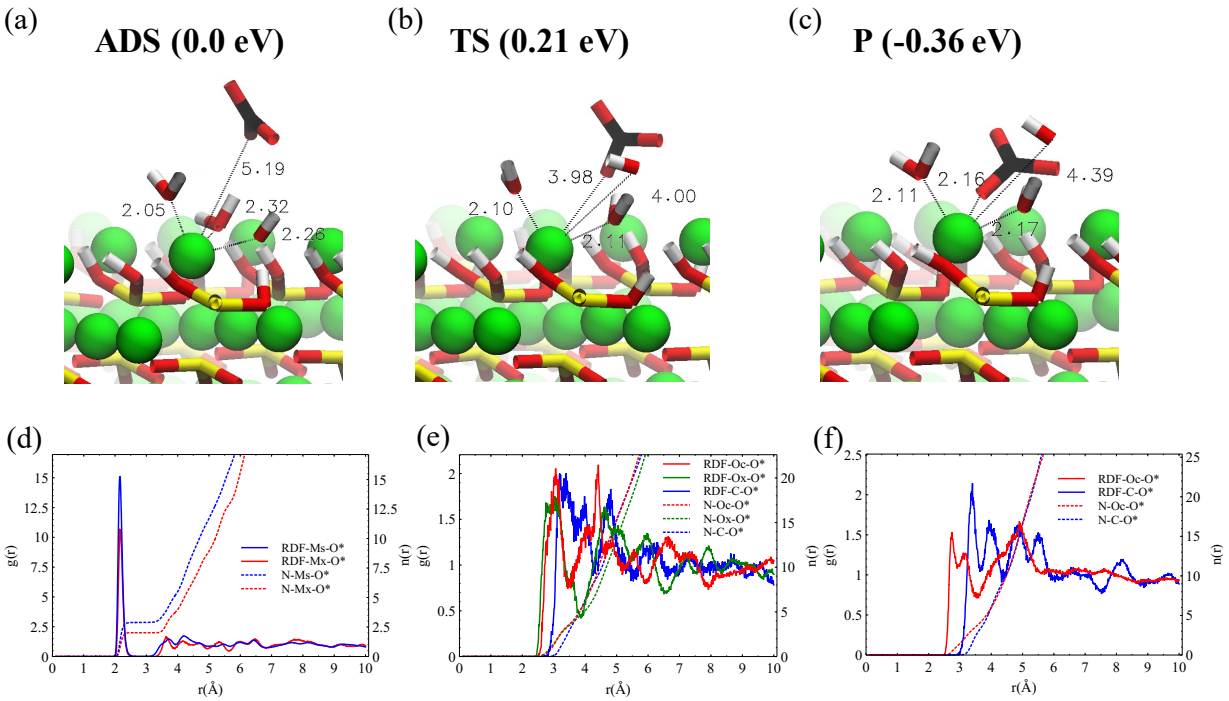

Figure 3.10. Adsorption of CO32- on hydroxylated {010} surface of Forsterite. (a-c) (ADS) adsorbate state of CO_3^{2-} as determined by PMF calculations. Two water molecules as well as one hydroxide are coordinated around surface Magnesium. (TS) transition state. (P) product state. (d) g(r) and coordination number, n(r), for (d) Magnesium (e) Bicarbonate and (f) Carbonate on the surface forsterite. g(r) is shown with solid line and n(r) is shown with dashed lines in all figures.

f. By visual inspection, we find that the carbonate is not able to rotate freely as in the solution, due to the electrostatic field it senses from the surface magnesium. Rather, one carbonate oxygen remains oriented toward to the surface for the entire time of the simulation. The hydration number of the carbonate oxygen (Oc) is 4.3, higher than its solution counterpart.

3.4 Conclusion:

We develop two reactive FFs for modeling aqueous magnesium carbonate and Mg/O/Si/C/H containing solids and their interfaces with water. We successfully parameterize the FFs to the configurations and mechanical properties of magnesite, magnesium hydroxide, magnesium oxide, and other relevant crystals. Additionally, the structures and hydration energies of magnesium are included in the list of observables for the aqueous FF. After deriving the FF parameters, we test the transferability of the interfacial FF to other prevalent magnesium-containing minerals in the

context of carbon sequestration, including the bulk structure of forsterite, nesquehonite, dolomite, and diopside. Not only the lattice properties of these crystals are captured well with our FF, but also the bulk modulus of dolomite and some of its elastic constants are predicted accurately.

Next, the interfacial structure of magnesium (-carbonate, -silicate, and -oxide) minerals when dry or in contact with a single water molecule are investigated using both DFT calculations and interfacial ReaxFF. Although the geometry of all dry surfaces is similar in both methods, the hydration energies are overestimated when calculated through the reactive FF. Some hydrogen bonds are underestimated, except for the case of "side water" adsorption on the surface of forsterite. The discrepancy of hydration energies and hydrogen bond distances stems partly from the oxygen-hydrogen interaction parameters in ReaxFF that are mainly fitted to describe liquid water, and partly from the absence of Mg-O-O and Mg-O-H parameters in our forcefield. Unlike the single water molecule adsorption, the adsorption energies resulted from ReaxFF for two to five water monolayers are in agreement with the experiment. This makes our FF suitable to study reactions at the water-forsterite interface when few water monolayers are present.

Then, we study the interaction of magnesium and (bi)carbonate in gaseous clusters and liquid water. Our calculations for magnesium-(bi)carbonate ion-pairing through the fitted aqueous FF agree well with DFT results. Although the obtained energies for SSIP structures are lower than the CIP structure in gaseous clusters, the averaged potential energies in liquid water confirm the relative stability of CIP to SSIP and SSIP to SI structures. This enables our force field to study homogeneous nucleation of magnesite, hydromagnesite, nesquehonite, and amorphous magnesium carbonate phases. We also check the applicability of the derived reactive forcefields for the dissociation of carbonic acid in liquid water that contains magnesium and hydroxide ions

and the interfacial water layers on top of the brucite surface. Our simulations demonstrate the migration of hydroxide ions that leads to carbonate production, whether in liquid water or at the interface of brucite. Proton transfer reactions at the interface of metal oxides have been previously observed through both experiments and quantum mechanical calculations.

The observed proton transfer at the hydroxylated-solid-water interface has significant implications on the nucleation of magnesium carbonate phases at geological conditions. It can explain the anomalously low activation energy barrier for the formation of magnesite. At the molecular scale, it can manifest both through the pairing of the dissolved surface magnesium and carbonate at the thin water film or the formation of neutral magnesium-carbonate surface complexes that can dissolve faster than the magnesium cation[35]. Here, we show that a stable Mg-CO_3 surface complex can form on the hydroxylated surface of forsterite with a low energy barrier. However, more elaborate free energy calculations that consist of magnesium-water coordination number as a collective variable are needed for more accurate energy barrier calculations.

Chapter 4

Formation and Dissolution of Surface Metal Carbonate Complexes: Implications for Interfacial Carbon Mineralization in Metal Silicates

4.1 Introduction:

Permanent CO_2 storage in the form of metal carbonates is a promising route to constrain the untethered carbon emissions from the transportation, civil and energy infrastructure. Such storage technologies can be realized either *in situ* through the geological carbon sequestration in mafic (*e.g.,* basalts) and ultramafic (*e.g.,* peridotite) lithologies[147] or *ex situ* by carbonating industrial and construction waste to produce value-added commodities. Cementitious materials, for instance, can potentially offset 43% of their production carbon footprint through the ambient carbonation process.[66] Whether realized *in* or *ex situ*, the storage security and economic cost associated with these carbon sequestration solutions can be only lowered if the design process ensures enhanced carbonation kinetics with rapid and close-to-complete CO_2 conversion.

When considering carbonation reaction, the composition of processing (injection) fluid, chiefly H_2O-to-CO_2 ratio, plays a critical role in tuning mineralization kinetics and reaction pathways. This is particularly significant considering the low mutual solubility of water and CO_2. Unlike reactions mediated by water-rich fluids, the carbonation reactions with humidified CO_2-rich fluids might appear hindered owing to uncertainties arising in mass transport processes and ion solvation extents.[231] However, well-controlled CO_2-rich laboratory and field-scale experiments on

olivine[16,33–35,37,38,79,83,84,231,232], brucite[82], and feldspar[32] show that the carbonation in such environments can be potentially facile due in parts to the formation of nanometer-thick adsorbed water films.

Adsorbed water nanofilms present a unique nanoscale environment whose physicochemical properties (*e.g.,* dielectric permittivity, hydrogen bond network, self-diffusivity, etc.) as a reactant and solvent are distinct from their bulk counterparts. For instance, recent experiments provide an evidence for the enhanced CO_2 speciation when carbonating forsterite with adsorbed water nanofilms[29,35]. Leveraging oxygen scrambling technique, Miller et al.[35,232] have shown that carbonic acid forms much faster on nanoparticles of forsterite compared to fumed silica. The adsorbed water nanofilms, also, confine the resultant carbonic acid and (bi)carbonate adjacent to the surface. This could potentially rise to distinct interfacial carbonation pathways that initially favor amorphous phases in low water-coverage regimes.[82,84] In such pathways, the formation of surface metal (bi)carbonate complexes[36] is demonstrated by the high-pressure titration experiments coupled with *in situ* infrared (IR) spectrometry[81] and ^{1}H-^{13}C cross-polarized Nuclear Magnetic Resonance spectroscopy[35].

Despite the extensive body of experimental and simulation literature on aqueous CO_2 reactivity[140,143,215,216,233–237], the chemical reactions at the nano-meter scale mineral-water interfaces remain largely unknown. In particular, the underlying molecular mechanisms driving the formation of magnesium-(bi)carbonate surface complexes and metal ion dissolution are still unclear. Such fundamental reaction steps are critical in advancing our understanding of nanoconfined carbon mineralization in adsorbed water films and motivate the two-fold objective of the present paper. The first objective is to delineate the mechanistic picture of the formation of

metal carbonate surface complexes in interfacial water films. The second objective is to clarify the role of interfacial carbonate anions in tuning the dissolution kinetics, *i.e.,* ligand-enhanced dissolution. The experiments remain ambivalent when it comes to quantifying the impact of (bi)carbonate concentration on the dissolution kinetics in H_2O-rich media.[238–240] However, magnesium carbonate precipitation rates increase with increasing temperature and CO_2 pressure during the forsterite carbonation in thin water films.[24] Such observations suggest that the dissolution rate might increase with (bi)carbonate concentration in water films.

Herein, we use reactive and nonreactive molecular simulations to address our two objectives. We probe the fate and role of (bi)carbonate on 1) forsterite (Mg_2SiO_4), the magnesium endmember of olivine, relevant to carbonation studies of mafic (e.g. basalt) rocks, and 2) Calcium-Silicate-Hydrate (C-S-H), the most critical phase in the modern concrete.[63–65] Concrete Carbonation (ambient and valorized demolition waste) can sink up to 2.5% of the man-made carbon emissions, despite excessive carbon emissions caused by the cement production.[66–68] Besides their technological significance and relevance to carbon sequestration, the comparative study of forsterite and C-S-H allows us to probe the intricate role of cation (Ca^{2+} and Mg^{2+}) hydration dynamics and water exchange rates on the elementary interfacial carbonation steps.[74]

4.2 Methods:

4.2.1 Reactive Molecular Dynamics Simulations

Reactive simulations are performed using ReaxFF[241], a semi-classical potential which features bond-order formalism to model the formation and breakage of bonds, and utilizes the

electronegativity equalization method (EEM) to equilibrate charge fluctuations and transfer. In general, the total potential energy in ReaxFF could be written as:

$$E_{tot} = E_{bond} + E_{VDW} + E_{qeq} + E_{penalty} + E_{over} \quad (1)$$

where E_{bond}, E_{VDW}, E_{qeq}, $E_{penalty}$, and E_{over} are respectively bonded, van der Waals, electrostatic, penalty and over-coordination terms. For carbonation of calcium silicates, we adopt the potential parameters from a work on aqueous calcium carbonate systems[161] where the calcium charge is fixed. This parameter set has been tested in a number of studies, including in an investigation on the calcite-water interface[242] and the prenucleation of calcium carbonate in solutions[243]. Similarly, for interfacial and aqueous carbonation of magnesium-containing systems, we developed a ReaxFF parameter set with fixed magnesium charge.[244] This parameterization faithfully reproduces first principle and experimental hydration structure, hydration energy, a wide range of crystal structures, adsorption energy and proton transfer in cluster and interfacial systems. The interested readers are referred to the Zare and Qomi[244] for details. We implemented an in-house module in LAMMPS[95] to take into account the fixed charge in the charge equalization scheme. Reactive simulations are performed in the NVT ensemble at 300K. The simulation time step is set to 0.25 fs, with the Nose-Hoover thermostat with a relaxation time of 100 fs.

4.2.2 Non-reactive Potential-of-Mean-Force (PMF) Calculations

The energetics of the dissociation of metal from the solid surface is determined via the umbrella sampling (US) technique as implemented in the "PLUMED 2.5" add-on package to LAMMPS[98]. Here, we use a biased harmonic spring with a stiffness of 200 kcal/molÅ^{-2} and 120 kcal/molÅ^{-2} between Me^{2+} cation and a reference Me^{2+} atom on the surface respectively. The normal distance to the solid surface is taken as the "collective variable" and sampling windows are separated by

0.1 Å. CSH-FF[99] and a modified version of Clay-FF [77] was also used for the dissolution of Me^{2+} ions from the surface, although for the case of carbonate-assisted dissolution, it was combined with a forcefield developed for carbonate minerals and solvated carbonate ions.[160] An additional collective variable namely the surface Mg water coordination number is also considered, see the **Supplementary Note 2** for more details. The harmonic spring with stiffness of 2000 kcal/mol is chosen for the coordination number. Histograms of the distribution of the collective variables were produced after 500 ps of equilibration phase, and another 1 ns of the production phase of MD runs at 300 K in the NVT ensemble. The substrate (except the first two layers) were fixed. A weak harmonic potential was also considered in the 'xy' plane (parallel to the surface) to keep the ion in the desired adsorption/desorption site, enclosed in a cylinder with the fixed reference atoms on its base. The free energy difference is then obtained via the weighted histogram analysis method (WHAM)[100].

4.2.3 Proton Transfer Potential-of-Mean-Force (PMF) Calculations

To calculate the free energy of the long-range proton transfer reactions, we first defined the coordinate of the excess proton (or hydroxide)[228,245]:

$$\vec{\xi} = \sum_{i=1}^{N_H} \mathbf{r}^{H_i} - \sum_{j=1}^{N_X} w^{X^j} \mathbf{r}^{X^j} - \sum_{i=1}^{N_H} \sum_{j=1}^{N_X} f_{sw}(d_{X_j,H_i})(\mathbf{r}^{H_i} - \mathbf{r}^{X^j}) \quad (2)$$

where $\mathbf{r}^{atom}$ is the position of hydrogen (H) or heavy atoms (X), w^{X^j} is the number of hydrogens bonded to the heavy atom in its least protonated state. In our case, w^O for the oxygen in bicarbonate is zero while it is 1 for the oxygen of hydroxide. The switching function $f_{sw}(d)$ is a continuous function that determines if the hydrogen is bonded to the heavy atom or not:

$$f_{sw}(d) = 1/(1 + \exp\,[(d - r_{sw})/d_{sw}]) \quad (3)$$

where d is the distance between the heavy atom and hydrogen atoms. r_{sw} and d_{sw} are fixed parameters that are chosen to be 1.4Å and 0.05Å in our work. These values are observed to give us the best results in terms of the stability of the hydrogen atoms around oxygens. The general coordinate $\vec{\xi}$ gives us the location of excess charge in the set of atoms involved in the proton transfer, and could be used to define a one-dimensional reaction coordinate,

$$\zeta_R = \frac{\left|\mathbf{r}^D - \vec{\xi}\right|}{\left|\mathbf{r}^D - \vec{\xi}\right| + \left|\mathbf{r}^A - \vec{\xi}\right|} \tag{4}$$

in which $\mathbf{r}^D$ is the position of the initial donor (i.e. the oxygen in bicarbonate in our work), and $\mathbf{r}^A$ represents the position of the final acceptor (i.e. the oxygen in hydroxide in our work). ζ_R is indeed a fractional reaction coordinate. Umbrella sampling calculations are done for 41 windows equally spaced from 0 to 1 using the "PLUMED 2.5" add-on package to LAMMPS[98]. Spring constants vary from 7000 to 30000 kcal/(mol.Å^2). The free energy difference is then obtained via the weighted histogram analysis method (WHAM)[100].

4.3 Results and discussion:

4.3.1 Reactive simulations of bicarbonate with metal silicate surfaces

To understand carbonation reactions in adsorbed water nanofilms at the molecular level, we should address how the bicarbonate and carbonic acid interact with the surface. In fact, experiment[29,35] and simulations[143,233] show that bicarbonate and carbonic acid are present on the surface of silica fume and forsterite nanoparticles and in large water clusters. Here, we perform reactive molecular dynamics (MD) simulations to study the interaction of carbonic acid and bicarbonate within the saturated slit pore of C-S-H and hydroxylated {010} forsterite surface. As the analogue of C-S-H,

we employ a defective Hamid tobermorite ($Ca_{2.25}[Si_3O_{7.5}(OH)_{1.5}].1H_2O$)) {001} at 1.7 Ca/Si ratio[63]. For reactive MD simulation details see the **Methods** section.

First, we place a bicarbonate ion in the adsorbed water layers on the surface of metal-silicate, fixed at a distance of about 8 Å away from the surface. While fixing the oxygen-hydrogen bond in the bicarbonate to avoid any reaction, we equilibrate the system for few picoseconds. At this stage, we observe spontaneous diffusion of surface OH^- groups in the adsorbed water layer adjacent to the surface. Similar proton hopping events are observed through AIMD simulations of water on ZnO surface[221], scanning tunneling microscopy experiments on FeO[223] and TiO_2[224] monolayers, and single-molecule localization microscopy on defective boron nitride layers[225].

After releasing the constraint on the bond, we observe that bicarbonate dissociates to carbonate only after tens of picoseconds. The resultant carbonate subsequently adsorbs onto the surface and combines with a metal cation forming a surface $MeCO_3$ complex, in agreement with the observed surface complexes by Loring et al.[36] using *in situ* FTIR and Miller et al.[35] via ^1H-^{13}C cross-polarized NMR spectroscopy. Such complexes are also found on metal oxides[246,247] and hydroxylated metal oxide nanoparticle[248] surfaces, showing bicarbonate deprotonates in the presence of adsorbed water films. We also observe a similar mechanism in the presence of interfacial carbonic acid in reactive MD simulations.

Upon our visual observation, the hydroxyl in bicarbonate, which is fixed almost at the third water monolayer, forms a long chain of hydrogen bonds through intermediate water molecules and is anchored at the other end to a surface hydroxide, see **Fig. 4.1**. The formation of this structure is immediately followed by a long-range proton transfer mechanism, pushing the hydroxyl group

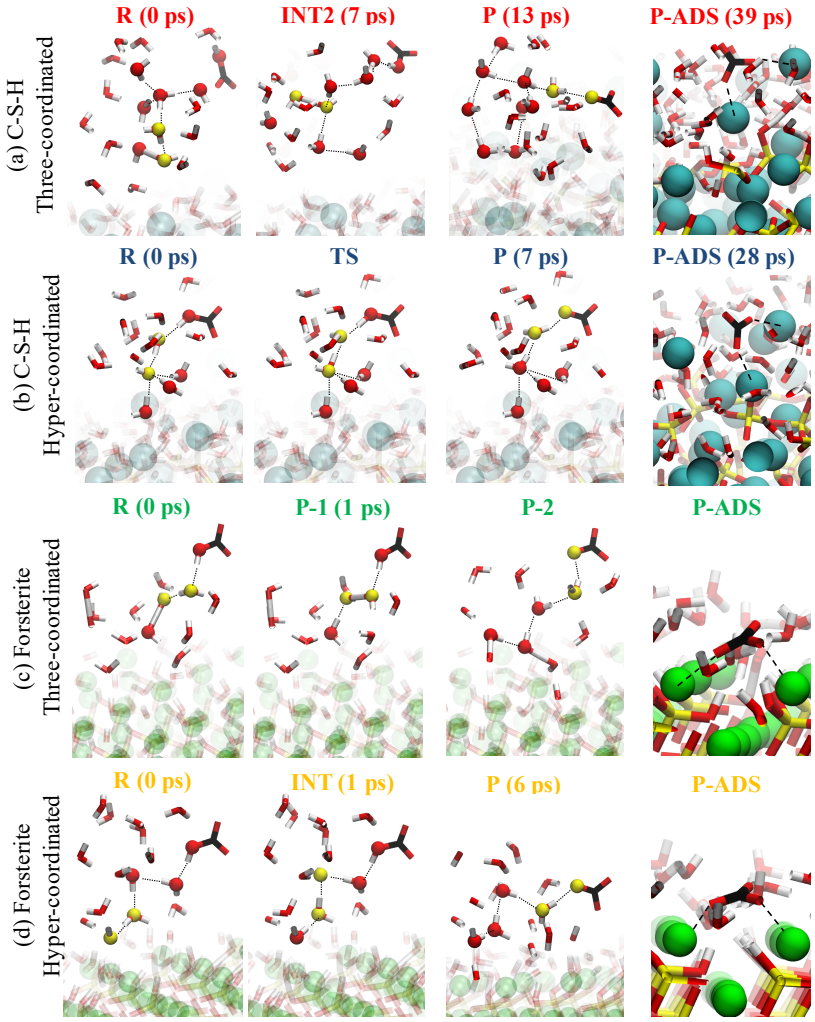

Figure 4.1. The proton transfer reaction path between surfaces and the bicarbonate, followed by the adsorption of carbonate anion on the surface. (a) Sample snapshots from C-S-H simulations using three-coordinated hydroxide force field: Initially, bicarbonate (HCO_3^-) is present close to the C-S-H surface. A chain of water molecules is formed from a hydroxide (acceptor) on the C-S-H surface on one end, to the bicarbonate ion (donor) on the other end. The second intermediate state (INT2) shows a Zundel-like group ($H_3O_2^-$) as a result of proton movement from the C-S-H surface up to the bicarbonate group. The final proton movement (P) results in the exothermic formation of CO_3^{2-}. Finally, the carbonate group was adsorbed to the surface with no energy barrier, where it is coordinated with two calcium atoms. (b) Sample snapshots from C-S-H simulations using hyper-coordinated hydroxide force field: The initial state of the reaction shows that an OH^- close to the surface is hyper-coordinated with 4 water molecules. The transition state (TS) depicts the instability of ($H_3O_2^-$) in the hypercoordination formulation. The final proton movement (P) leads to the exothermic formation of CO_3^{2-}. Snapshots of forsterite carbonation through proton transfer mechanism using (c) three-coordinated (d) hyper-coordinated hydroxide force fields. Calcium, oxygen, hydrogen, carbon, and magnesium atoms are shown in cyan, red, white, black, and green, respectively. The atoms shown in yellow are oxygen atoms involved in proton transfer in that frame.

from the surface to the bicarbonate through structural diffusion[249], and finally transforming the bicarbonate to a carbonate anion. Structural diffusion, often called “Grotthuss diffusion”, is the hopping of a proton from a hydronium ion to a neighboring water molecule, or from a water

molecule to a neighboring hydroxide. It involves breakage and formation of O-H bonds as the proton migrates between water molecules and it is much faster than vehicular diffusion, in which the centers of charge and mass move together.[227] It is important to note that the version of ReaxFF[161] we use in this simulation is shown to give satisfactory energy change for the deprotonation of carbonic acid to bicarbonate compared to quantum mechanical results when two water molecules are in the solvation shell.

It is noteworthy that it was long believed that the structural diffusion of a hydroxide is only a mirror image of the structural diffusion of a hydronium ion in water.[250] However, Car-Parrinello Molecular dynamics (CPMD) simulations[251,252] provide a new picture of hydroxide water coordination, called "hyper-coordination" that enables the hydroxide to accept four hydrogen bonds, and possibly donate a weak hydrogen bond, in contrast to the traditional view in which it only accepts three hydrogen bonds. Consistent with core-level spectroscopy experiments, neutron diffraction and neutron scattering data, this could play a major role for the lower diffusion rate of hydroxide than that of hydronium in a condensed water phase.[252]

Even with high level functionals such as PBE0, the "three-coordinated" hydroxide is still observed in population analysis.[252] Furthermore, the structured water nanofilms could change the proton transfer mechanism and hydroxide solvation structure, as shown through AIMD simulations of anion-exchange membranes[253]. These observations motivate us to separately simulate the proton transfer reaction between the bicarbonate and the surface of C-S-H and forsterite using both "three-coordinated"[254] and "hyper-coordinated"[230] ReaxFF water models, as shown in **Fig. 4.2.** We

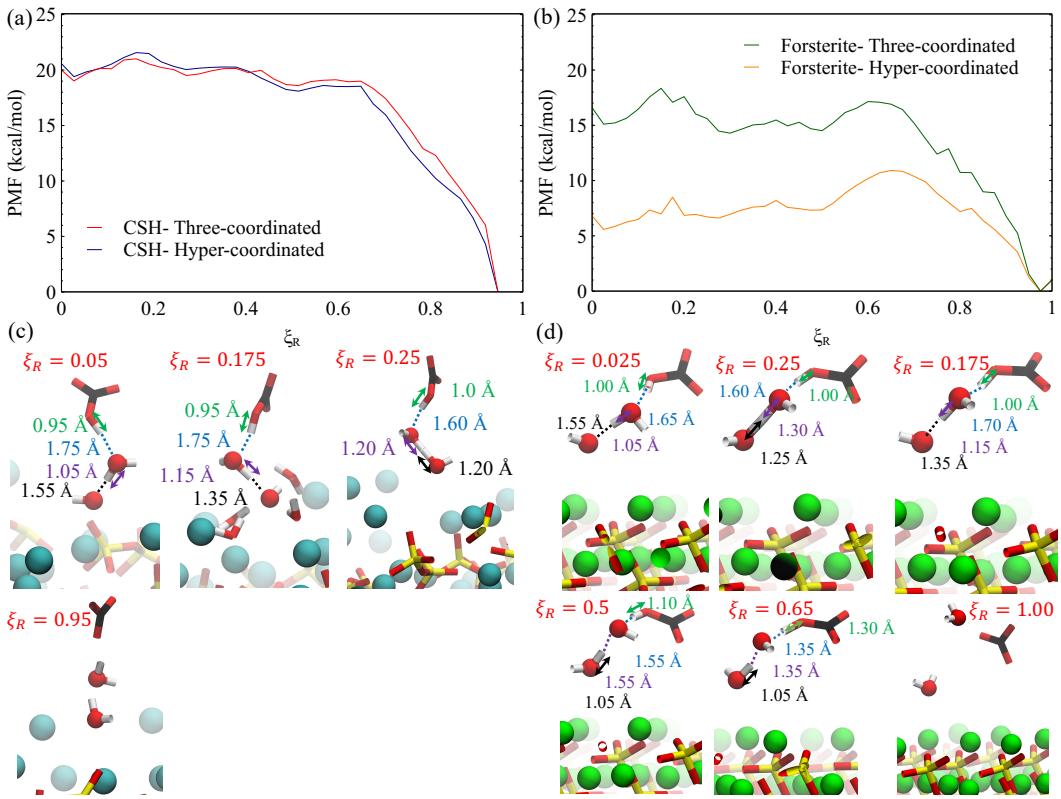

Figure 4.2. Potential-of-Mean-Force (PMF) for the proton transfer reactions. (a) PMF for the reaction of bicarbonate with the surface of C-S-H using two descriptions of water molecule coordination states. (b) PMF for the reaction of bicarbonate with the surface of forsterite using two descriptions of water molecule coordination states. (c) Snapshots from PMF calculations on the surface of C-S-H. (d) Snapshots from PMF calculations on the surface of forsterite. The surrounding water molecules are not shown for clarity.

confirm that regardless of the employed water model, the hydroxide ion structurally diffuses from the surface toward the bicarbonate in the interfacial water film.

We calculate the free energy landscape of the long-range proton transfer between C-S-H and forsterite surfaces and bicarbonate based on the collective variable, ξ_R, which locates the position of the excess charge or (OH^-)[228]. By way of example, when ξ_R is 0.0, 0.5, or 1.0, the excess charge's center is located at the donor, in the middle, or at the acceptor in proton transfer step, see the **Methods** section for more details. We position the bicarbonate at the interface of C-S-H and forsterite such that only one intermediate water molecule bridges between the bicarbonate and surface hydroxide. The interface is full of water molecules layered upon the surface as expected for hydrophilic surfaces. By definition, the collective variable ξ_R includes the location of oxygen

and hydrogen atoms in the three molecules involved in the proton transfer reaction (the bicarbonate, the hydroxide and the intermediate water). This ensures that the fluctuation of hydrogen bonds and the rotation of the intermediate water molecule are taken into account. As shown in **Fig. 4.2.a-b**, the free energy barrier for these processes resulted from three-coordinated ReaxFF water model is 2.0 kcal/mol for C-S-H and 3.2 kcal/mol for forsterite. For hyper-coordinated water model, free energy barriers of 2.3 kcal/mol and 5.4 kcal/mol were obtained for C-S-H and forsterite, respectively. Although the general shape of the energy landscapes are somewhat similar regardless of the forcefield implemented, the barriers derived from hyper-coordinated water model are higher than those resulted from the three-coordinated water model, in parts due to the lower diffusion constants of hyper-coordinated OH^- in water compared to the three-coordinated hydroxide[230].

We also find that the long-range proton transfer reaction between the surface and the bicarbonate is stepwise, both on C-S-H and forsterite surfaces. As shown in **Fig. 4.2.a-b**, the initial barrier for the hydroxide to migrate perpendicularly from the surface to the water layer is in the range of 2-3.2 kcal/mol. Previous AIMD simulations were able to show the proton transfer either between the surface oxygen and adsorbed layer or between the hydroxide and water molecules within the adsorbed layer parallel to the surface of the oxides[221,222,255,256]. The corresponding energy barriers were found to be in a wide range of 0.5-8 kcal/mol depending on surface composition and surface site.

Our observations of structural proton transfer away from surface to the bicarbonate are due to hydrogen bond network fluctuations formed by bicarbonate within the adsorbed water layer. For instance, we observe that at the transition state ($\xi_R = 0.175$), the hydrogen bond distance between

the oxygen of the surface hydroxide and the adjacent water molecule is squeezed while the OH bond of the water molecule is elongated, see **Fig. 4.2.c-d**. The fluctuations in the hydrogen bond network in the adsorbed water layer have been previously shown through AIMD simulations to facilitate the proton transfer events on the surface of metal oxides[221,255]. As shown in the same figures**,** the ξ_R value of 0.25 is reminiscent of the Zundel-like water structure which has the same level of energy as the structure shown for the initial state $\xi_R = 0.025$ in case the three-coordinated water model is used. However, the Zundel-like water structure in the hyper-coordinated water scheme is energetically less stable than the initial structure at $\xi_R = 0.025$.

On the C-S-H surface, the hydroxide is smoothly transported to the bicarbonate after the initial transition at $\xi_R = 0.175$, see **Fig. 4.2.c-d**. However, for the case of forsterite, there is clearly a second transition state at around $\xi_R = 0.65$ due to the relatively more structured layers of water on forsterite than C-S-H, which in turn can be attributed to the higher residence time of water around magnesium when compared to calcium.

Following the completion of proton transfer, the produced carbonate combines exothermically with a metal cation on the surface. Surface metal carbonate complexes on forsterite surfaces are detected using attenuation total reflection IR spectroscopy[36] and $^{1}H–^{13}C$ Cross-Polarized NMR spectroscopy techniques[35]. Our simulations show that the surface complex formation is accompanied by the removal of one water molecule from the first hydration shell of surface metal. This is barrierless for $CaCO_3$ and has an energy barrier of roughly 5 kcal/mol for $MgCO_3$. When compared to the ion pair formation in the solution[160], this shows that the barriers associated with surface metal-carbonate complex formation are lower than 9.5 and 2.5 kcal/mol reported respectively for magnesium and calcium carbonate ion pair formation in aqueous media. The

difference between the calcium and magnesium carbonate ion pair formation energy barrier is intimately related to the extended residence time of water molecules coordinated in the first hydration shell of Mg^{2+} cations.

4.3.2 Dissolution of surface metal ion through a carbonate-promoted mechanism

It is imperative to resolve the energetics of Me^{2+} dissolution as it is generally-perceived to be the rate-limiting step in metal silicate carbonation reaction.[147] To this end, we calculate the dissolution free energy of Me^{2+} via the umbrella sampling technique, see the **Methods** section for details. Random surface calcium atoms were selected for dissolution simulations on the C-S-H surface. We find that the corresponding energy barriers are in the range of 11-20 kcal/mol, **Fig. 4.3.a**. This shows that Ca^{2+} ions can readily dissolve from C-S-H in the absence of surface protonation and carbonate ligands. The observed wide dissolution energy barrier range, in parts, originates from the heterogeneity of interfacial calcium cations, see **Fig. 4.3.b** and **Fig. 4.3.c**. *Ab initio* MD simulations reported a similar variability in the placement of calcium atoms at the interface with water for anorthite ($CaAl_2Si_2O_8$) surfaces.[257] DFT Calculations of Ca-proton exchange on hydrated wollastonite ($CaSiO_3$) {010} surface show an energy barrier of 11 kcal/mol,[258] which is close to our lower bound force field calculations.

For the case of forsterite, we consider the under-coordinated magnesium at an obtuse edge, which is found as a favorable site for dissolution according to X-ray reflectivity experiments.[259] It is also important to consider the water coordination number of Mg^{2+} ion as an additional collective variable since the water exchange rate is four orders of magnitude slower around solvated Mg^{2+} ion compared to that of Ca^{2+} ions.[260] When the surface Mg^{2+} ion is coordinated with an adsorbed

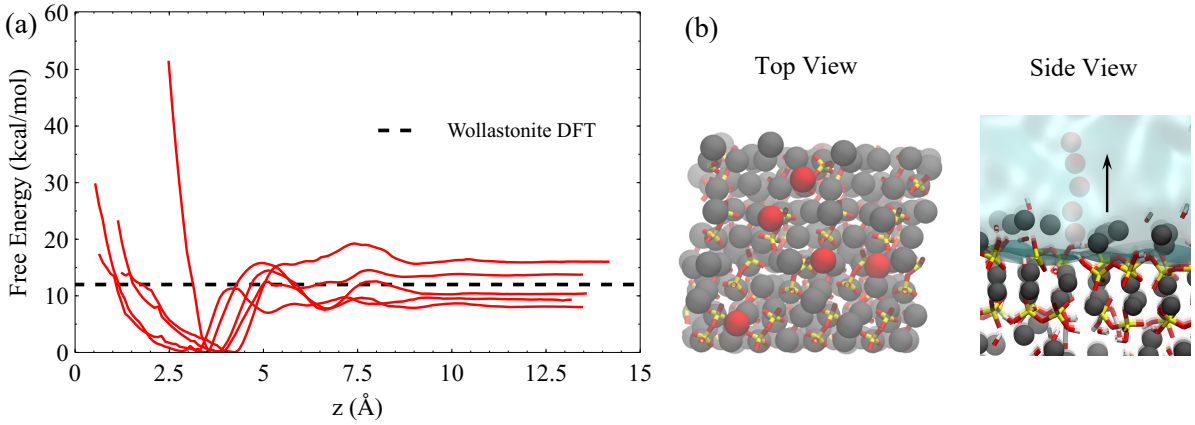

Figure 4.3. Potential-of-Mean-Force (PMF) for the dissolution of Me2+ from C-S-H and forsterite surfaces. (a) Free energy of random Ca^{2+} dissolution from the C-S-H surface, using the umbrella sampling approach. The black dashed line represents the Ca-exchange energy barrier on the wollastonite surface[70] using the DFT method. The inset demonstrates the variation of calcium atoms on the disordered surface of C-S-H. (b) Top and side view of C-S-H slab. In the top view, randomly selected calcium atoms for dissolution are shown. The side view demonstrates a schematics of calcium dissolution from the surface. Calcium atoms on the surface are located are variably distanced from the surface due to the disordered and heterogeneous structure of C-S-H.

carbonate ion, we protonate two neighboring silicate oxygens that represent detached protons from precursor interfacial carbonic acid and bicarbonate groups. Although the adsorption site of carbonate and protons on the surface might not necessarily be the same, chances of finding such configurations increase significantly in adsorbed water films within geological conditions.

The resulting 2D dissolution PMF for the carbonate-assisted dissolution is presented in **Fig. 4.4.a**. The minimum free energy path is calculated using the Nudged Elastic Band (NEB) technique. This path is shown by black lines connecting two stable states at each end. The initial stable state represents the reactant state, where two magnesium atoms on the surface are coordinated with a carbonate, as shown in **Fig. 4.4.c**. Two water molecules are found in the first shell of the dissolving magnesium at this state. At the transition state, when the dissolving magnesium is almost 1 Å away from the surface, an additional water molecule enters the first coordination shell as shown in **Fig. 4.4. d**. At this state, one carbonyl oxygen of the carbonate rotates to detach from the adjacent surface magnesium atom. Finally, we find the dissolved magnesium in a stable state when it is

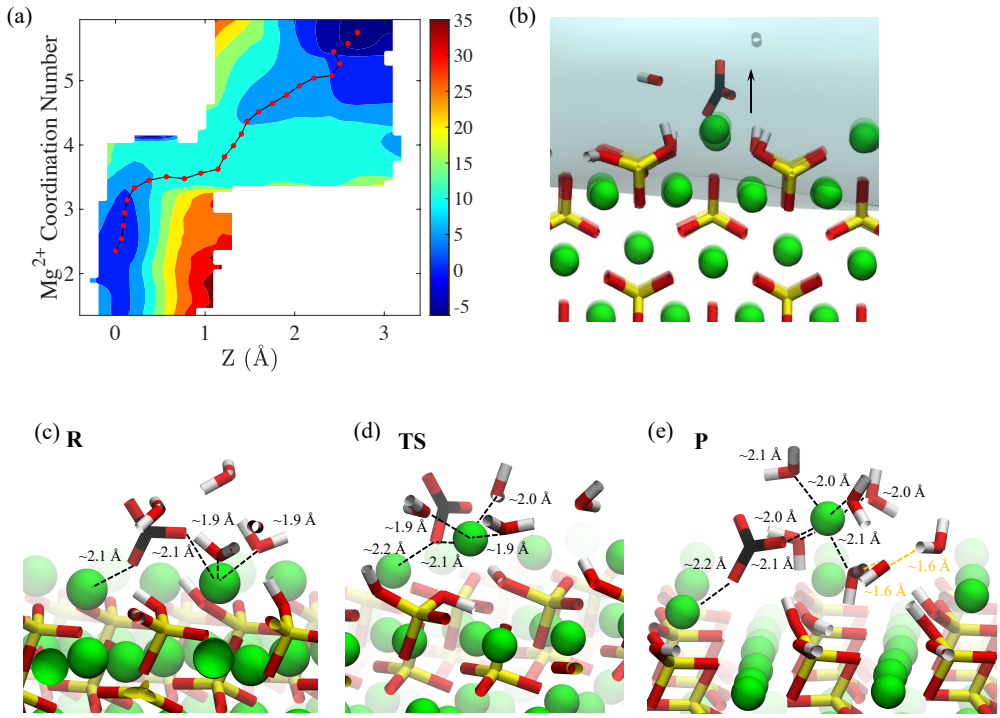

Figure 4.4. Carbonate-assisted dissolution of magnesium from a step site (a) 2D map of Potential of Mean Force (PMF) resulted from umbrella sampling. The two collective variables namely, distance from the surface (Z) and water coordination number of magnesium are shown in the x and y axis respectively. (b) Obtuse edge of (010) surface of forsterite. Carbonate is initially adsrobed on the surface. The arrow shows the direction of the magnesium dissolution from the surface. (c) Reactant state (R) involving carbonate and two water molecules coordinated to a magnesium at the step site. Carbonate is bondend to two magnesium atoms in a monondate form. (d) Transition state (TS) for the dissolution of magnesium. Three water molecules are coordinated to dissolving magnesium which has a distance of ~ 1Å from the surface. The carbonate ion is rotated such that only one carbonyl oxygen is bondded to the surface. (e) Product state (P) for the dissolution of magnesium. Magnesium is ~ 3Å away from the surface. Five water molecules are coordinated in the first shell. Black dashed lines show the bond between magnesium and water. Orange dashed lines show the hydrogen bonds. The surface is in contact with liquid water, however, only neighboring water molecules are shown in the figures for brevity.

almost 3 Å away from the surface, while coordinated by 5 water molecules and the carbonate ion as shown in **Fig. 4.4.e**. However, we observe that another water molecule is tighly bound in the second coordination shell due to the hydrogen bonds with with a hydroxyl group and a water molecule in the first coordination shell of magnesium. This gives rise to the coordination number of 5.7 at the product state. We note that Mg^{2+} water coordination number in aqueous $MgCO_3$ ion pair is shown to be ~5.2 using the same forcefield.[160]

To better understand our carbonate-assisted dissolution results, we also consider a carbonate-unassisted dissolution of Mg^{2+} from the same obtuse edge and the same surface protonation

scheme. However, to preserve charge neutrality, two additional hydroxyl groups are placed on the surface replacing the carbonate ion. The resulted 2D dissolution PMF for this case is shown in **Fig. 4.5.a**. At the reactant state, the magnesium at the step site is initially coordinated with two water molecules and one hydroxyl group, as shown in **Fig. 4.5.c**. The transition state occurs when the magnesium is almost 1 Å away from the surface similar to the carbonate-assisted case. At this state, another water molecule is found in the second shell of magnesium forming hydrogen bonds with silicate hydrogen and a water molecule in the first shell. The hydrogen bond between this water molecule and silicate hydrogen makes the bond between the dissolving magnesium and the surface silicate weaker. When the magnesium is almost 3 Å away from the surface, another stable

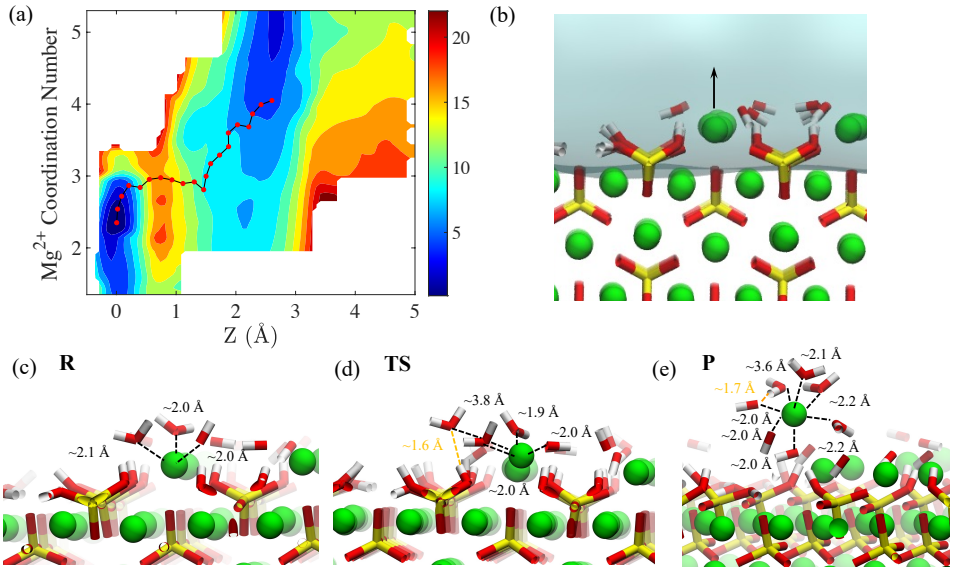

Figure 4.5. Magnesium dissolution from a step site of forsterite through the protonation of two silicate oxygens. (a) 2D map of Potential of Mean Force (PMF) resulted from umbrella sampling. The two collective variables namely, distance from the surface (Z) and water coordination number of magnesium are shown in the x and y axis respectively. (b) Obtuse edge of (010) surface of forsterite. The arrow shows the direction of the magnesium dissolution from the surface. (c) Reactant state (R) involving one hydroxyl group and two water molecules coordinated to a magnesium at the step site. (d) Transition state (TS) for the dissolution of magnesium. An additional water molecule enters the coordination shell of magnesium with a distance of 3.8 Å. It forms a hydrogen bond with the silicate hydrogen assisting the dissolution of undercoordinated magnesium which is 1 Å away from the surface. (e) Product state (P) for the dissolution of magnesium. Magnesium is ~ 2.7 Å away from the surface. Four water molecules and three hydroxyl groups are coordinated around dissolved magnesium. Black dashed lines show the bond between magnesium and water. Orange dashed lines show the hydrogen bonds.

state is found, see **Fig. 4.5.e**. At this state, magnesium is coordinated with three hydroxyl groups and 4 water molecules. Two of the hydroxyl groups are solely bonded to the dissolved magnesium, while another hydroxyl shares a bond with a surface magnesium at the step site.

The free energy values along the minimum free energy paths derived for carbonate-assisted and carbonate-unassisted dissolution in **Fig. 4.4-5**, are plotted in **Fig. 4.6.a**. The free energy barriers for the dissolution of carbonate-assisted and carbonate-unassisted Mg^{2+} are respectively 13.2±1.7 and 17.1±2.3 kcal/mol, See **Appendix B Note 1** for the mathematical derivation of error estimation in 2D PMFs. These results are well in the lower range of experimentally measured apparent dissolution activation energies in acidic conditions, see **Fig. 4.6.a**.[261,262] In line with our results, it is shown through experiments that the dissolution of phlogopite [$KMg_{2.87}Si_{3.07}Al_{1.23}O_{10}(F,OH)_2$] is promoted in the presence of organic ligands at the rock-water-scCO_2 interface, despite an increase in the pH value.[263] In **Fig. 4.6.b,** the evolution of the water/water+hydroxyl coordination

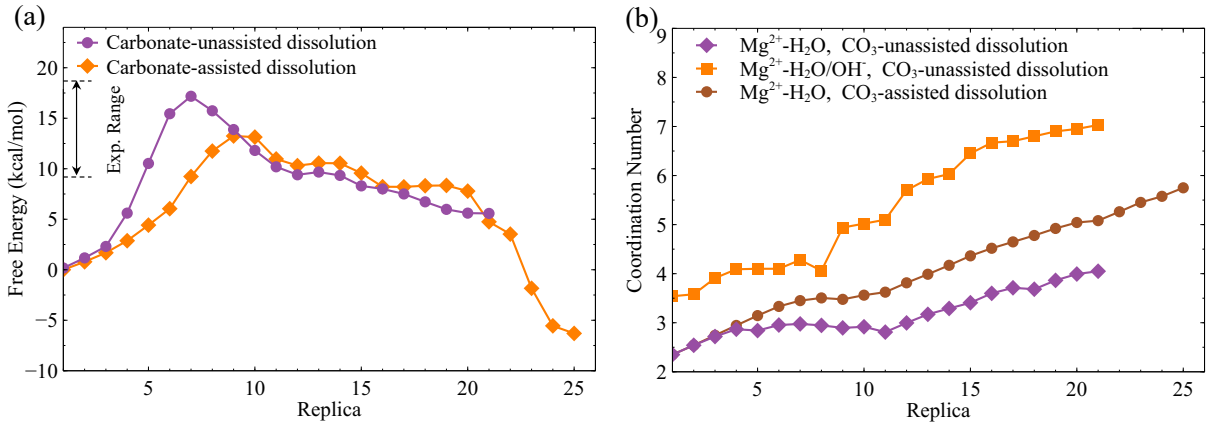

Figure 4.6. The Potential-of-Mean-Force (PMF) for the dissolution of Mg2+ from the surface of forsterite (a) The free energy profile for the dissolution of Mg^{2+} in carbonate -assisted and -unassisted scenarios. The horizontal axis shows the points on the minimum free energy paths derived from the 2D PMF shown in the previous figure. The designated experimental range corresponds to the apparent dissolution energy barriers in acidic conditions, $2 \leq pH \leq 5$ collected by Rimstidt and coworkers.[74] (b) The evolution of magnesium-water/water+hydroxyl groups coordination number as the magnesium moves on the minimum energy paths. The difference between purple and orange paths show the number of hydroxyl groups coordinated around dissolved magnesium

number is plotted as Mg^{2+} departs the surface. While 5-6 water molecules coordinate with the dissolved Mg^{2+} in the carbonate-assisted scenario, four water molecules in the first shell and three hydroxyl groups coordinate around the abstracted Mg^{2+} in the carbonate-unassisted scenario.

Our simulations show that the carbonate-assisted dissolution is slightly favored over carbonate-unassisted dissolution. However, after a partial detachment of magnesium from the surface, the adjacent silicate becomes undercoordinated that can attract nearby protons. The protonation of the undercoordinated silicate decreases the electrostatic attraction between the silicate and the dissolving magnesium ion. The protonation of the adjacent silicate can therefore decrease the electrostatic barrier, compared to what we obtained through free energy calculations, for which we used a non-reactive forcefield. Nonetheless, the aforementioned repulsion between the adsorbed proton and neutral magnesium-carbonate ion pair is theoretically less strong than the repulsion between the proton and the doubly charged magnesium cation. Modeling such a complex dissolution process requires intricate reactive force fields that could take into account the variability of the magnesium charge as it dissolves from the surface to the solution.

4.4 Implications

Although our calculations show a small difference between carbonated-assisted and -unassisted dissolution barrier, we believe that the dissolution of metal-carbonate surface complex could positively affect the rate of nucleation and growth. From statistical mechanics point of view, it is not only the reaction barrier for the attachment of ions or ion pairs to the carbonate nuclei that determines the growth rate, but also the configurational entropy that depends on the distance between the nuclei core and ions/ion-pairs.[264] When two free ions/molecules exist in a bulk solution, the number of degenerate microstates is proportional to $4\pi r^2 dr$, see **Fig. 4.7.a**.

Therefore, the configurational entropy, ΔS_q, when the ion moves from r_1 to r_2 changes as $K_B T \ln(r_1^2/r_2^2) = 2K_B T \ln(r_1/r_2)$, where K_B is the Boltzmann constant and T is the temperature. In contrast, the number of degenerate microstate in the thin water film on the silicate mineral is proportional to $2\pi r dr$ and therefore ΔS_q is equal to $K_B T \ln(r_1/r_2)$, as shown in **Fig. 4.7.b**.

When two free ions like a positive metal ion and a negative carbonate exist in the thin water film and probe the vicinity of a carbonate nucleus, the total number of degenerate microstates is equal to the number of degenerate microstates for carbonate ion at distance r_1 from the nuclei (N_1) times the number of degenerate microstates for metal ion at distance r_2 (N_2), see **Fig. 4.7.d.** However,

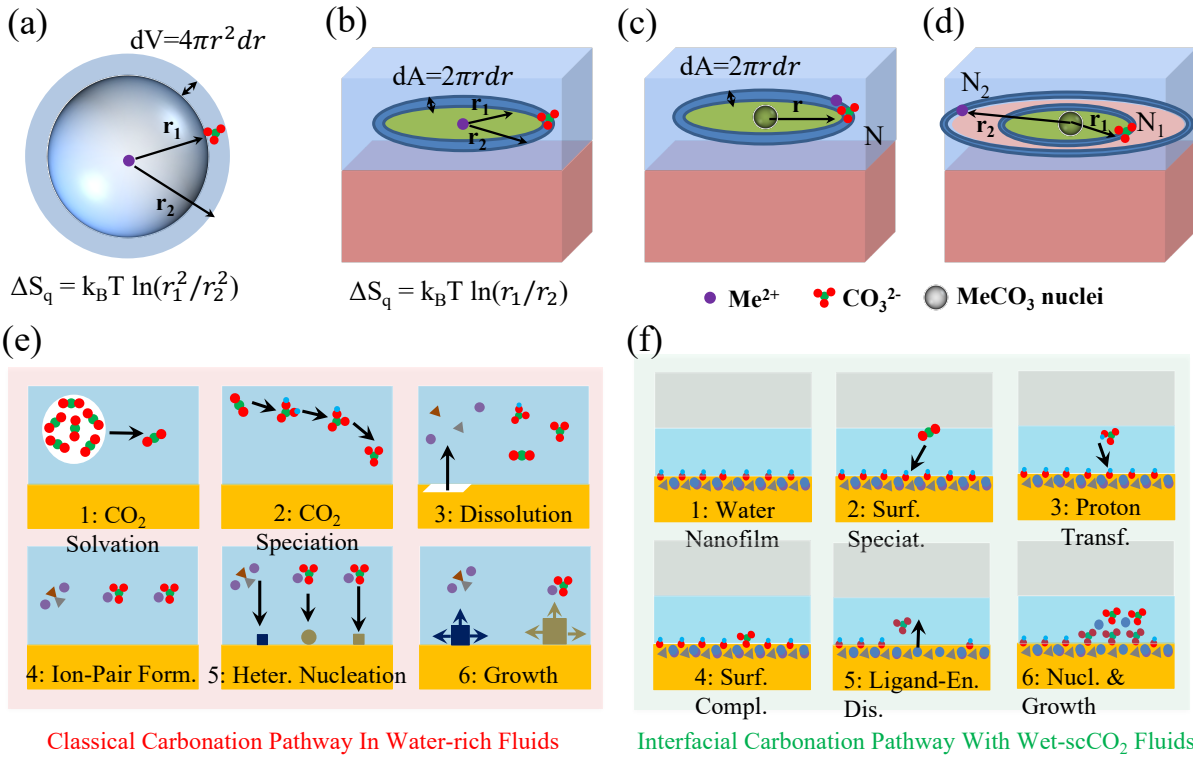

Figure 4.7. Schematics for the nucleation and growth mechanisms in the bulk aqueous solution versus the nucleation and growth at the interface. Configurational entropy contribtuion in growth mechanisms with ion attachment when ions are separated (a) in the bulk aqueous solution and (b) in the adsorbed water nanofilm. Attachment of (c) an ion-pair, and (d) separate carbonate and metal ions to the metal carbonate nuclei in the adsornbed water film or on the surface. (e) the classical carbonation mechanism in water-rich fluids and (f) the interfacial reaction pathway in which a metal silicate rock carbonates in the presence of adsorbed water nanofilms.

when these two ions are already paired as a result of dissolution from the surface, the number of microstates for the carbonate nuclei and the ion-pair distanced away from each other is lower than $N_1 \times N_2$, see **Fig. 4.7.c**. Otherwise said, the possibility of ion pair colliding with the carbonate core is higher than the possibility of separate ions colliding with the carbonate core at the same site. Thus, a precursor carbonate-assisted dissolution would naturally ensure that the configurational entropy is minimized in the classical monomer-by-monomer growth mechanism.

However, we recognize that the attachment of an ion pair to a nucleus might be energetically different at various surface sites, *e.g.,* steps and kinks. Through atomistic simulations, Raiteri et al.[264] show that the attachment of a calcium carbonate ion pair to an amorphous calcium carbonate spherical nucleus is almost barrierless, regardless of its size. This is in contrast to the attachment events to the basal calcite surface that is found to be a limiting step.[264] Interestingly, Mergelsberg et al.[84] observe the formation of amorphous magnesium carbonate nano-particles when carbonating forsterite with wet supercritical CO_2 fluids. Akin to the calcium carbonate system[265], this amorphous phase is a precursor to the formation of thermodynamically stable crystalline magnesium carbonate phases.[84] The observations of amorphous phases suggest that growth in thin adsorbed water nanofilms might be governed by the aforementioned entropic penalty rather than free energy barriers associated with attachment events.

The classical understanding of carbonation kinetics in water-rich fluids is established on the foundation of the dissolution-precipitation pathways.[266] **Fig. 4.7.e** shows a schematic demonstration of such a path that encapsulates different elementary reaction steps ranging from aqueous CO_2 solvation and speciation to proton-promoted dissolution and ion-pair formation that leads ultimately to the heterogeneous nucleation and growth processes via the monomer-by-

monomer addition. There is evidence that these reactions can be spatially limited to the interfacial water film, which might become supersaturated with respect to a new carbonate mineral phase.[267,268] When juxtaposed with spectroscopic data[33,35,36,38], our multi-technique computational framework highlights the presence of a new dissolution path, **Fig. 4.7.f**. In this path, the kinetics of CO_2 speciation is accelerated on the hydroxylated metal silicate surfaces or perhaps in the presence of dissolved cations in the adsorbed water nanofilm[35]. Our reactive simulations show that the carbonic acid and bicarbonate in the nanofilm deprotonate on the basic hydroxylated metal silicate surfaces, **Figs. 4.1-2**. The resultant carbonate either chemisorbs to form a surface metal-carbonate complex as observed in high-pressure spectroscopic measurements[35,36] or actively participates in metal abstraction from the surface using a ligand-enhanced dissolution mechanism, **Fig. 4.4-6**. The dissolved ions and ion pairs are subsequently transported within the nanofilm via a two-dimensional diffusive process[231] that culminate in a monomer-by-monomer growth of metal carbonate crystals. Although the interfacial carbonation path can be classified as a dissolution-precipitation pathway, the silicate surfaces actively engage in the chemical reactions through long-range proton transport and ligand-enhanced dissolution. This can potentially affect macroscopically observed interfacial carbonation kinetics when compared to bulk aqueous phase mediated reactions.

Chapter 5

Conclusions

In this dissertation, we have used atomistic simulation techniques to investigate the properties of rock-water-CO_2 interface to better understand the nano-scale nature of the carbonation process. We have specifically chosen Calcium-Silicate-Hydrate (C-S-H), the binding phase of concrete, and forsterite (Mg_2SiO_4), the magnesium end-member of the olivine group, as our solid models. In chapter 2, we have studied the phase behavior of humidified CO_2-rich phases with different thermodynamic conditions in the slit-pore of the aforementioned minerals. We have found that a nano-meter thick water layer adsorbs on the surface even at under saturated conditions. Also, we have observed overlapping regions at the interface of water-CO_2 which could entail higher carbonic acid formation rate than that in the aqueous phase. Through free energy calculations, we have found that CO_2 could be found in a metastable state when adsorbed on the surface of C-S-H. Our density functional theory calculations show that carbonic acid and bicarbonate could form on the surface of C-S-H with a lower energy barrier compared to the bulk aqueous phase.

In chapter 3, we have developed a reactive force field to model magnesium-bearing systems at the solid-liquid interface and in bulk solids, where magnesium interacts with carbon/oxygen/hydrogen species. Using this force field in chapter 4, we have delved into the interaction of bicarbonate at the rock-water interface. We have found that, after few picoseconds, bicarbonate deprotonates at the interface through a long-range migration of the proton to the surface hydroxyl groups. We also have performed free energy calculation for this deprotonation mechanism, and have found that this

reaction leads to a more stable state when carbonate is formed. We have also observed that the energy barrier for this reaction is low enough to spontaneously occur at room temperature. This is reminiscent of the basic nature of the hydroxylated surface of metal-silicate. Then, the doubly negative charged carbonate adsorbs on the surface to form a metal-carbonate surface complex. This reaction is particularly important when the adsorbed water on the surface has a thickness of about 1 nano-meter, which is small enough for this long-range proton transfer to occur. Therefore, our study suggests that this type of reaction and the subsequent surface complex formation need to be considered in rock-water-CO_2 systems where the surface of the rock is hydroxylated. Finally, we have calculated the free energy landscape for the dissolution of magnesium-carbonate surface complex. We have shown that the magnesium-carbonate ion pair is more stable when dissolved in the adsorbed water film, and the free energy required for this dissolution is somewhat lower than the case where no carbonate exists. Along with the previous reaction and adsorption paths observed in this dissertation, this highlights the role of magnesium-carbonate surface complexes in accelerating the dissolution process. Moreover, we have discussed the aftermath of this scenario where magnsesium-carbonate ion pair dissolves from the surface into the quasi-2D water film environment. Based on statistical mechanics point of view, we have discussed that the presence of ion pairs in the thin water film lowers the penalty regarding configurational entropy for nucleation and growth. Overall, our findings could partly explain the fast mineralization process when a humidified CO_2-rich phase enters the pore network of divalent metal silicates.

References:

1. Tong, D. *et al.* Committed emissions from existing energy infrastructure jeopardize 1.5 °C climate target. *Nature* 1–5 (2019) doi:10.1038/s41586-019-1364-3.
2. Hoffert, M. I. *et al.* Advanced Technology Paths to Global Climate Stability: Energy for a Greenhouse Planet. *Science* (2002) doi:10.1126/science.1072357.
3. Pacala, S. & Socolow, R. Stabilization Wedges: Solving the Climate Problem for the Next 50 Years with Current Technologies. *Science* **305**, 968–972 (2004).
4. Stolaroff, J. K., Lowry, G. V. & Keith, D. W. Using CaO- and MgO-rich industrial waste streams for carbon sequestration. *Energy Conversion and Management* **46**, 687–699 (2005).
5. Rim, G., Marchese, A. K., Stallworth, P., Greenbaum, S. G. & Park, A.-H. A. 29Si solid state MAS NMR study on leaching behaviors and chemical stability of different Mg-silicate structures for CO2 sequestration. *Chemical Engineering Journal* **396**, 125204 (2020).
6. Fernández Bertos, M., Simons, S. J. R., Hills, C. D. & Carey, P. J. A review of accelerated carbonation technology in the treatment of cement-based materials and sequestration of CO2. *Journal of Hazardous Materials* **112**, 193–205 (2004).
7. Bachu, S. CO2 storage in geological media: Role, means, status and barriers to deployment. *Progress in Energy and Combustion Science* **34**, 254–273 (2008).
8. Zoback, M. D. & Gorelick, S. M. Earthquake triggering and large-scale geologic storage of carbon dioxide. *PNAS* **109**, 10164–10168 (2012).
9. Matter, J. M. *et al.* Permanent Carbon Dioxide Storage into Basalt: The CarbFix Pilot Project, Iceland. *Energy Procedia* **1**, 3641–3646 (2009).
10. Matter, J. M. *et al.* Rapid carbon mineralization for permanent disposal of anthropogenic carbon dioxide emissions. *Science* **352**, 1312–1314 (2016).
11. Gislason, S. R. *et al.* Mineral sequestration of carbon dioxide in basalt: A pre-injection overview of the CarbFix project. *International Journal of Greenhouse Gas Control* **4**, 537–545 (2010).
12. McGrail, B. P. *et al.* Field Validation of Supercritical CO2 Reactivity with Basalts. *Environ. Sci. Technol. Lett.* **4**, 6–10 (2017).
13. McGrail, B. P. *et al.* Wallula Basalt Pilot Demonstration Project: Post-injection Results and Conclusions. *Energy Procedia* **114**, 5783–5790 (2017).
14. McGrail, B. P., Spane, F. A., Sullivan, E. C., Bacon, D. H. & Hund, G. The Wallula basalt sequestration pilot project. *Energy Procedia* **4**, 5653–5660 (2011).
15. Kelemen, P. B. *et al.* Engineered carbon mineralization in ultramafic rocks for CO2 removal from air: Review and new insights. *Chemical Geology* **550**, 119628 (2020).
16. White, S. K. *et al.* Quantification of CO2 Mineralization at the Wallula Basalt Pilot Project. *Environ. Sci. Technol.* **54**, 14609–14616 (2020).
17. Pogge von Strandmann, P. A. E. *et al.* Rapid CO2 mineralisation into calcite at the CarbFix storage site quantified using calcium isotopes. *Nat Commun* **10**, 1983 (2019).
18. Gaus, I. Role and impact of CO2–rock interactions during CO2 storage in sedimentary rocks. *International Journal of Greenhouse Gas Control* **4**, 73–89 (2010).
19. Elkhoury, J. E., Ameli, P. & Detwiler, R. L. Dissolution and deformation in fractured carbonates caused by flow of CO2-rich brine under reservoir conditions. *International Journal of Greenhouse Gas Control* **16**, S203–S215 (2013).
20. Anovitz, L. M. *et al.* Diagenetic changes in macro- to nano-scale porosity in the St. Peter Sandstone: An (ultra) small angle neutron scattering and backscattered electron imaging analysis. *Geochimica et Cosmochimica Acta* **102**, 280–305 (2013).

21. Kelemen, P. B. & Hirth, G. Reaction-driven cracking during retrograde metamorphism: Olivine hydration and carbonation. *Earth and Planetary Science Letters* **345–348**, 81–89 (2012).
22. Matter, J. M. & Kelemen, P. B. Permanent storage of carbon dioxide in geological reservoirs by mineral carbonation. *Nature Geoscience* **2**, 837–841 (2009).
23. Abdolhosseine Qomi, M. J. *et al.* Molecular-Scale Mechanisms of CO2 Mineralization in Nanoscale Interfacial Water Films. *Nature Reviews Chemistry* (2022).
24. Giammar, D. E., Bruant, R. G. & Peters, C. A. Forsterite dissolution and magnesite precipitation at conditions relevant for deep saline aquifer storage and sequestration of carbon dioxide. *Chemical Geology* **217**, 257–276 (2005).
25. Spycher, N., Pruess, K. & Ennis-King, J. CO2-H2O mixtures in the geological sequestration of CO2. I. Assessment and calculation of mutual solubilities from 12 to 100°C and up to 600 bar. *Geochimica et Cosmochimica Acta* **67**, 3015–3031 (2003).
26. Gelb, L. D., Gubbins, K. E., Radhakrishnan, R. & Sliwinska-Bartkowiak, M. Phase separation in confined systems. *Rep. Prog. Phys.* **62**, 1573–1659 (1999).
27. Peterson, B. K., Walton, J. P. R. B. & Gubbins, K. E. Fluid behaviour in narrow pores. *J. Chem. Soc., Faraday Trans. 2* **82**, 1789–1800 (1986).
28. Santiso, E. E., George, A. M., Sliwinska-bartkowiak, M., Nardelli, M. B. & Gubbins, K. E. Effect of Confinement on Chemical Reactions. *Adsorption* **1**, 349–354 (2005).
29. Miller, Q. R. S. *et al.* Water Structure Controls Carbonic Acid Formation in Adsorbed Water Films. *J. Phys. Chem. Lett.* **9**, 4988–4994 (2018).
30. Qomi, M. J. A., Bauchy, M., Ulm, F.-J. & Pellenq, R. J.-M. anomalous composition-dependent dynamics of nanoconfined water in the interlayer of disordered calcium-silicates. *The Journal of Chemical Physics* **140**, 054515 (2014).
31. Masoumi, S., Zare, S., Valipour, H. & Abdolhosseini Qomi, M. J. Effective Interactions between Calcium-Silicate-Hydrate Nanolayers. *J. Phys. Chem. C* **123**, 4755–4766 (2019).
32. Loring, J. S., Miller, Q. R. S., Thompson, C. J. & Schaef, H. T. Chapter 4 - Experimental Studies of Reactivity and Transformations of Rocks and Minerals in Water-Bearing Supercritical CO2. in *Science of Carbon Storage in Deep Saline Formations* (eds. Newell, P. & Ilgen, A. G.) 63–88 (Elsevier, 2019). doi:10.1016/B978-0-12-812752-0.00004-6.
33. Loring, J. S. *et al.* In Situ Infrared Spectroscopic Study of Forsterite Carbonation in Wet Supercritical CO2. *Environ. Sci. Technol.* **45**, 6204–6210 (2011).
34. S. Miller, Q. R. *et al.* Anomalously low activation energy of nanoconfined MgCO 3 precipitation. *Chemical Communications* **55**, 6835–6837 (2019).
35. Miller, Q. R. S. *et al.* Surface-Catalyzed Oxygen Exchange during Mineral Carbonation in Nanoscale Water Films. *J. Phys. Chem. C* **123**, 12871–12885 (2019).
36. Loring, J. S. *et al.* Evidence for Carbonate Surface Complexation during Forsterite Carbonation in Wet Supercritical Carbon Dioxide. *Langmuir* **31**, 7533–7543 (2015).
37. Felmy, A. R. *et al.* Reaction of water-saturated supercritical CO2 with forsterite: Evidence for magnesite formation at low temperatures. *Geochimica et Cosmochimica Acta* **91**, 271–282 (2012).
38. Schaef, H. T. *et al.* Forsterite [Mg2SiO4)] Carbonation in Wet Supercritical CO2: An in Situ High-Pressure X-ray Diffraction Study. *Environ. Sci. Technol.* **47**, 174–181 (2013).
39. Lacinska, A. M., Styles, M. T., Bateman, K., Hall, M. & Brown, P. D. An Experimental Study of the Carbonation of Serpentinite and Partially Serpentinised Peridotites. *Frontiers in Earth Science* **5**, 37 (2017).
40. Ming, X.-R. *et al.* Thin-film dawsonite in Jurassic coal measure strata of the Yaojie coalfield, Minhe Basin, China: A natural analogue for mineral carbon storage in wet supercritical CO2. *International Journal of Coal Geology* **180**, 83–99 (2017).
41. Gislason, S. R. & Oelkers, E. H. Carbon Storage in Basalt. *Science* **344**, 373–374 (2014).

42. McGrail, B. P. *et al.* Potential for carbon dioxide sequestration in flood basalts. *Journal of Geophysical Research: Solid Earth* **111**, (2006).
43. Goldberg, D. S., Takahashi, T. & Slagle, A. L. Carbon dioxide sequestration in deep-sea basalt. *PNAS* **105**, 9920–9925 (2008).
44. Goldberg, D. S., Kent, D. V. & Olsen, P. E. Potential on-shore and off-shore reservoirs for CO2 sequestration in Central Atlantic magmatic province basalts. *PNAS* **107**, 1327–1332 (2010).
45. Marieni, C., Henstock, T. J. & Teagle, D. A. H. Geological storage of CO2 within the oceanic crust by gravitational trapping. *Geophysical Research Letters* **40**, 6219–6224 (2013).
46. Snæbjörnsdóttir, S. Ó. *et al.* CO2 storage potential of basaltic rocks in Iceland and the oceanic ridges. *Energy Procedia* **63**, 4585–4600 (2014).
47. Power, I. M. *et al.* Strategizing Carbon-Neutral Mines: A Case for Pilot Projects. *Minerals* **4**, 399–436 (2014).
48. Wilson, S. A. *et al.* Offsetting of CO2 emissions by air capture in mine tailings at the Mount Keith Nickel Mine, Western Australia: Rates, controls and prospects for carbon neutral mining. *International Journal of Greenhouse Gas Control* **25**, 121–140 (2014).
49. Huntzinger, D. N., Gierke, J. S., Sutter, L. L., Kawatra, S. K. & Eisele, T. C. Mineral carbonation for carbon sequestration in cement kiln dust from waste piles. *Journal of Hazardous Materials* **168**, 31–37 (2009).
50. Rim, G. *et al.* CO 2 utilization in built environment via the P CO2 swing carbonation of alkaline solid wastes with different mineralogy. *Faraday Discussions* **230**, 187–212 (2021).
51. O'Connor, W. K., Dahlin, D. C., Rush, G. E., Dahlin, C. L. & Collins, W. K. Carbon dioxide sequestration by direct mineral carbonation: process mineralogy of feed and products. *Mining, Metallurgy & Exploration* **19**, 95–101 (2002).
52. National Academies of Sciences, E. *Negative Emissions Technologies and Reliable Sequestration: A Research Agenda*. (2018). doi:10.17226/25259.
53. Bourg, I. C., Beckingham, L. E. & DePaolo, D. J. The Nanoscale Basis of CO2 Trapping for Geologic Storage. *Environ. Sci. Technol.* **49**, 10265–10284 (2015).
54. Alcalde, J. *et al.* Estimating geological CO 2 storage security to deliver on climate mitigation. *Nature Communications* **9**, 2201 (2018).
55. Chakraborty, N., Karpyn, Z., Liu, S., Yoon, H. & Dewers, T. Experimental evidence of gas densification and enhanced storage in nanoporous shales. *Journal of Natural Gas Science and Engineering* **76**, 103120 (2020).
56. Cihan, A., Tokunaga, T. K. & Birkholzer, J. T. Adsorption and Capillary Condensation-Induced Imbibition in Nanoporous Media. *Langmuir* **35**, 9611–9621 (2019).
57. Tokunaga, T. K. *et al.* Water Saturation Relations and Their Diffusion-Limited Equilibration in Gas Shale: Implications for Gas Flow in Unconventional Reservoirs. *Water Resources Research* **53**, 9757–9770 (2017).
58. Erfani, A., Szutkowski, K., Aichele, C. P. & White, J. L. Diffusion, Interactions, and Disparate Kinetic Trapping of Water–Hydrocarbon Mixtures in Nanoporous Solids. *Langmuir* **37**, 858–866 (2021).
59. Vincent, O., Marguet, B. & Stroock, A. D. Imbibition Triggered by Capillary Condensation in Nanopores. *Langmuir* **33**, 1655–1661 (2017).
60. Cihan, A., Tokunaga, T. K. & Birkholzer, J. T. Diffusion-to-Imbibition Transition in Water Sorption in Nanoporous Media: Theoretical Studies. *Water Resources Research* **57**, e2021WR029720 (2021).
61. Li, H. *et al.* Dynamic behavior of hydration water in calcium-silicate-hydrate gel: A quasielastic neutron scattering spectroscopy investigation. *Phys. Rev. E* **86**, 061505 (2012).
62. Velasco, R., Pathak, M., Panja, P. & Deo, M. What Happens to Permeability at the Nanoscale? A Molecular Dynamics Simulation Study. in *Unconventional Resources Technology Conference, Austin, Texas, 24-26 July 2017* 3248–3257 (Society of Exploration Geophysicists, American

Association of Petroleum Geologists, Society of Petroleum Engineers, 2017). doi:10.15530/urtec-2017-2697415.
63. Abdolhosseini Qomi, M. J. *et al.* Combinatorial molecular optimization of cement hydrates. *Nature Communications* **5**, 4960 (2014).
64. Bauchy, M. *et al.* Fracture toughness anomalies: Viewpoint of topological constraint theory. *Acta Materialia* **121**, 234–239 (2016).
65. Morshedifard, A., Masoumi, S. & Qomi, M. J. A. Nanoscale origins of creep in calcium silicate hydrates. *Nature Communications* **9**, 1785 (2018).
66. Xi, F. *et al.* Substantial global carbon uptake by cement carbonation. *Nature Geoscience* **9**, 880–883 (2016).
67. Boden, T. A., Andres, R. J. & Marland, G. *Global, Regional, and National Fossil-Fuel CO2 Emissions (1751 - 2010) (V. 2013)*. https://www.osti.gov/dataexplorer/biblio/1389328-global-regional-national-fossil-fuel-co2-emissions (2013) doi:10.3334/CDIAC/00001_V2013.
68. Barcelo, L., Kline, J., Walenta, G. & Gartner, E. Cement and carbon emissions. *Mater Struct* **47**, 1055–1065 (2014).
69. Rimmelé, G., Barlet-Gouédard, V., Porcherie, O., Goffé, B. & Brunet, F. Heterogeneous porosity distribution in Portland cement exposed to CO2-rich fluids. *Cement and Concrete Research* **38**, 1038–1048 (2008).
70. Barlet-Gouédard, V., Rimmelé, G., Porcherie, O., Quisel, N. & Desroches, J. A solution against well cement degradation under CO2 geological storage environment. *International Journal of Greenhouse Gas Control* **3**, 206–216 (2009).
71. Chavez Panduro, E. A. *et al.* In-Situ X-ray Tomography Study of Cement Exposed to CO2 Saturated Brine. *Environ. Sci. Technol.* **51**, 9344–9351 (2017).
72. Renforth, P. The negative emission potential of alkaline materials. *Nat Commun* **10**, 1401 (2019).
73. Monteiro, P. J. M. *et al.* Advances in characterizing and understanding the microstructure of cementitious materials. *Cement and Concrete Research* **124**, 105806 (2019).
74. Erras-Hanauer, H., Clark, T. & van Eldik, R. Molecular orbital and DFT studies on water exchange mechanisms of metal ions. *Coordination Chemistry Reviews* **238–239**, 233–253 (2003).
75. Kerisit, S., Weare, J. H. & Felmy, A. R. Structure and dynamics of forsterite–scCO2/H2O interfaces as a function of water content. *Geochimica et Cosmochimica Acta* **84**, 137–151 (2012).
76. Botan, A., Rotenberg, B., Marry, V., Turq, P. & Noetinger, B. Carbon Dioxide in Montmorillonite Clay Hydrates: Thermodynamics, Structure, and Transport from Molecular Simulation. *J. Phys. Chem. C* **114**, 14962–14969 (2010).
77. Kerisit, S., Bylaska, E. J. & Felmy, A. R. Water and carbon dioxide adsorption at olivine surfaces. *Chemical Geology* **359**, 81–89 (2013).
78. Miller, Q. R. S. *et al.* Emerging investigator series: ion diffusivities in nanoconfined interfacial water films contribute to mineral carbonation thresholds. *Environmental Science: Nano* **7**, 1068–1081 (2020).
79. Placencia-Gómez, E. *et al.* Critical Water Coverage during Forsterite Carbonation in Thin Water Films: Activating Dissolution and Mass Transport. *Environ. Sci. Technol.* **54**, 6888–6899 (2020).
80. Thompson, C. J., Loring, J. S., Rosso, K. M. & Wang, Z. Comparative reactivity study of forsterite and antigorite in wet supercritical CO2 by in situ infrared spectroscopy. *International Journal of Greenhouse Gas Control* **18**, 246–255 (2013).
81. Thompson, C. J. *et al.* Automated high-pressure titration system with in situ infrared spectroscopic detection. *Review of Scientific Instruments* **85**, 044102 (2014).
82. Zhang, X. *et al.* In situ imaging of amorphous intermediates during brucite carbonation in supercritical CO2. *Nat. Mater.* 1–7 (2021) doi:10.1038/s41563-021-01154-5.

83. Kerisit, S. N., Mergelsberg, S. T., Thompson, C. J., White, S. K. & Loring, J. S. Thin Water Films Enable Low-Temperature Magnesite Growth Under Conditions Relevant to Geologic Carbon Sequestration. *Environ. Sci. Technol.* **55**, 12539–12548 (2021).
84. Mergelsberg, S. T. *et al.* Low temperature and limited water activity reveal a pathway to magnesite via amorphous magnesium carbonate. *Chemical Communications* **56**, 12154–12157 (2020).
85. Smith, R. S., Li, Z., Dohnálek, Z. & Kay, B. D. Adsorption, Desorption, and Displacement Kinetics of H2O and CO2 on Forsterite, Mg2SiO4(011). *J. Phys. Chem. C* **118**, 29091–29100 (2014).
86. M. G. Martin; 'MCCCS Towhee: a tool for Monte Carlo molecular simulation', Mol. Simulat. 39 1212-1222 (2013).
87. Mooij, G. C. A. M., Frenkel, D. & Smit, B. Direct simulation of phase equilibria of chain molecules. *J. Phys.: Condens. Matter* **4**, L255 (1992).
88. Berendsen, H. J. C., Postma, J. P. M., van Gunsteren, W. F. & Hermans, J. Interaction Models for Water in Relation to Protein Hydration. in *Intermolecular Forces: Proceedings of the Fourteenth Jerusalem Symposium on Quantum Chemistry and Biochemistry Held in Jerusalem, Israel, April 13–16, 1981* (ed. Pullman, B.) 331–342 (Springer Netherlands, 1981). doi:10.1007/978-94-015-7658-1_21.
89. Harris, J. G. & Yung, K. H. Carbon Dioxide's Liquid-Vapor Coexistence Curve And Critical Properties as Predicted by a Simple Molecular Model. *J. Phys. Chem.* **99**, 12021–12024 (1995).
90. Cygan, R. T., Liang, J.-J. & Kalinichev, A. G. Molecular Models of Hydroxide, Oxyhydroxide, and Clay Phases and the Development of a General Force Field. *J. Phys. Chem. B* **108**, 1255–1266 (2004).
91. Qomi, M. J. A. *et al.* Combinatorial molecular optimization of cement hydrates. *Nature Communications* **5**, 4960 (2014).
92. Yan, H. *et al.* Termination and hydration of forsteritic olivine (010) surface. *Geochimica et Cosmochimica Acta* **145**, 268–280 (2014).
93. King, H. E. *et al.* Computer simulations of water interactions with low-coordinated forsterite surface sites: Implications for the origin of water in the inner solar system. *Earth and Planetary Science Letters* **300**, 11–18 (2010).
94. de Leeuw, N. H., Parker, S. C., Catlow, C. R. A. & Price, G. D. Modelling the effect of water on the surface structure and stability of forsterite. *Phys Chem Min* **27**, 332–341 (2000).
95. Plimpton, S. Fast Parallel Algorithms for Short-Range Molecular Dynamics. *Journal of Computational Physics* **117**, 1–19 (1995).
96. Berendsen, H. J. C., Grigera, J. R. & Straatsma, T. P. The missing term in effective pair potentials. *J. Phys. Chem.* **91**, 6269–6271 (1987).
97. Cygan, R. T., Romanov, V. N. & Myshakin, E. M. Molecular Simulation of Carbon Dioxide Capture by Montmorillonite Using an Accurate and Flexible Force Field. *J. Phys. Chem. C* **116**, 13079–13091 (2012).
98. Tribello, G. A., Bonomi, M., Branduardi, D., Camilloni, C. & Bussi, G. PLUMED 2: New feathers for an old bird. *Computer Physics Communications* **185**, 604–613 (2014).
99. Shahsavari, R., J.-M. Pellenq, R. & Ulm, F.-J. Empirical force fields for complex hydrated calcio-silicate layered materials. *Physical Chemistry Chemical Physics* **13**, 1002–1011 (2011).
100. Kumar, S., Rosenberg, J. M., Bouzida, D., Swendsen, R. H. & Kollman, P. A. THE weighted histogram analysis method for free-energy calculations on biomolecules. I. The method. *Journal of Computational Chemistry* **13**, 1011–1021 (1992).
101. Funk, A. & Trettin, H. F. R. DFT Study on the Effect of Water on the Carbonation of Portlandite. *Ind. Eng. Chem. Res.* **52**, 2168–2173 (2013).
102. Car, R. & Parrinello, M. Unified Approach for Molecular Dynamics and Density-Functional Theory. *Phys. Rev. Lett.* **55**, 2471–2474 (1985).

103. VandeVondele, J. & Hutter, J. Gaussian basis sets for accurate calculations on molecular systems in gas and condensed phases. *The Journal of Chemical Physics* **127**, 114105 (2007).
104. Goedecker, S., Teter, M. & Hutter, J. Separable dual-space Gaussian pseudopotentials. *Phys. Rev. B* **54**, 1703–1710 (1996).
105. Hartwigsen, C., Goedecker, S. & Hutter, J. Relativistic separable dual-space Gaussian pseudopotentials from H to Rn. *Phys. Rev. B* **58**, 3641–3662 (1998).
106. Krack, M. Pseudopotentials for H to Kr optimized for gradient-corrected exchange-correlation functionals. *Theor Chem Acc* **114**, 145–152 (2005).
107. Perdew, J. P., Burke, K. & Ernzerhof, M. Generalized Gradient Approximation Made Simple. *Phys. Rev. Lett.* **77**, 3865–3868 (1996).
108. Zhang, Y. & Yang, W. Comment on ``Generalized Gradient Approximation Made Simple''. *Phys. Rev. Lett.* **80**, 890–890 (1998).
109. Grimme, S., Antony, J., Ehrlich, S. & Krieg, H. A consistent and accurate ab initio parametrization of density functional dispersion correction (DFT-D) for the 94 elements H-Pu. *The Journal of Chemical Physics* **132**, 154104 (2010).
110. Trygubenko, S. A. & Wales, D. J. A doubly nudged elastic band method for finding transition states. *J Chem Phys* **120**, 2082–2094 (2004).
111. Henkelman, G. & Jónsson, H. Improved tangent estimate in the nudged elastic band method for finding minimum energy paths and saddle points. *The Journal of Chemical Physics* **113**, 9978–9985 (2000).
112. Henkelman, G., Uberuaga, B. P. & Jónsson, H. A climbing image nudged elastic band method for finding saddle points and minimum energy paths. *The Journal of Chemical Physics* **113**, 9901–9904 (2000).
113. Hamid, S. A. The crystal structure of the 11Å natural tobermorite Ca2.25[Si3O7.5(OH)1.5] · 1H2O. *Zeitschrift fur Kristallographie* **154**, 189–198 (1981).
114. Peuble, S. *et al.* Multi-scale characterization of the incipient carbonation of peridotite. *Chemical Geology* **476**, 150–160 (2018).
115. Marquardt, K. & Faul, U. H. The structure and composition of olivine grain boundaries: 40 years of studies, status and current developments. *Phys Chem Minerals* **45**, 139–172 (2018).
116. Xing, T., Zhu, W., Fusseis, F. & Lisabeth, H. Generating porosity during olivine carbonation via dissolution channels and expansion cracks. *Solid Earth* **9**, 879–896 (2018).
117. Erdmann, S., Scaillet, B., Martel, C. & Cadoux, A. Characteristic Textures of Recrystallized, Peritectic, and Primary Magmatic Olivine in Experimental Samples and Natural Volcanic Rocks. *Journal of Petrology* **55**, 2377–2402 (2014).
118. Luhmann, A. J. *et al.* Permeability, porosity, and mineral surface area changes in basalt cores induced by reactive transport of CO2-rich brine. *Water Resources Research* **53**, 1908–1927 (2017).
119. Silvestri, A. *et al.* Wetting Properties of the CO2–Water–Calcite System via Molecular Simulations: Shape and Size Effects. *Langmuir* **35**, 16669–16678 (2019).
120. Silvestri, A. *et al.* A Quantum Mechanically Derived Force Field To Predict CO2 Adsorption on Calcite {10.4} in an Aqueous Environment. *J. Phys. Chem. C* **121**, 24025–24035 (2017).
121. Qomi, M. J. A., Bauchy, M., Ulm, F.-J. & Pellenq, R. J.-M. Anomalous composition-dependent dynamics of nanoconfined water in the interlayer of disordered calcium-silicates. *The Journal of Chemical Physics* **140**, 054515 (2014).
122. Youssef, M., Pellenq, R. J.-M. & Yildiz, B. Glassy Nature of Water in an Ultraconfining Disordered Material: The Case of Calcium−Silicate−Hydrate. *J. Am. Chem. Soc.* **133**, 2499–2510 (2011).
123. Diamond, L. W. & Akinfiev, N. N. Solubility of CO2 in water from −1.5 to 100 °C and from 0.1 to 100 MPa: evaluation of literature data and thermodynamic modelling. *Fluid Phase Equilibria* **208**, 265–290 (2003).

124. Li, Q., Steefel, C. I. & Jun, Y.-S. Incorporating Nanoscale Effects into a Continuum-Scale Reactive Transport Model for CO2-Deteriorated Cement. *Environ. Sci. Technol.* **51**, 10861–10871 (2017).
125. Scherer, G. W. & Huet, B. Carbonation of wellbore cement by CO2 diffusion from caprock. *International Journal of Greenhouse Gas Control* **3**, 731–735 (2009).
126. Raoof, A., Nick, H. M., Wolterbeek, T. K. T. & Spiers, C. J. Pore-scale modeling of reactive transport in wellbore cement under CO2 storage conditions. *International Journal of Greenhouse Gas Control* **11**, S67–S77 (2012).
127. Pavlov, M., Siegbahn, P. E. M. & Sandström, M. Hydration of Beryllium, Magnesium, Calcium, and Zinc Ions Using Density Functional Theory. *J. Phys. Chem. A* **102**, 219–228 (1998).
128. Chen, S. & Navrotsky, A. Calorimetric study of the surface energy of forsterite. *American Mineralogist* **95**, 112–117 (2010).
129. Wu, Y., Tepper, H. L. & Voth, G. A. Flexible simple point-charge water model with improved liquid-state properties. *J. Chem. Phys.* **124**, 024503 (2006).
130. Vorholz, J., Harismiadis, V. I., Rumpf, B., Panagiotopoulos, A. Z. & Maurer, G. Vapor+liquid equilibrium of water, carbon dioxide, and the binary system, water+carbon dioxide, from molecular simulation. *Fluid Phase Equilibria* **170**, 203–234 (2000).
131. Nakouzi, E. *et al.* Moving beyond the Solvent-Tip Approximation to Determine Site-Specific Variations of Interfacial Water Structure through 3D Force Microscopy. *J. Phys. Chem. C* **125**, 1282–1291 (2021).
132. da Rocha, S. R. P., Johnston, K. P., Westacott, R. E. & Rossky, P. J. Molecular Structure of the Water−Supercritical CO2 Interface. *J. Phys. Chem. B* **105**, 12092–12104 (2001).
133. Kvamme, B., Graue, A., Buanes, T., Kuznetsova, T. & Ersland, G. Storage of CO2 in natural gas hydrate reservoirs and the effect of hydrate as an extra sealing in cold aquifers. *International Journal of Greenhouse Gas Control* **1**, 236–246 (2007).
134. Kuznetsova, T. & Kvamme, B. Thermodynamic properties and interfacial tension of a model water–carbon dioxide system. *Physical Chemistry Chemical Physics* **4**, 937–941 (2002).
135. Espinoza, D. N. & Santamarina, J. C. Water-CO2-mineral systems: Interfacial tension, contact angle, and diffusion—Implications to CO2 geological storage. *Water Resources Research* **46**, (2010).
136. J?nsson, H., Mills, G. & Jacobsen, K. W. Nudged elastic band method for finding minimum energy paths of transitions. in *Classical and Quantum Dynamics in Condensed Phase Simulations* 385–404 (WORLD SCIENTIFIC, 1998). doi:10.1142/9789812839664_0016.
137. Schaef, H. T. *et al.* Competitive sorption of CO2 and H2O in 2:1 layer phyllosilicates. *Geochimica et Cosmochimica Acta* **161**, 248–257 (2015).
138. Loring, J. S. *et al.* In Situ Study of CO2 and H2O Partitioning between Na–Montmorillonite and Variably Wet Supercritical Carbon Dioxide. *Langmuir* **30**, 6120–6128 (2014).
139. Burghaus, U. Surface chemistry of CO2 – Adsorption of carbon dioxide on clean surfaces at ultrahigh vacuum. *Progress in Surface Science* **89**, 161–217 (2014).
140. Stirling, A. HCO3– Formation from CO2 at High pH: Ab Initio Molecular Dynamics Study. *J. Phys. Chem. B* **115**, 14683–14687 (2011).
141. Nguyen, M. T. *et al.* Mechanism of the Hydration of Carbon Dioxide: Direct Participation of H2O versus Microsolvation. *J. Phys. Chem. A* **112**, 10386–10398 (2008).
142. Yamabe, S. & Kawagishi, N. A computational study on the relationship between formation and electrolytic dissociation of carbonic acid. *Theor Chem Acc* **130**, 909–918 (2011).
143. Stirling, A. & Pápai, I. H2CO3 Forms via HCO3− in Water. *J. Phys. Chem. B* **114**, 16854–16859 (2010).
144. Silva, J. J. R. F. da & Williams, R. J. P. *The Biological Chemistry of the Elements: The Inorganic Chemistry of Life*. (OUP Oxford, 2001).

145. Taub, A. I. & Luo, A. A. Advanced lightweight materials and manufacturing processes for automotive applications. *MRS Bulletin* **40**, 1045–1054 (2015).
146. Höche, D. *et al.* Performance boost for primary magnesium cells using iron complexing agents as electrolyte additives. *Scientific Reports* **8**, 7578 (2018).
147. Snæbjörnsdóttir, S. Ó. *et al.* Carbon dioxide storage through mineral carbonation. *Nat Rev Earth Environ* **1**, 90–102 (2020).
148. Markham, G. D., Glusker, J. P. & Bock, C. W. The Arrangement of First- and Second-Sphere Water Molecules in Divalent Magnesium Complexes: Results from Molecular Orbital and Density Functional Theory and from Structural Crystallography. *J. Phys. Chem. B* **106**, 5118–5134 (2002).
149. Xu, J. *et al.* Testing the cation-hydration effect on the crystallization of Ca–Mg–CO3 systems. *PNAS* **110**, 17750–17755 (2013).
150. Qafoku, O. *et al.* Dynamics of Magnesite Formation at Low Temperature and High pCO2 in Aqueous Solution. *Environ. Sci. Technol.* **49**, 10736–10744 (2015).
151. Qafoku, O. *et al.* Formation of submicron magnesite during reaction of natural forsterite in H2O-saturated supercritical CO2. *Geochimica et Cosmochimica Acta* **134**, 197–209 (2014).
152. Miller, Q. R. S. *et al.* Quantitative Review of Olivine Carbonation Kinetics: Reactivity Trends, Mechanistic Insights, and Research Frontiers. *Environ. Sci. Technol. Lett.* **6**, 431–442 (2019).
153. Miller, Q. R. S. *et al.* Anomalously low activation energy of nanoconfined MgCO3 precipitation. *Chemical Communications* **55**, 6835–6837 (2019).
154. Liu, T. *et al.* Structure and dynamics of water on the forsterite surface. *Physical Chemistry Chemical Physics* **20**, 27822–27829 (2018).
155. Zachara, J. *et al.* Internal Domains of Natural Porous Media Revealed: Critical Locations for Transport, Storage, and Chemical Reaction. *Environ. Sci. Technol.* **50**, 2811–2829 (2016).
156. Gautier, Q., Bénézeth, P. & Schott, J. Magnesite growth inhibition by organic ligands: An experimental study at 100, 120 and 146°C. *Geochimica et Cosmochimica Acta* **181**, 101–125 (2016).
157. Miller, Q. R. S., Kaszuba, J. P., Schaef, H. T., Bowden, M. E. & McGrail, B. P. Impacts of Organic Ligands on Forsterite Reactivity in Supercritical CO2 Fluids. *Environ. Sci. Technol.* **49**, 4724–4734 (2015).
158. Morrow, C. P., Olsen, A. A. & Kubicki, J. D. Quantum mechanical modeling of hydrolysis and H2O-exchange in Mg-, Ca-, and Ni-silicate clusters: Implications for dissolution mechanisms of olivine minerals. *American Mineralogist* **99**, 2303–2312 (2014).
159. Prigiobbe, V., Suarez Negreira, A. & Wilcox, J. Interaction between Olivine and Water Based on Density Functional Theory Calculations. *J. Phys. Chem. C* **117**, 21203–21216 (2013).
160. Raiteri, P., Demichelis, R. & Gale, J. D. Thermodynamically Consistent Force Field for Molecular Dynamics Simulations of Alkaline-Earth Carbonates and Their Aqueous Speciation. *J. Phys. Chem. C* **119**, 24447–24458 (2015).
161. Gale, J. D., Raiteri, P. & van Duin, A. C. T. A reactive force field for aqueous-calcium carbonate systems. *Physical Chemistry Chemical Physics* **13**, 16666–16679 (2011).
162. Russo, M. F. & van Duin, A. C. T. Atomistic-scale simulations of chemical reactions: Bridging from quantum chemistry to engineering. *Nuclear Instruments and Methods in Physics Research Section B: Beam Interactions with Materials and Atoms* **269**, 1549–1554 (2011).
163. Song, G. L. & Atrens, A. Corrosion Mechanisms of Magnesium Alloys. *Advanced Engineering Materials* **1**, 11–33 (1999).
164. Rappe, A. K. & Goddard, W. A. Charge equilibration for molecular dynamics simulations. *J. Phys. Chem.* **95**, 3358–3363 (1991).
165. Nakano, A. Parallel multilevel preconditioned conjugate-gradient approach to variable-charge molecular dynamics. *Computer Physics Communications* **104**, 59–69 (1997).

166. Aktulga, H. M., Fogarty, J. C., Pandit, S. A. & Grama, A. Y. Parallel reactive molecular dynamics: Numerical methods and algorithmic techniques. *Parallel Computing* **38**, 245–259 (2012).
167. Mortier, W., Ghosh, S. K. & Shankar, S. Electronegativity Equalization Methods for the Calculation of Atomic Charges in Molecules. *J Am Chem Soc* **108**, 4315–4320 (1986).
168. Vajeeston, P., Ravindran, P., Kjekshus, A. & Fjellvåg, H. Pressure-Induced Structural Transitions in ${\mathrm{M}\mathrm{g}\mathrm{H}}_{2}$. *Phys. Rev. Lett.* **89**, 175506 (2002).
169. Karen, P., Kjekshus, A., Huang, Q. & Karen, V. L. The crystal structure of magnesium dicarbide. *Journal of Alloys and Compounds* **282**, 72–75 (1999).
170. Xia, X., Weidner, D. J. & Zhao, H. Equation of state of brucite; single-crystal Brillouin spectroscopy study and polycrystalline pressure-volume-temperature measurement. *American Mineralogist* **83**, 68–74 (1998).
171. Zigan, F. & Rothbauer, R. Neutronenbeugungsmessungen am brucit. *Neues Jahrbuch f{\"u}r Mineralogie Monatshefte* **1967**, 137–143 (1967).
172. Sasaki, S., Fujino, K. & Takéuchi, Y. X-Ray Determination of Electron-Density Distributions in Oxides, MgO, MnO, CoO, and NiO, and Atomic Scattering Factors of their Constituent Atoms. *Proceedings of the Japan Academy, Series B* **55**, 43–48 (1979).
173. Ross, N. L. The equation of state and high-pressure behavior of magnesite. *American Mineralogist* **82**, 682–688 (2015).
174. Catti, M., Pavese, A., Dovesi, R. & Saunders, V. R. Static lattice and electron properties of ${\mathrm{MgCO}}_{3}$ (magnesite) calculated by ab initio periodic Hartree-Fock methods. *Phys. Rev. B* **47**, 9189–9198 (1993).
175. Markham, G. D., Glusker, J. P., Bock, C. L., Trachtman, M. & Bock, C. W. Hydration Energies of Divalent Beryllium and Magnesium Ions: An ab Initio Molecular Orbital Study. *J. Phys. Chem.* **100**, 3488–3497 (1996).
176. Frisch, M. J. *et al.* Gaussian 16. *Revision A* **3**, (2016).
177. Becke, A. D. Density-functional thermochemistry. III. The role of exact exchange. *J. Chem. Phys.* **98**, 5648–5652 (1993).
178. Lee, C., Yang, W. & Parr, R. G. Development of the Colle-Salvetti correlation-energy formula into a functional of the electron density. *Phys. Rev. B* **37**, 785–789 (1988).
179. Li, X. & Frisch, M. J. Energy-Represented Direct Inversion in the Iterative Subspace within a Hybrid Geometry Optimization Method. *J. Chem. Theory Comput.* **2**, 835–839 (2006).
180. Krack, M. & Köster, A. M. An adaptive numerical integrator for molecular integrals. *J. Chem. Phys.* **108**, 3226–3234 (1998).
181. Grimme, S., Antony, J., Ehrlich, S. & Krieg, H. A consistent and accurate ab initio parametrization of density functional dispersion correction (DFT-D) for the 94 elements H-Pu. *Journal of Chemical Physics* **132**, 154104–154104 (2010).
182. Grimme, S., Ehrlich, S. & Goerigk, L. Effect of the damping function in dispersion corrected density functional theory. *Journal of Computational Chemistry* **32**, 1456–1465 (2011).
183. Furthmüller, J. & Kresse, G. Efficient iterative schemes for ab initio total-energy calculations using a plane-wave basis set. *Phys. Rev. B* **54**, 11169–11186 (1996).
184. Kresse, G. & Joubert, D. From ultrasoft pseudopotentials to the projector augmented-wave method. *Phys. Rev. B* **59**, 1758–1775 (1999).
185. Thanthiriwatte, K. S., Hohenstein, E. G., Burns, L. A. & Sherrill, C. D. Assessment of the Performance of DFT and DFT-D Methods for Describing Distance Dependence of Hydrogen-Bonded Interactions. *J. Chem. Theory Comput.* **7**, 88–96 (2011).
186. Torres, E. & DiLabio, G. A. A (Nearly) Universally Applicable Method for Modeling Noncovalent Interactions Using B3LYP. *J. Phys. Chem. Lett.* **3**, 1738–1744 (2012).
187. Duboué-Dijon, E., Mason, P. E., Fischer, H. E. & Jungwirth, P. Hydration and Ion Pairing in Aqueous Mg2+ and Zn2+ Solutions: Force-Field Description Aided by Neutron Scattering

Experiments and Ab Initio Molecular Dynamics Simulations. *J. Phys. Chem. B* **122**, 3296–3306 (2018).
188. Kerisit, S. & Parker, S. C. Free Energy of Adsorption of Water and Metal Ions on the {10$\bar{1}$4} Calcite Surface. *J. Am. Chem. Soc.* **126**, 10152–10161 (2004).
189. Galib, M. *et al.* Revisiting the hydration structure of aqueous Na+. *J. Chem. Phys.* **146**, 084504 (2017).
190. Brik, M. G. First-principles calculations of structural, electronic, optical and elastic properties of magnesite MgCO3 and calcite CaCO3. *Physica B: Condensed Matter* **406**, 1004–1012 (2011).
191. Reeder, R. J. & Markgraf, S. A. High-temperature crystal chemistry of dolomite. *American Mineralogist* **71**, 795–804 (1986).
192. Ross, N. L. & Reeder, R. J. High-pressure structural study of dolomite and ankerite. *American Mineralogist* **77**, 412–421 (1992).
193. Chen, P.-F., Chiao, L.-Y., Huang, P., Yang, Y. & Liu, L. Elasticity of magnesite and dolomite from a genetic algorithm for inverting Brillouin spectroscopy measurements. *Physics of the Earth and Planetary Interiors* **155**, 73–86 (2006).
194. McGrail, B. P., Schaef, H. T., Glezakou, V.-A., Dang, L. X. & Owen, A. T. Water reactivity in the liquid and supercritical CO2 phase: Has half the story been neglected? *Energy Procedia* **1**, 3415–3419 (2009).
195. Eliaz, N. & Gileadi, E. *Physical Electrochemistry: Fundamentals, Techniques, and Applications*. (John Wiley & Sons, 2019).
196. Asaduzzaman, A., Muralidharan, K. & Ganguly, J. Incorporation of water into olivine during nebular condensation: Insights from density functional theory and thermodynamics, and implications for phyllosilicate formation and terrestrial water inventory. *Meteoritics & Planetary Science* **50**, 578–589 (2015).
197. Pokrovsky, O. S., Schott, J. & Thomas, F. Processes at the magnesium-bearing carbonates/solution interface. I. a surface speciation model for magnesite. *Geochimica et Cosmochimica Acta* **63**, 863–880 (1999).
198. Pokrovsky, O. S. & Schott, J. Processes at the magnesium-bearing carbonates/solution interface. II. kinetics and mechanism of magnesite dissolution. *Geochimica et Cosmochimica Acta* **63**, 881–897 (1999).
199. Wright, K., T. Cygan, R. & Slater, B. Structure of the (101[combining macron]4) surfaces of calcite , dolomite and magnesite under wet and dry conditions. *Physical Chemistry Chemical Physics* **3**, 839–844 (2001).
200. Michalkova, A., Ilchenko, M., Gorb, L. & Leszczynski, J. Theoretical Study of the Adsorption and Decomposition of Sarin on Magnesium Oxide. *J. Phys. Chem. B* **108**, 5294–5303 (2004).
201. Hewlett, P. & Liska, M. *Lea's Chemistry of Cement and Concrete*. (Butterworth-Heinemann, 2019).
202. Jug, K., Heidberg, B. & Bredow, T. Cyclic Cluster Study on the Formation of Brucite from Periclase and Water. *J. Phys. Chem. C* **111**, 13103–13108 (2007).
203. Yeon, J. & van Duin, A. C. T. ReaxFF Molecular Dynamics Simulations of Hydroxylation Kinetics for Amorphous and Nano-Silica Structure, and Its Relations with Atomic Strain Energy. *J. Phys. Chem. C* **120**, 305–317 (2016).
204. Water on the MgO(001) Surface: Surface Reconstruction and Ion Solvation | The Journal of Physical Chemistry Letters. https://pubs.acs.org/doi/abs/10.1021/acs.jpclett.5b00885.
205. Markov, I. V. *Crystal Growth for Beginners: Fundamentals of Nucleation, Crystal Growth and Epitaxy*. (WORLD SCIENTIFIC, 2003). doi:10.1142/5172.
206. Saldi, G. D., Jordan, G., Schott, J. & Oelkers, E. H. Magnesite growth rates as a function of temperature and saturation state. *Geochimica et Cosmochimica Acta* **73**, 5646–5657 (2009).

207. Wieland, E., Wehrli, B. & Stumm, W. The coordination chemistry of weathering: III. A generalization on the dissolution rates of minerals. *Geochimica et Cosmochimica Acta* **52**, 1969–1981 (1988).
208. Stefánsson, A., Lemke, K. H., Bénézeth, P. & Schott, J. Magnesium bicarbonate and carbonate interactions in aqueous solutions: An infrared spectroscopic and quantum chemical study. *Geochimica et Cosmochimica Acta* **198**, 271–284 (2017).
209. Di Tommaso, D. & De Leeuw, N. H. First Principles Simulations of the Structural and Dynamical Properties of Hydrated Metal Ions Me2+ and Solvated Metal Carbonates (Me = Ca, Mg, and Sr). in *Crystal growth & design* vol. 10 4292–4302 (2010).
210. Siebert, R. M. & Hostetler, P. B. The stability of the magnesium carbonate ion pair from 10 degrees to 90 degrees C. *American Journal of Science* **277**, 716–734 (1977).
211. Hoegh-Guldberg, O. *et al.* Coral Reefs Under Rapid Climate Change and Ocean Acidification. *Science* **318**, 1737–1742 (2007).
212. Lackner, K. S. Carbonate Chemistry for Sequestering Fossil Carbon. *Annual Review of Energy and the Environment* **27**, 193–232 (2002).
213. Ohtaki, Hitoshi. & Radnai, Tamas. Structure and dynamics of hydrated ions. *Chem. Rev.* **93**, 1157–1204 (1993).
214. Obst, S. & Bradaczek, H. Molecular Dynamics Study of the Structure and Dynamics of the Hydration Shell of Alkaline and Alkaline-Earth Metal Cations. *J. Phys. Chem.* **100**, 15677–15687 (1996).
215. Lam, R. K. *et al.* The hydration structure of aqueous carbonic acid from X-ray absorption spectroscopy. *Chemical Physics Letters* **614**, 282–286 (2014).
216. Kumar, P. P., Kalinichev, A. G. & Kirkpatrick, R. J. Hydrogen-Bonding Structure and Dynamics of Aqueous Carbonate Species from Car−Parrinello Molecular Dynamics Simulations. *J. Phys. Chem. B* **113**, 794–802 (2009).
217. Bruneval, F., Donadio, D. & Parrinello, M. Molecular Dynamics Study of the Solvation of Calcium Carbonate in Water. *J. Phys. Chem. B* **111**, 12219–12227 (2007).
218. Entezari Zarandi, A., Larachi, F., Beaudoin, G., Plante, B. & Sciortino, M. Multivariate study of the dynamics of CO2 reaction with brucite-rich ultramafic mine tailings. *International Journal of Greenhouse Gas Control* **52**, 110–119 (2016).
219. Harrison, A. L., Power, I. M. & Dipple, G. M. Accelerated Carbonation of Brucite in Mine Tailings for Carbon Sequestration. *Environ. Sci. Technol.* **47**, 126–134 (2013).
220. Zare, S., Uddin, K. M. S., Funk, A. & Abdolhosseini Qomi, M. J. Interfacial Reaction Pathways for Docking CO2 in Natural and Synthetic Rocks. *Environmental Science & Technology* **Under Review**, (2021).
221. Tocci, G. & Michaelides, A. Solvent-Induced Proton Hopping at a Water–Oxide Interface. *J. Phys. Chem. Lett.* **5**, 474–480 (2014).
222. Andrade, M. F. C., Ko, H.-Y., Zhang, L., Car, R. & Selloni, A. Free energy of proton transfer at the water–TiO 2 interface from ab initio deep potential molecular dynamics. *Chemical Science* **11**, 2335–2341 (2020).
223. Merte, L. R. *et al.* Water-Mediated Proton Hopping on an Iron Oxide Surface. *Science* **336**, 889–893 (2012).
224. Wendt, S. *et al.* Formation and Splitting of Paired Hydroxyl Groups on Reduced ${\mathrm{TiO}}_{2}(110)$. *Phys. Rev. Lett.* **96**, 066107 (2006).
225. Comtet, J. *et al.* Direct observation of water-mediated single-proton transport between hBN surface defects. *Nature Nanotechnology* **15**, 598–604 (2020).
226. Comtet, J. *et al.* Anomalous interfacial dynamics of single proton charges in binary aqueous solutions. *arXiv:2101.00231 [cond-mat]* (2021).

227. Marx, D., Chandra, A. & Tuckerman, M. E. Aqueous Basic Solutions: Hydroxide Solvation, Structural Diffusion, and Comparison to the Hydrated Proton. *Chem. Rev.* **110**, 2174–2216 (2010).
228. Riccardi, D. *et al.* "Proton Holes" in Long-Range Proton Transfer Reactions in Solution and Enzymes: A Theoretical Analysis. *J. Am. Chem. Soc.* **128**, 16302–16311 (2006).
229. Riccardi, D., König, P., Guo, H. & Cui, Q. Proton Transfer in Carbonic Anhydrase Is Controlled by Electrostatics Rather than the Orientation of the Acceptor. *Biochemistry* **47**, 2369–2378 (2008).
230. Zhang, W. & van Duin, A. C. T. Second-Generation ReaxFF Water Force Field: Improvements in the Description of Water Density and OH-Anion Diffusion. *J. Phys. Chem. B* **121**, 6021–6032 (2017).
231. S. Miller, Q. R. *et al.* Emerging investigator series: ion diffusivities in nanoconfined interfacial water films contribute to mineral carbonation thresholds. *Environmental Science: Nano* **7**, 1068–1081 (2020).
232. Miller, Q. R. S. *et al.* Insights into silicate carbonation processes in water-bearing supercritical CO2 fluids. *International Journal of Greenhouse Gas Control* **15**, 104–118 (2013).
233. Galib, M. & Hanna, G. The Role of Hydrogen Bonding in the Decomposition of H2CO3 in Water: Mechanistic Insights from Ab Initio Metadynamics Studies of Aqueous Clusters. *J. Phys. Chem. B* **118**, 5983–5993 (2014).
234. Galib, M. & Hanna, G. Molecular dynamics simulations predict an accelerated dissociation of H 2 CO 3 at the air–water interface. *Physical Chemistry Chemical Physics* **16**, 25573–25582 (2014).
235. Leung, K., Nielsen, I. M. B. & Kurtz, I. Ab Initio Molecular Dynamics Study of Carbon Dioxide and Bicarbonate Hydration and the Nucleophilic Attack of Hydroxide on CO2. *J. Phys. Chem. B* **111**, 4453–4459 (2007).
236. Dopieralski, P. D., Burakowski, A., Latajka, Z. & Olovsson, I. Hydration of NaHCO3, KHCO3, (HCO3-)2, HCO3- and CO32- from molecular dynamics simulation and speed of sound measurements. *Chemical Physics Letters* **507**, 89–95 (2011).
237. Iida, K., Yokogawa, D., Sato, H. & Sakaki, S. The barrier origin on the reaction of CO2+OH− in aqueous solution. *Chemical Physics Letters* **443**, 264–268 (2007).
238. Wogelius, R. A. & Walther, J. V. Olivine dissolution kinetics at near-surface conditions. *Chemical Geology* **97**, 101–112 (1992).
239. Pokrovsky, O. S. & Schott, J. Kinetics and mechanism of forsterite dissolution at 25°C and pH from 1 to 12. *Geochimica et Cosmochimica Acta* **64**, 3313–3325 (2000).
240. Golubev, S. V., Pokrovsky, O. S. & Schott, J. Experimental determination of the effect of dissolved CO2 on the dissolution kinetics of Mg and Ca silicates at 25 °C. *Chemical Geology* **217**, 227–238 (2005).
241. van Duin, A. C. T., Dasgupta, S., Lorant, F. & Goddard, W. A. ReaxFF: A Reactive Force Field for Hydrocarbons. *J. Phys. Chem. A* **105**, 9396–9409 (2001).
242. Fenter, P., Kerisit, S., Raiteri, P. & Gale, J. D. Is the Calcite–Water Interface Understood? Direct Comparisons of Molecular Dynamics Simulations with Specular X-ray Reflectivity Data. *J. Phys. Chem. C* **117**, 5028–5042 (2013).
243. Demichelis, R., Raiteri, P., Gale, J. D., Quigley, D. & Gebauer, D. Stable prenucleation mineral clusters are liquid-like ionic polymers. *Nat Commun* **2**, 590 (2011).
244. Zare, S. & Abdolhosseini Qomi, M. J. Reactive force fields for aqueous and interfacial magnesium carbonate formation. *Physical Chemistry Chemical Physics* **23**, 23106–23123 (2021).
245. König, P. H. *et al.* Toward Theoretical Analyis of Long-Range Proton Transfer Kinetics in Biomolecular Pumps. *J. Phys. Chem. A* **110**, 548–563 (2006).
246. Cornu, D., Guesmi, H., Krafft, J.-M. & Lauron-Pernot, H. Lewis Acido-Basic Interactions between CO2 and MgO Surface: DFT and DRIFT Approaches. *J. Phys. Chem. C* **116**, 6645–6654 (2012).
247. Stark, J. V., Park, D. G., Lagadic, I. & Klabunde, K. J. Nanoscale Metal Oxide Particles/Clusters as Chemical Reagents. Unique Surface Chemistry on Magnesium Oxide As Shown by Enhanced

Adsorption of Acid Gases (Sulfur Dioxide and Carbon Dioxide) and Pressure Dependence. *Chem. Mater.* **8**, 1904–1912 (1996).
248. Baltrusaitis, J., Schuttlefield, J., Zeitler, E. & Grassian, V. H. Carbon dioxide adsorption on oxide nanoparticle surfaces. *Chemical Engineering Journal* **170**, 471–481 (2011).
249. Marx, D. Proton Transfer 200 Years after von Grotthuss: Insights from Ab Initio Simulations. *ChemPhysChem* **7**, 1848–1870 (2006).
250. Agmon, N. Mechanism of hydroxide mobility. *Chemical Physics Letters* **319**, 247–252 (2000).
251. Tuckerman, M. E., Marx, D. & Parrinello, M. The nature and transport mechanism of hydrated hydroxide ions in aqueous solution. *Nature* **417**, 925 (2002).
252. Chen, M. *et al.* Hydroxide diffuses slower than hydronium in water because its solvated structure inhibits correlated proton transfer. *Nature Chemistry* **10**, 413–419 (2018).
253. Zelovich, T. *et al.* Hydroxide Ion Diffusion in Anion-Exchange Membranes at Low Hydration: Insights from Ab Initio Molecular Dynamics. *Chem. Mater.* **31**, 5778–5787 (2019).
254. Duin, A. C. T. van, Zou, C., Joshi, K., Bryantsev, V. & Goddard, W. A. CHAPTER 6:A Reaxff Reactive Force-field for Proton Transfer Reactions in Bulk Water and its Applications to Heterogeneous Catalysis. in *Computational Catalysis* 223–243 (2013). doi:10.1039/9781849734905-00223.
255. Quaranta, V., Hellström, M. & Behler, J. Proton-Transfer Mechanisms at the Water–ZnO Interface: The Role of Presolvation. *J. Phys. Chem. Lett.* **8**, 1476–1483 (2017).
256. Hellström, M., Quaranta, V. & Behler, J. One-dimensional vs. two-dimensional proton transport processes at solid–liquid zinc-oxide–water interfaces. *Chemical Science* **10**, 1232–1243 (2019).
257. Lee, M.-S., Peter McGrail, B., Rousseau, R. & Glezakou, V.-A. Structure, dynamics and stability of water/scCO_2/mineral interfaces from *ab initio* molecular dynamics simulations. *Scientific Reports* **5**, 14857 (2015).
258. Giraudo, N. *et al.* Early Stage Hydration of Wollastonite: Kinetic Aspects of the Metal-Proton Exchange Reaction. *J. Phys. Chem. C* **119**, 10493–10499 (2015).
259. Teng, H. H., Fenter, P., Cheng, L. & Sturchio, N. C. Resolving orthoclase dissolution processes with atomic force microscopy and X-ray reflectivity. *Geochimica et Cosmochimica Acta* **65**, 3459–3474 (2001).
260. Casey, W. H. & Westrich, H. R. Control of dissolution rates of orthosilicate minerals by divalent metal–oxygen bonds. *Nature* **355**, 157–159 (1992).
261. Palandri, J. L. & Kharaka, Y. K. *A Compilation of Rate Parameters of Water-Mineral Interaction Kinetics for Application to Geochemical Modeling*. https://apps.dtic.mil/docs/citations/ADA440035 (2004).
262. Rimstidt, J. D., Brantley, S. L. & Olsen, A. A. Systematic review of forsterite dissolution rate data. *Geochimica et Cosmochimica Acta* **99**, 159–178 (2012).
263. Shao, H., Ray, J. R. & Jun, Y.-S. Effects of organic ligands on supercritical CO2-induced phlogopite dissolution and secondary mineral formation. *Chemical Geology* **290**, 121–132 (2011).
264. Raiteri, P. & Gale, J. D. Water Is the Key to Nonclassical Nucleation of Amorphous Calcium Carbonate. *J. Am. Chem. Soc.* **132**, 17623–17634 (2010).
265. Yoreo, J. J. D. *et al.* Crystallization by particle attachment in synthetic, biogenic, and geologic environments. *Science* **349**, (2015).
266. Lasaga, A. C. Chemical kinetics of water-rock interactions. *Journal of Geophysical Research: Solid Earth* **89**, 4009–4025 (1984).
267. Putnis, A. Why Mineral Interfaces Matter. *Science* **343**, 1441–1442 (2014).
268. Ruiz-Agudo, E., Putnis, C. V. & Putnis, A. Coupled dissolution and precipitation at mineral–fluid interfaces. *Chemical Geology* **383**, 132–146 (2014).

269. Martin, M. G. & Siepmann, J. I. Novel Configurational-Bias Monte Carlo Method for Branched Molecules. Transferable Potentials for Phase Equilibria. 2. United-Atom Description of Branched Alkanes. *J. Phys. Chem. B* **103**, 4508–4517 (1999).
270. Martin, M. G. & Thompson, A. P. Industrial property prediction using Towhee and LAMMPS. *Fluid Phase Equilibria* **217**, 105–110 (2004).
271. Kästner, J. & Thiel, W. Analysis of the statistical error in umbrella sampling simulations by umbrella integration. *J. Chem. Phys.* **124**, 234106 (2006).

APPENDIX A

Supplementary Note 1: H_2O-CO_2 mixture adsorption in the macro-pore: Grand Canonical Monte Carlo (GCMC) simulations were used to determine the thermodynamic properties of the bulk H_2O-CO_2 mixture. We used the method of Configurational Biased Monte Carlo (CBMC)[269,270] as implemented in Towhee[86] to adsorb the mixture into a periodic box with dimensions (40 Å ×40 Å × 40Å) in the grand canonical ensemble ($\mu_{H_2O}\mu_{CO_2}VT$). The cell dimensions are taken large enough to reduce the standard deviation of the solvent concentration as much as possible. The corresponding biased probabilities are given in the main text. We performed these GCMC simulations by considering 315 pairs of chemical potentials (μ_{H_2O}, μ_{CO_2}) in the ranges [-49,-42] kJ/mol and [-40, -30] kJ/mol for water and CO_2 respectively except for the simulations that were done at 348K with CO_2-rich condition where the chemical potential of water was in the range [-49,-45] kJ/mol. To examine whether phase coexistence exists, we assumed two different initial mixture compositions relevant to CO_2-rich and H_2O-rich conditions for all pairs of chemical potentials. Higher initial number of CO_2 molecules than water molecules were put on the lattice points for the CO_2-rich cases, and liquid water for the H_2O-rich cases were considered. We used rigid SPC[88] model and EPM2 model[89] for water and CO_2 respectively. All simulations are equilibrated for more than 25 million MC steps. The results are shown in **Fig. A1** and **Fig. A2** for temperatures of 348K and 300K respectively. The phase of the H_2O-CO_2 mixture is determined by μ_{H_2O} or μ_{CO_2} or both. At a specific range of chemical potentials, the mixture could be in

coexisting CO_2-rich and H_2O-rich phases with two degrees of freedom (μ_{H_2O}, μ_{CO_2}) consistent with the Gibbs phase rule:

$$F = 2 + C - P \qquad \text{Eq. A1}$$

Where two degrees of freedom (F) is derived for a two-component immiscible mixture (C=2) with two phases (gas or liquid) (P=2). As expected for immiscible mixtures, CO_2 was calculated to be dominant when water is below saturation level ($\mu \leq 47 \frac{kJ}{mol}$ at 348K and $\mu \leq 46 \frac{kJ}{mol}$ at 300K) as it could only be found in vapor form in that regime, see **Fig. A1.e** and **Fig. A2.e**. The density and pressure of CO_2-rich mixtures are merely controlled by the chemical potential of CO_2, see density and pressure colormaps in **Fig. A1** and **Fig. A2** for CO_2-rich phases. In the H_2O-rich phase, as water is found in liquid form the density is around 1 g/cm^3 while the pressure is mostly controlled by the chemical potential of water. On the other hand, the molar fractions of components are sensitive to the chemical potential of both components, like in **Fig.A1.b** where the lowest CO_2 mole fraction is reached at the lowest μ_{CO_2} and highest μ_{H_2O}, and as we move from top left to bottom right of the diagram this molar fraction increases. To make the molar fractions clearer, H_2O molar fractions are depicted in **Fig. S3** for the regions of chemical potential space where CO_2 is dominant.

Supplementary Note 2: H_2O-CO_2 mixture adsorption in the slit nanopore: Upon GCMC calculations in the slit-pore of the mineral, CO_2 could only penetrate the slit pore when the interlayer distance is more than 30 Å, as could be seen in **Fig. A4.a**. At interlayer distances of less 20 Å, the density of capillary water is found to be higher than its bulk value (1 g/cm^3) consistent with the simulations on the ultra-confined nature of water in CSH[121,122], see **Fig A4-b**.

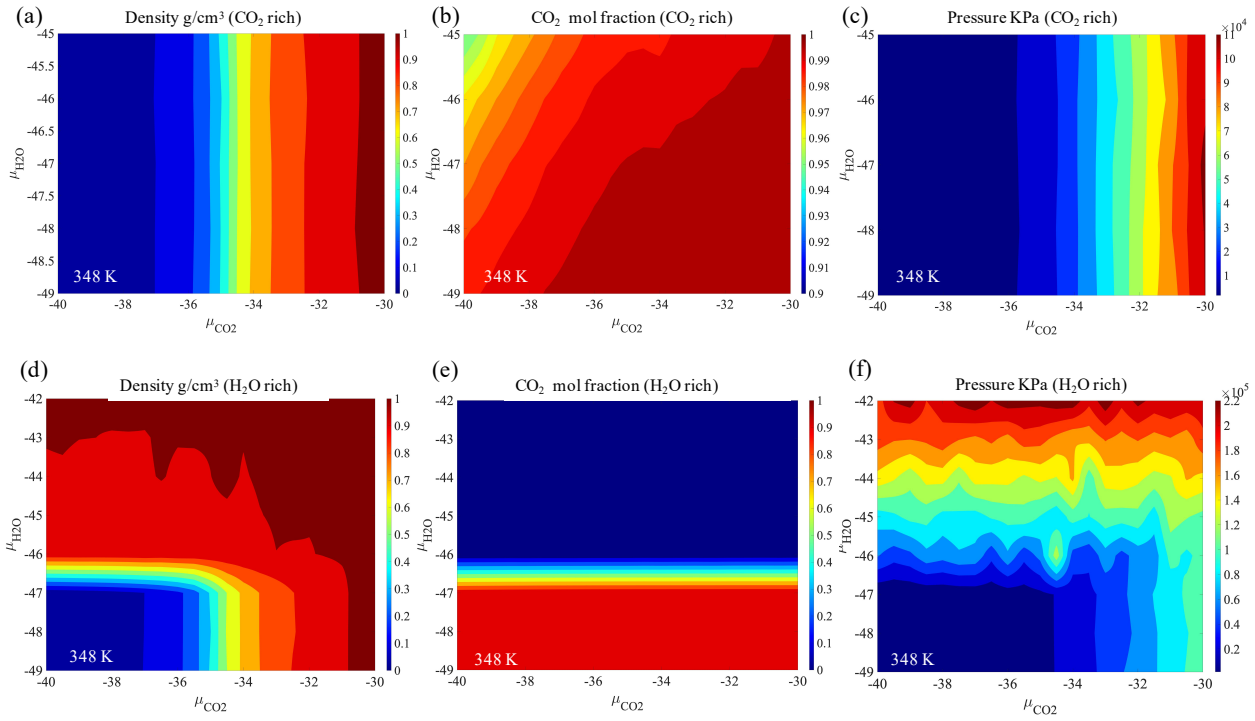

Fig. A1. Adsorption of CO_2-H_2O mixture in the macro-pore at 348K. Colormaps of different thermodynamic properties are derived based on the independent variables (μ_{H_2O}, μ_{CO_2}). (a) density derived for a box initially at CO_2-rich condition. (b) CO_2 mole fraction derived for a box initially at CO_2-rich condition. (c) Pressure derived for a box initially at CO_2-rich condition. scCO_2 points at 100bar and 200bar were chosen for slit-pore adsorption. (d) Density for a box initially at H_2O-rich condition. (e) CO_2 mole fraction derived for a box initially at H_2O-rich condition. (f) Pressure derived for a box initially at H_2O-rich condition.

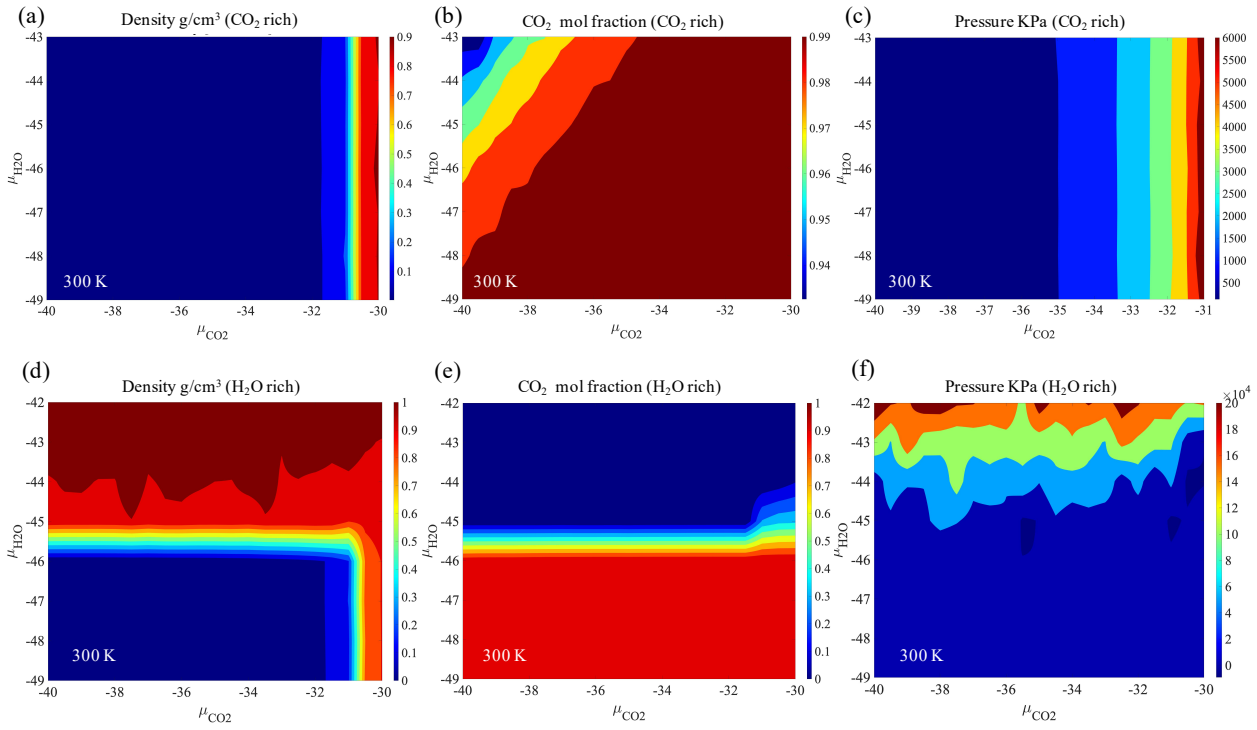

Fig. A2. Adsorption of CO_2-H_2O mixture in the macro-pore at 300K. Colormaps of different thermodynamic properties are derived based on the independent variables (μ_{H_2O}, μ_{CO_2}). (a) density derived for a box initially at CO_2-rich condition. (b) CO_2 mole fraction derived for a box initially at CO_2-rich condition. (c) Pressure derived for a box initially at CO_2-rich condition. sbCO_2 at 20bar and normal condition at 1 bar were chosen for slit-pore adsorption (d) Density for a box initially at H_2O-rich condition. (e) CO_2 mole fraction derived for a box initially at H_2O-rich condition. (f) Pressure derived for a box initially at H_2O-rich condition.

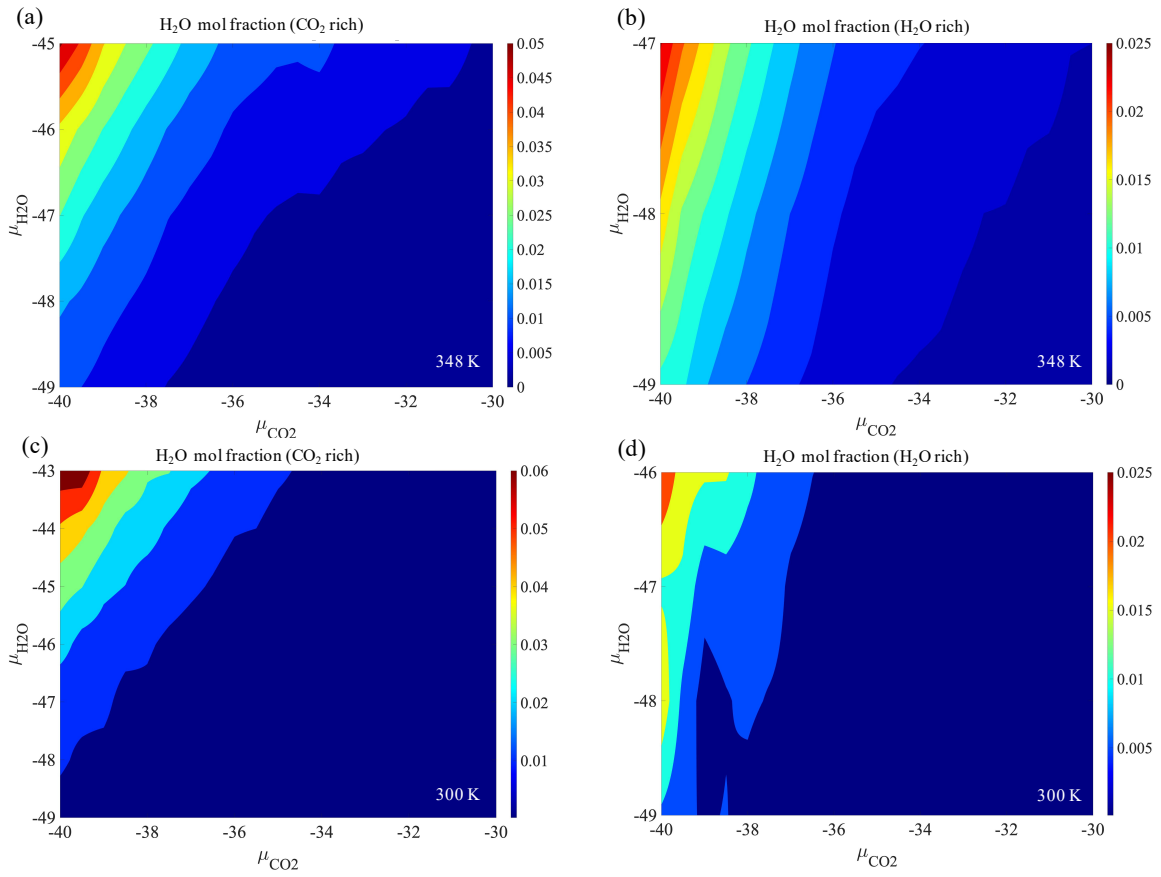

Fig. A3. H_2O mole fraction in the macropore dominated by CO_2. (a) Mole fraction of water at 348K in a cell initially rich with water. It was converged to the CO_2-rich phase for the below saturation conditions $\mu_{H_2O} \leq 47\ kj/mol$. (b) Mole fraction of water at 348K in a cell initially rich with CO_2. (c) Mole fraction of water at 300K in a cell initially rich with CO_2. (d) Mole fraction of water at 300K in a cell initially rich with water. It was converged to the CO_2-rich phase for when $\mu_{H_2O} \leq 46\ kj/mol$.

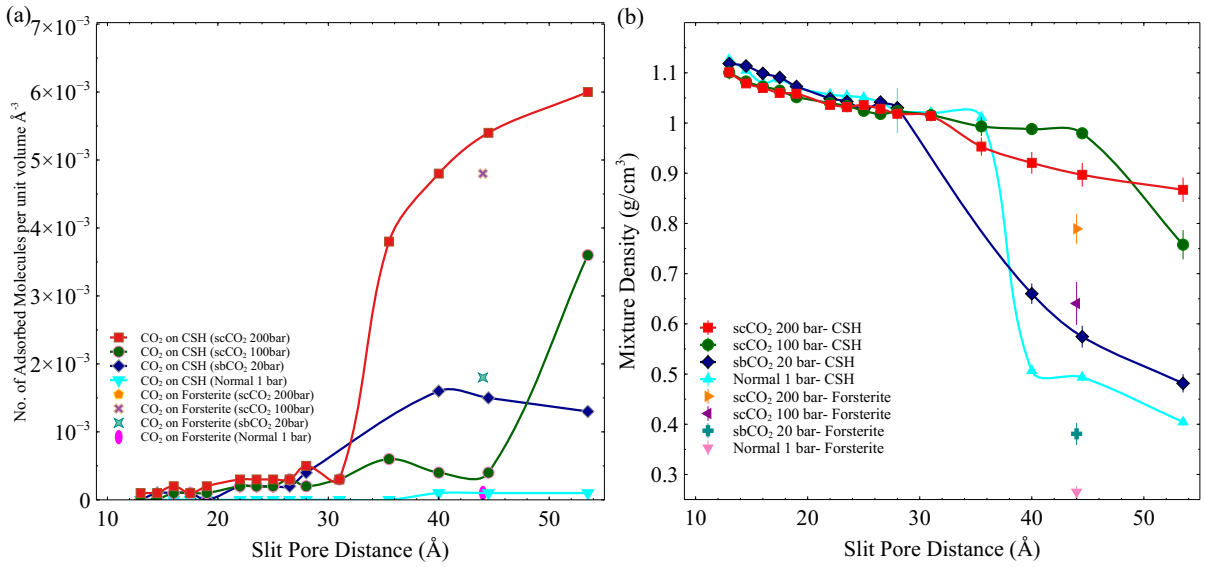

Fig. A4. Adsorption of CO_2-H_2O mixture in the slit-pore of rock. (a) Number of adsorbed molecules per unit volume based on the slit-pore distance. 1/V dashed line shows that the number of water molecules is constant. It shows that after a certain distance only interfacial water exists. (b) The density of the mixture based on the slit-pore distance at various thermodynamic conditions.

APPENDIX B

Supplementary Note 1: Error estimation for the free energy path of dissolution: To calculate the error in the free energy barrier for the dissolution of ions from the surface, we use the methodology developed in Kastner and Thiel (2006)[271]. Here, we extend that methodology, which was applicable to one collective variable, for a two-dimensional free energy landscape. The biased probability distribution function of the 2-dimensional collective variable $\vec{\xi}$ in window i can be approximated by a gaussian function based on mean values, $\overrightarrow{\bar{\xi}_i^b}$, and the covariance matrix C:

$$P_i^b\left(\vec{\xi}\right) = (2\pi)^{-1}\det(C)^{-1/2} e^{-\frac{1}{2}(\vec{\xi}-\overrightarrow{\bar{\xi}_i^b})^T C^{-1}(\vec{\xi}-\overrightarrow{\bar{\xi}_i^b})} \quad \text{Eq. A2}$$

The unbiased mean force for each window is:

$$\vec{\nabla} {A_i}^u = -\frac{1}{\beta}\vec{\nabla} ln P_i^b\left(\vec{\xi}\right) - \vec{\nabla} w_i = -\frac{1}{\beta}\vec{\nabla}\left[-\frac{1}{2}\left(\vec{\xi}-\overrightarrow{\bar{\xi}_i^b}\right)^T C^{-1}\left(\vec{\xi}-\overrightarrow{\bar{\xi}_i^b}\right)\right] - \vec{\nabla} w_i = \frac{1}{\beta}\left[C^{-1}\left(\vec{\xi}-\overrightarrow{\bar{\xi}_i^b}\right)\right] - \vec{\nabla} w_i \quad \text{Eq. A3}$$

In which w_i is the harmonic restraint potential for window i. The error propagation in the above equation leads to

$$var\left(\vec{\nabla}{A_i}^u\right) = \frac{1}{\beta^2} var\left(C^{-1}\left(\vec{\xi} - \overrightarrow{\bar{\xi}_i^b}\right)\right) \quad \text{Eq. A4}$$

Writing $C^{-1} = \begin{bmatrix} a & b \\ c & d \end{bmatrix}$ and $\vec{\xi} - \overrightarrow{\bar{\xi}_i^b} = \begin{pmatrix} \xi - \bar{\xi}_i^b \\ \eta - \bar{\eta}_i^b \end{pmatrix}$, the above equation could be written in its component:

$$var\left(\vec{\nabla}{A_i}^u\right) = \frac{1}{\beta^2} var\left(\begin{bmatrix} a & b \\ c & d \end{bmatrix}\begin{pmatrix} \xi - \bar{\xi}_i^b \\ \eta - \bar{\eta}_i^b \end{pmatrix}\right) = \frac{1}{\beta^2} var\left(\begin{pmatrix} a\left(\xi - \bar{\xi}_i^b\right) + b(\eta - \bar{\eta}_i^b) \\ c(\xi - \bar{\xi}_i^b) + d(\eta - \bar{\eta}_i^b) \end{pmatrix}\right) \quad \text{Eq. A5}$$

Using the equation of $var(AB) \approx (AB)^2\left[\frac{var(A)}{A^2} + \frac{var(B)}{B^2}\right]$, $var\left(\vec{\nabla}{A_i}^u\right)$ can be written as

$$var\left(\vec{\nabla}{A_i}^u\right) = {}^1\!/_{\beta^2} \begin{pmatrix} a^2\left(\xi - \bar{\xi}_i^b\right)^2\left[\frac{var(a)}{a^2} + \frac{var\left(\left(\bar{\xi}_i^b\right)\right)}{\left(\xi - \bar{\xi}_i^b\right)^2}\right] + b^2(\eta - \bar{\eta}_i^b)^2\left[\frac{var(b)}{b^2} + \frac{var\left(\left(\bar{\eta}_i^b\right)\right)}{(\eta - \bar{\eta}_i^b)^2}\right] \\ c^2\left(\xi - \bar{\xi}_i^b\right)^2\left[\frac{var(c)}{c^2} + \frac{var\left(\left(\bar{\xi}_i^b\right)\right)}{\left(\xi - \bar{\xi}_i^b\right)^2}\right] + d^2(\eta - \bar{\eta}_i^b)^2\left[\frac{var(d)}{d^2} + \frac{var\left(\left(\bar{\eta}_i^b\right)\right)}{(\eta - \bar{\eta}_i^b)^2}\right] \end{pmatrix} \quad \text{Eq. A6}$$

The variance of unbiased mean force could be written as the weighted sum of variance of unbiased mean force at each window:

$$var\left(\vec{\nabla}A^u\right) = \sum_i^{windows} p_i^2 var\left(\vec{\nabla}{A_i}^u\right) \quad \text{Eq. A7}$$

In which, the probability $p_i(\vec{\xi})$ could be written as

$$p_i\left(\vec{\xi}\right) = N_i P_i^b\left(\vec{\xi}\right) / \sum_i N_i\, P_i^b\left(\vec{\xi}\right) \quad \text{Eq. A8}$$

$$\Delta A = \int_{\overrightarrow{\xi_a}}^{\overrightarrow{\xi_b}} \vec{\nabla} A^u . \overrightarrow{d\xi} = \int_{\overrightarrow{\xi_a}}^{\overrightarrow{\xi_b}} \left(\frac{\partial A^u}{\partial \xi} d\xi + \frac{\partial A^u}{\partial \eta} d\eta\right) \quad \text{Eq. A9}$$

The error in ΔA propagates as follows

$$var(\Delta A) = \int_{\xi_a}^{\xi_b} \int_{\xi_a'}^{\xi_b'} cov\left(\frac{\partial A^u}{\partial \xi}, \frac{\partial A^u}{\partial \xi'}\right) d\xi . d\xi' + \int_{\eta_a}^{\eta_b} \int_{\eta_a'}^{\eta_b'} cov\left(\frac{\partial A^u}{\partial \eta}, \frac{\partial A^u}{\partial \eta'}\right) d\eta . d\eta' \quad \text{Eq. A10}$$

The final error in ΔA at 95% confidence level is:

$$\pm 1.96\sqrt{var(\Delta A)} \quad \text{Eq. A11}$$

Supplementary Note 2: Potential-of-mean-force (PMF) for the dissolution of magnesium from the forsterite surface: To sample the full phase space in our free energy calculation for the dissolution of magnesium from the forsterite surface, we consider the surface Mg water coordination number in addition to its perpendicular distance from the surface. The coordination number is defined as below:

$$CN = \sum_{i \in \{Ow\}} \frac{1-\left(\frac{r_i - d_0}{r_0}\right)^n}{1-\left(\frac{r_i - d_0}{r_0}\right)^m} \quad \text{Eq. A12}$$

where r_{ij} is the distance of water molecule *i* with the surface Mg, r_0 is set to 1 Å, d_0 is set to 2.2 Å, n is equal to 4, and m is equal to 8. The value of d_0 is taken from the peak distance of the surface Mg-water pair distribution function.